ADVANCED FUNCTIONAL MATERIALS
www.afm-journal.de

Check for updates

Recent Progress on Flexible Silicon Nanomembranes for Advanced Electronics and Optoelectronics

Ziyu Zhang, Yang Wang, Tianjun Cai, Binmin Wu, Bofan Hu, Xing Li, Enming Song, Gaoshan Huang, Ziao Tian, Zengfeng Di,* and Yongfeng Mei**

Silicon nanomembranes, an emerging material with ultrathin thickness, combine the electrical properties of semiconductors with the flexibility that bulk materials lack. These nanomembranes can impart enhanced functionality to devices, supporting development needs for next-generation technologies "more-than-Moore" Law. In recent years, as research of fabrication techniques and fundamental principles have advanced, the focus of silicon nanomembrane studies has evolved from material preparation and component processing to functionalization and system-level integration. This review begins with an overview of silicon nanomembrane preparation methods and formation principles. In terms of device advancements and applications, developments in optoelectronic devices, sensors, biomedicine, energy harvesting, and integrated circuits are covered. Finally, the review discusses the current challenges in silicon nanomembrane technology and the potential of silicon nanomembrane devices and systems in future optoelectronics, biomedicine, energy harvesting, and advanced integrated circuit architectures.

1. Introduction

Silicon, as one of the critical elements in the semiconductor field, plays a pivotal role in the development of modern electronic technology, industrial products, and the global economy.[1] However, as the demands for device performance and functionality continue to escalate, the traditional optimization strategies for silicon-based devices face challenges. The current trend of miniaturizing integrated circuits is approaching physical limits, exacerbating thermal management issues as integration density increases.[2] Additionally, quantum effects such as tunneling and short-channel effects become more pronounced, undermining device stability and performance.[3] Furthermore, the inherent rigidity and lack of flexibility in bulk silicon materials hinder their suitability for emerging applications that require flexible and multifunctional capabilities.[4] These limitations constrain the application of traditional silicon devices in future high-performance and multifunctional electronic systems.

In recent years, the "more-than-Moore" paradigm has emerged as a focal point in integrated circuit (IC) technology development.[5] This approach aims to enhance chip performance not only by further scaling down transistor dimensions but also by introducing new materials, structures, and functionalities. For example, silicon nanowires have emerged as a low-dimensional

Z. Zhang, Y. Wang, T. Cai, B. Hu, X. Li, G. Huang, Y. Mei
Department of Materials Science & State Key Laboratory of Surface Physics
Fudan University
Shanghai 200438, P. R. China
E-mail: yfm@fudan.edu.cn

Z. Tian, Z. Di
State Key Laboratory of Materials for Integrated Circuits
Shanghai Institute of Microsystem and Information Technology
Chinese Academy of Sciences
Shanghai 200050, P. R. China
E-mail: zfdi@mail.sim.ac.cn

B. Wu
State Key Laboratory of Infrared Physics
Shanghai Institute of Technical Physics
Chinese Academy of Sciences
Shanghai 200083, P. R. China
E-mail: wubinmin@mail.sitp.ac.cn

G. Huang, Y. Mei
Yiwu Research Institute of Fudan University
Yiwu, Zhejiang 322000, P. R. China

E. Song, G. Huang, Y. Mei
International Institute of Intelligent Nanorobots and Nanosystems
Fudan University
Shanghai 200438, P. R. China

G. Huang
State Key Laboratory of Photovoltaic Science and Technology
Fudan University
Shanghai 200438, P. R. China

E. Song, Y. Mei
Shanghai Frontiers Science Research Base of Intelligent Optoelectronics and Perception
Institute of Optoelectronics
Fudan University
Shanghai 200438, P. R. China

The ORCID identification number(s) for the author(s) of this article can be found under https://doi.org/10.1002/adfm.202502191

DOI: 10.1002/adfm.202502191

© 2025 Wiley-VCH GmbH

structure, with unique electrical and mechanical properties.[6] When implemented in field-effect transistors, these nanoscale structures enable superior gate control and carrier transport characteristics,[7] demonstrating the potential of novel materials in extending device performance. Along with silicon nanowires, the "more-than-Moore" strategy leverages other emerging technologies such as multifunctional and heterogeneous integration, three-dimensional integrated circuits (3D ICs),[8] photonic integrated circuits (PICs),[9] and micro-electro-mechanical systems (MEMS)[10] to overcome the physical limitations of traditional scaling and drive advancements in semiconductor technology to meet diverse application needs.

Within this technological framework, silicon nanomembranes (SiNMs) have become crucial solutions for the next generation of devices.[11] Since the bending stiffness of a material is proportional to the cube of its thickness, nanoscale thickness in films results in remarkable flexibility and structural malleability. At the same time, SiNMs can maintain excellent semiconductor material properties[12] while enabling additional external field coupling and detection functions.[13] Notably, SiNMs, structured through self-rolling processes based on strain engineering, and flexible SiNM devices fabricated using transfer printing techniques, have contributed to advancements from a "more-than-Moore" perspective. The self-rolling process exploits strain gradients introduced during the epitaxial growth or deposition of SiNMs, enabling the formation of microstructures through strain release, and thereby achieving microstructure fabrication in a single step.[14] This process enhances device integration by incorporating additional functionalities through three-dimensional space, which is critical in optoelectronics, MEMS,[15] and energy-related applications.[16] Conversely, the transfer printing process allows for the transfer of strain-free SiNMs onto designated flexible substrates, facilitating device fabrication with excellent biocompatibility and scalability, and novel physics mechanisms.[17] Consequently, flexible SiNM-based electronic and energy devices have garnered increasing attention in fields such as optoelectronics, ICs, substance sensing, biomedicine, and energy harvesting. Devices based on SiNMs will advance bulk planar silicon-based semiconductor devices in three directions: 1) Thickness-dependent physical properties. At different thicknesses, the varying dominance of interface states, quantum confinement effects, and bulk semiconductor silicon lead to differences in the electrical, optical, and thermal properties of SiNM,[17a,18] introducing new mechanisms from the material itself. 2) On-demand functional integration. By utilizing three-dimensional structures formed through external deformation or internal strain, these devices offer customizable functionalities, including stress measurement,[10a,19] temperature sensing,[20] and polarization detection.[14a,21] 3) In situ, real-time detection. The combination of flexibility of SiNMs with flexible substrates enhances the accurate sensing of signals on complex surfaces, and their bendable and foldable characteristics will play a crucial role in device miniaturization and portability.[22]

In this review, we provide an overview of the fabrication processes, physical properties, device applications, and future developments of SiNMs in the fields of electronic devices and energy harvesting. First, we discuss the principles and methods of SiNM preparation, assembly, and transfer. Following this, we delve into the applications and unique advantages of flexible SiNMs in optoelectronics, substance sensing, biomedicine, and energy-related domains. Then, we explore the challenges and breakthroughs associated with achieving large-area integration, multidimensional sensing, and high-performance energy storage using flexible SiNMs in next-generation electronic devices and energy storage systems. At the end of the review, we analyzed the bottlenecks faced by the further development of SiNMs from the perspectives of materials, devices, and systems, highlighting the research directions that require attention. We also explored promising processing techniques. We believe that SiNM, as an indispensable thin-film material, will continue to make contributions in the fields of electronic and optoelectronic devices.

2. Preparation, Assembly, and Design of SiNMs

Since the first fabrication of SiNMs by peeling from the substrate, the field has been developed over 20 years. With continuous research and development, the process has evolved from the inability to apply the films and the randomness of the peeling procedure to the controllable fabrication of devices. In recent years, SiNMs have advanced to the point where, through sophisticated device structures and algorithm-software assistance, they can achieve highly customized, system-level, multifunctional integration. SiNM technology has opened broader fields for the design and application of silicon semiconductor devices.

The strain state and origin of strain in SiNMs determine their morphology, functionality, and application fields, and can generally be classified into three categories: 1) Strain-free SiNMs, typically used in high-integration devices on rigid substrates or as conformal flexible devices after substrate removal (**Figure 1**a–i);[10a,12a,16,22c,23,24,25,26] 2) SiNMs based on external strain engineering, which lack internal stress upon substrate release but undergo deformation under intentionally applied external strain, often for precisely designed microstructures and large-deformation flexible devices (Figure 1j–q);[14c,27–32] 3) SiNMs with intrinsic strain gradients, where strain originates from differences in thermal expansion coefficients or lattice mismatch within the material system, leading to spontaneous deformation upon substrate release. These self-assembled microstructures show great potential in fields like optoelectronic detection and energy harvesting (Figure 1r–y).[14a,b,21,33–36] When the SiNM is subjected to minimal external strain, its inherent flexibility facilitates conformal attachment to target surfaces and in situ signal sensing. Compared to epitaxial SiNMs, SiNMs fabricated via etching silicon on insulator (SOI) wafers exhibit lower strain and almost no strain gradient in the thickness direction. Therefore, SOI wafers are typically used to fabricate strain-free SiNM structures and devices.[37] Consequently, defining micro patterns,[38] especially micropores[39] within the SiNM and etching the silicon dioxide sacrificial layer on SOI, followed by adhesive peeling with an elastic stamp, has become a common method for obtaining SiNMs (Figure 1a–d).[12a,23,24,40] In addition, the efficient transfer of SiNMs and their adhesion to a wide range of material surfaces can be achieved through advancements in the optimization and analysis of micro- and nano-structures.[17b,41] The biocompatibility and flexibility of SiNMs make them one of the promising candidates for wearable and implantable biomedical devices and in-situ sensors (Figure 1e–g).[10a,25,42] Their degradable nature allows implanted devices to dissolve naturally after

© 2025 Wiley-VCH GmbH

16163028, 2025, 35, Downloaded from https://advanced.onlinelibrary.wiley.com/doi/10.1002/adfm.202502191 by Fudan University, Wiley Online Library on [08/03/2026]. See the Terms and Conditions (https://onlinelibrary.wiley.com/terms-and-conditions) on Wiley Online Library for rules of use; OA articles are governed by the applicable Creative Commons License

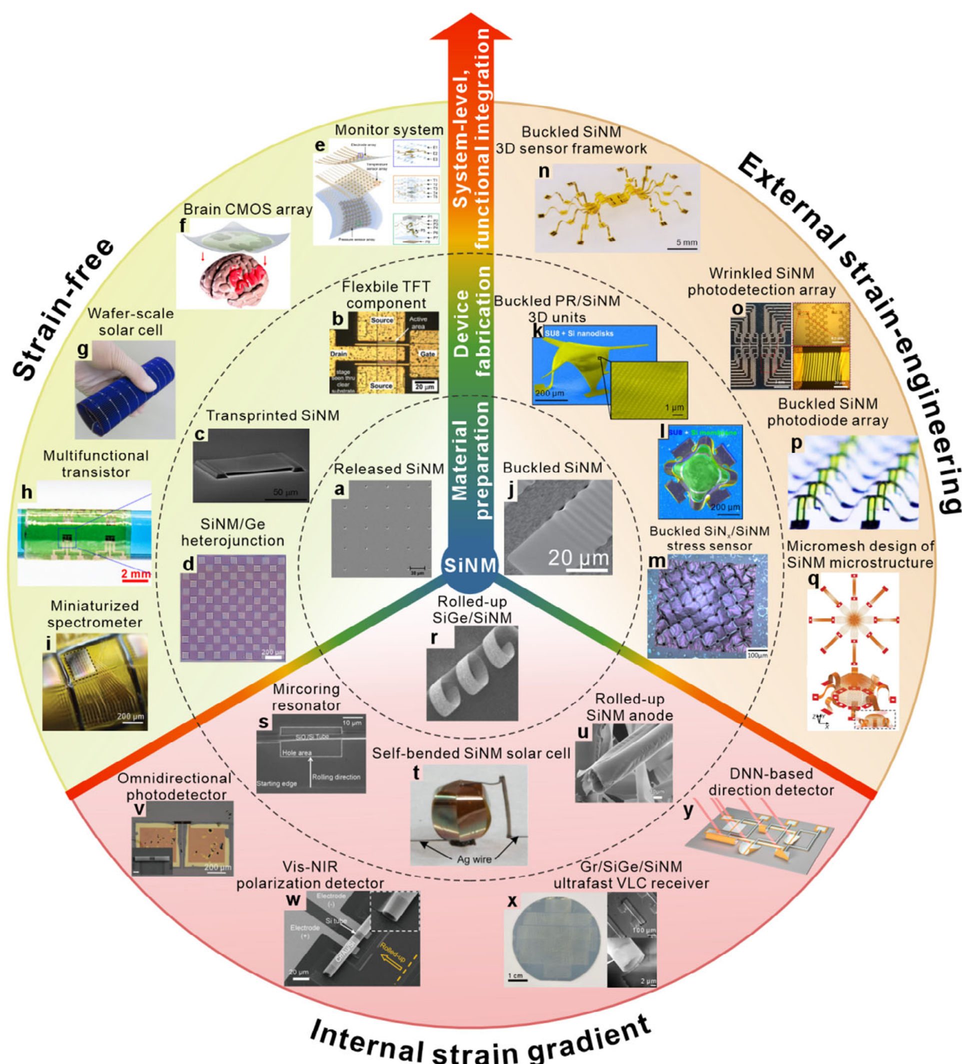

Figure 1. Schematic diagram of the development of SiNMs. a) Optical image of the released SiNM on a PI substrate. Panel (a) courtesy of Bofan Hu. b) Optical image of flexible SiNM TFT. Reproduced with permission.[23] Copyright 2006, AIP Publishing. c) Released 260 nm SiNM, which is suspended on two silicon bars.[24] d) Optical image of SiNM/Ge heterojunction. Reproduced with permission.[12a] Copyright 2011, American Chemical Society. e) Schematic illustration of a SiNM monitor system for temperature and pressure. Reproduced with permission.[10a] Copyright 2020, Springer Nature. f) Schematic of integrated SiNM CMOS array on a brain model. Reproduced with permission.[25] Copyright 2019, National Academy of Sciences. g) Photograph of a 15.6 cm × 15.6 cm bendable SiNM solar cell. Reproduced with permission.[16] Copyright 2023, Springer Nature. h) Optical image of multifunctional flexible SiNM sensor array. Reproduced with permission.[26] Copyright 2020, AAAS. i) Optical image of a unit of SiNM optical cavity for miniaturized spectrometers. Reproduced with permission.[22c] Copyright 2024, AAAS. j) SEM images of buckled SiNMs. Reproduced with permission.[27] Copyright 2017, IEEE. Colored SEM images of buckled k) Photoresist (PR)/ SiNM nanodisk and l) PR/SiNM microstructures. Reproduced with permission.[14c] Copyright 2015, National Academy of Sciences. m) Optical image of buckled SiN_x NM/SiNM stress sensor. Reproduced with permission.[28] Copyright 2014, Elsevier. n) 3D buckled SiNM device on biomedical devices. Reproduced with permission.[29] Copyright 2021, National Academy of Sciences. o) Digital photograph and optical images of 6×6 SiNM wrinkle NIR photodetection array. Reproduced with permission.[30] Copyright 2024, AAAS. p) Optical image of buckled SiNM photodiode array. Reproduced with permission.[31] Copyright 2018, American Chemical Society. q) FEM simulation of pre-strained and buckled 3D micromesh structures.[32] r) SEM image of rolled-up SiGe/SiNM structure. Reproduced with permission.[33] Copyright 2005, Wiley-VCH. s) SEM image of SiO_x/Si tube as a microring resonator. Reproduced with permission.[34] Copyright 2007, Elsevier. t) Optical image of a self-bended SiNM/Cr/Au photovoltaic device for energy harvesting. Reproduced with permission.[35] Copyright 2009, National Academy of Sciences. u) SEM image of rolled-up SiNM as an anode in batteries. Reproduced with permission.[36] Copyright 2018, Wiley-VCH. v) SEM image of SiNM microtube omnidirectional photodetector. Reproduced with permission.[14b] Copyright 2019, Wiley-VCH. w) SEM image of rolled-up c-SiNM vis-NIR polarization photodetector. Reproduced with permission.[14a] Copyright 2023, Wiley-VCH. x) Optical image of wafer-scale Gr/SiGe NM/SiNM ultrafast VLC receiver. Reproduced with permission.[21] Copyright 2024, Wiley-VCH. y) Schematics of a DNN-based direction photodetection via SiNM/Cr with various structures. Panel (y) courtesy of Ziyu Zhang.

© 2025 Wiley-VCH GmbH

16163028, 2025, 35, Downloaded from https://advanced.onlinelibrary.wiley.com/doi/10.1002/adfm.202502191 by Fudan University, Wiley Online Library on [08/03/2026]. See the Terms and Conditions (https://onlinelibrary.wiley.com/terms-and-conditions) on Wiley Online Library for rules of use; OA articles are governed by the applicable Creative Commons License

their service life, eliminating the need for surgical removal.[43] Additionally, the inherent light absorption-to-thickness properties of SiNMs give them the potential to function as optical microcavities for detecting specific wavelengths (Figure 1h,i).[22c,44] This approach enables wafer-scale delamination of single-crystal SiNMs and their transfer to desired substrates for heterogeneous integration, which has found widespread application in optoelectronic detection, physiological signal sensing, and flexible wearable devices.[45]

When a strain gradient exists within the SiNM as it detaches from the substrate or when an external strain is applied without conformal attachment, the SiNM will release strain and undergo out-of-plane deformation to achieve a stable state with minimal elastic energy (Figure 1j).[46] Based on these characteristics, the on-demand design of micro-scale 3D structures can be realized under macroscopic or controllable parameter conditions, enabling the integration of functional structures. When both ends of the SiNM are fixed, and it is subjected to compressive strain upon release, buckling or wrinkling typically occurs, which enhances the optical absorption and mechanical properties of SiNMs (Figure 1j,o).[27,30] Generally, when the stamp or target substrate used for peeling SiNMs is highly stretchable, pre-stretching before contact with the SiNM can induce compressive strain upon release after delamination, leading to buckling and the formation of periodic out-of-plane deformations (Figure 1k–m).[14c,47] These buckled structures, often anchored at multiple points on the substrate, are well-suited for MEMS.[27,48] Due to the high precision of applying strain engineering to the substrate, this approach is suitable for designing more complex microstructures.

If a SiNM system exhibits a strain gradient in the thickness direction, bending deformations will occur upon detachment from the substrate due to strain release and redistribution (Figure 1r).[33,49] With appropriate pattern design and film deposition processes, various three-dimensional structures such as rings, arches, helices, cones, and tubes can be efficiently constructed in a single-ended fixed configuration.[50] When combined with electrodes or dielectric materials, SiNMs can serve as reliable solutions for "more-than-Moore" integration in optoelectronic detection, energy storage, and electrical components (Figure 1s–u).[51] Therefore, SiNMs can be designed using different fabrication methods and processing techniques according to practical requirements, offering new functionalities and performance while maintaining compatibility with conventional silicon semiconductor processes.[52] The out-of-plane deformation and spatial anisotropy of SiNM devices based on three-dimensional structures will facilitate decoupling and response to external field signals at the microscopic scale (Figure 1w–y).[14a,b,50,53] On the macroscopic scale, they can further enhance energy harvesting efficiency in the photovoltaic field.[16,54] Recently, the microstructure design of SiNMs can also be integrated with emerging artificial intelligence technologies, which not only enhances the complexity and precision of designs, but also detects multidimensional information from device responses (Figure 1y), elevating the application of microstructured SiNM devices to new heights.[32,50] For SiNM, its thickness plays a critical role in determining its physical properties.[55] From a mechanical perspective, the relationship between its thickness and bending radius can be expressed as:

$$r = \frac{t}{2\varepsilon} \tag{1}$$

where t represents the thickness of the thin film and ϵ denotes the strain. This implies that, given the constant fracture strain of silicon, its flexibility significantly increases as the thickness decreases. Simultaneously, its bending stiffness:

$$D = \frac{Et^3}{12\,(1 - \nu^2)} \tag{2}$$

where E is Young's modulus, and ν is Poisson ratio, decreases cubically with reduced thickness, resulting in a pronounced enhancement in deformation under the same strain, thereby allowing semiconductor materials to undergo micron-scale out-of-plane deformation without damage (**Figure 2**a). When the thickness of SiNM is reduced to only a few nanometers, its effective elastic modulus begins to change. Studies by Katiyar et al. revealed that the elastic modulus of SiNM decreases significantly with reduced thickness, as intrinsic surface stress, surface defects, and surface oxide layers increasingly influence its mechanical properties. When the thickness reaches 2 nm, the effective elastic modulus of SiNM drops to 3.25 GPa, far below the 180 GPa of bulk silicon (Figure 2b).[18b] In terms of electronic transport, when the thickness of SiNM is relatively large, its band structure retains the characteristics of bulk silicon. However, when the thickness approaches the de Broglie wavelength of electrons, the motion of electrons within the crystal becomes confined in the thickness direction, leading to the manifestation of quantum confinement effects. At this point, the traditional doping mechanism becomes less obvious in influencing conductivity. Instead, the interaction between surface-reconstructed electronic states (such as the π and π^* bands formed by Si(001) surface reconstruction) and the bulk silicon energy bands determines the electronic transport properties (Figure 2c).[56] As the thickness decreases, the electronic energy bands of SiNM exhibit a blue shift, indicating that its optical absorption bandgap increases with reduced thickness, while the transmittance of the thin film significantly improves.[57] Furthermore, surface roughness in ultrathin SiNM has a pronounced impact on its performance. Surface oxide layers and undulations significantly reduce the phonon mean free path, thereby lowering the thermal conductivity.[58] Consequently, SiNM with thicknesses ranging from tens to hundreds of nanometers typically exhibits mechanical, electrical, and thermal properties similar to those of bulk silicon. Such SiNM is primarily utilized for the flexibilization or functional integration of devices with conventional silicon semiconductor properties. When SiNM approaches atomic-scale thickness, the quantum confinement effects on energy bands and optical properties, as well as the dominance of surface states, lead to devices with lower absorption rates, Young's modulus, and thermal conductivity. This introduces entirely new options for device design and fabrication from the perspective of the physical properties of materials.

The initial preparation of SiNMs is important for subsequent device processing and large-scale production. Fabrication

© 2025 Wiley-VCH GmbH

16163028, 2025, 35, Downloaded from https://advanced.onlinelibrary.wiley.com/doi/10.1002/adfm.202502191 by Fudan University, Wiley Online Library on [08/03/2026]. See the Terms and Conditions (https://onlinelibrary.wiley.com/terms-and-conditions) on Wiley Online Library for rules of use; OA articles are governed by the applicable Creative Commons License

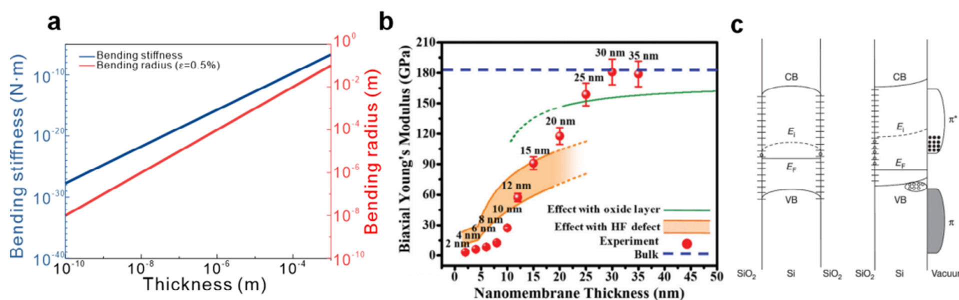

Figure 2. Physical properties of SiNM. a) Relationship between bending stiffness, bending radius, and thickness of silicon. b) Change of biaxial elastic Young's modulus in SiNM against different thickness. Reproduced with permission.[18b] Copyright 2019, Royal Society of Chemistry. c) Energy band in SiO_2/SiNM/SiO_2 and SiO_2/SiNM/vacuum. Reproduced with permission.[] Copyright 2006, Springer Nature.

methods can be broadly classified into top-down and bottom-up approaches. The top-down fabrication method for SiNMs primarily involves thinning bulk silicon and selective etching with masks. Ko et al.[59] reported a method that uses precisely controlled RIE and metal masking to etch and protect silicon sidewalls. A specially designed RIE process creates periodic ripple structures on the sidewalls of bulk silicon, while oblique electron beam evaporation deposits metal on the top and ripple surfaces to prevent subsequent etching. Selective KOH etching removes silicon that is not protected by the metal mask, resulting in a multilayer SiNM structure where the masked regions form NMs. This approach, while involving fewer steps and lower costs, offers limited control over SiNM release and usage, posing challenges for large-area device fabrication. The bottom-up methods include chemical vapor deposition (CVD), physical vapor deposition (PVD), and molecular beam epitaxy (MBE). These techniques involve the evaporation or chemical reaction of source materials or precursors to form the desired SiNM on various substrates. However, achieving high crystalline quality with PVD and CVD methods can be challenging, and the epitaxial growth method requires a highly selective choice of substrate materials. Moreover, there are three mainstream methods for fabricating SiNMs on insulator films: separation by implantation of oxygen (SIMOX), bonding and etch-back SOI (BESOI), and Smart-Cut technology. 1) SIMOX involves implanting high-energy oxygen ions into a silicon wafer, followed by high-temperature annealing to form a buried oxide layer beneath a thin surface silicon layer, creating an SOI structure. 2) BESOI entails bonding a silicon wafer with an oxide-treated silicon wafer, followed by thinning the top silicon layer through grinding or chemical etching to achieve precise film thickness control. 3) Smart-Cut introduces hydrogen ions to a predetermined depth in the silicon wafer, where high-temperature annealing causes hydrogen bubbles to expand, splitting the silicon layer for transfer to another substrate. Epitaxy and SOI processes are the most common methods for preparing SiNMs, but they face challenges due to high costs, which impact industrialization and practical application. Currently, Lee et al.[60] have proposed a method based on interconnected trench patterns, which enables the repeated generation of high-area-density and thickness-controllable SiNM from a single-parent silicon wafer. This method combines anisotropic wet etching and deep reactive ion etching techniques, achieving precise control over film thickness (ranging from 300 nm to 13 µm) and area density (up to 90%). It shows promise in addressing the high cost and single-use limitations of traditional silicon thin-film transfer methods, such as SOI wafer transfer. In addition, methods such as electron beam deposition and magnetron sputtering are commonly used to deposit sacrificial layers and SiNMs onto substrates, enabling the rapid, large-scale production of releasable SiNMs. However, films deposited through PVD typically form amorphous or polycrystalline SiNMs,[50,61] which have relatively poor chemical stability and numerous grain boundaries, leading to suboptimal electrical performance. When considering transfer and processing, the deposition method should be chosen based on the specific requirements of the device.

Then, the fabrication methods of silicon nano-microstructures form the foundation for the integration of SiNM devices and systems. Among these, SOI transfer, selective etching and release (Undercut Etching), and metal-assisted chemical etching (MACE) exhibit unique advantages and limitations, creating a complementary and competitive technological landscape across different application scenarios. 1) SOI transfer technology releases the top silicon layer by selectively etching the intermediate oxide layer with hydrofluoric acid, which is then transferred onto flexible or heterogeneous substrates.[20a,30,62] The main advantage of this technique lies in the fully freestanding SiNM, which can conform to both rigid and non-rigid surfaces and degrade within biological environments, making it an indispensable material property for fabricating flexible devices. At the same time, it retains the excellent electrical and optical properties of single-crystal silicon and requires only wet etching and stamp transfer processes to transfer SiNM to the desired target substrate. The van der Waals forces and interfacial capillary forces at the thin-film-substrate interface allow SiNM to achieve stable adhesion on most substrates. However, the ultrathin thickness makes the mechanical behavior of SiNM difficult to control, especially since the transfer process is still predominantly manual. Imprecise operations may introduce cracks and wrinkles into the SiNM, thereby reducing its yield (**Figure 3a,b**). 2) Selective etching of local regions of a patterned sacrificial layer, also known as undercut etching, enables on-chip SiNM microstructure fabrication using conventional photolithography and deposition processes.[14b,50,63] This method typically employs deposition techniques to create a strain layer on the top of the SiNM, which induces local out-of-plane deformation due to the strain gradient along the thickness direction after etching. The fact that the SiNM remains attached to the substrate means that on-chip process integration can be achieved before partial detachment, allowing for

 © 2025 Wiley-VCH GmbH

16163028, 2025, 35, Downloaded from https://advanced.onlinelibrary.wiley.com/doi/10.1002/adfm.202502191 by Fudan University, Wiley Online Library on [08/03/2026]. See the Terms and Conditions (https://onlinelibrary.wiley.com/terms-and-conditions) on Wiley Online Library for rules of use; OA articles are governed by the applicable Creative Commons License

16163028, 2025, 35, Downloaded from https://advanced.onlinelibrary.wiley.com/doi/10.1002/adfm.202502191 by Fudan University, Wiley Online Library on [08/03/2026]. See the Terms and Conditions (https://onlinelibrary.wiley.com/terms-and-conditions) on Wiley Online Library for rules of use; OA articles are governed by the applicable Creative Commons License

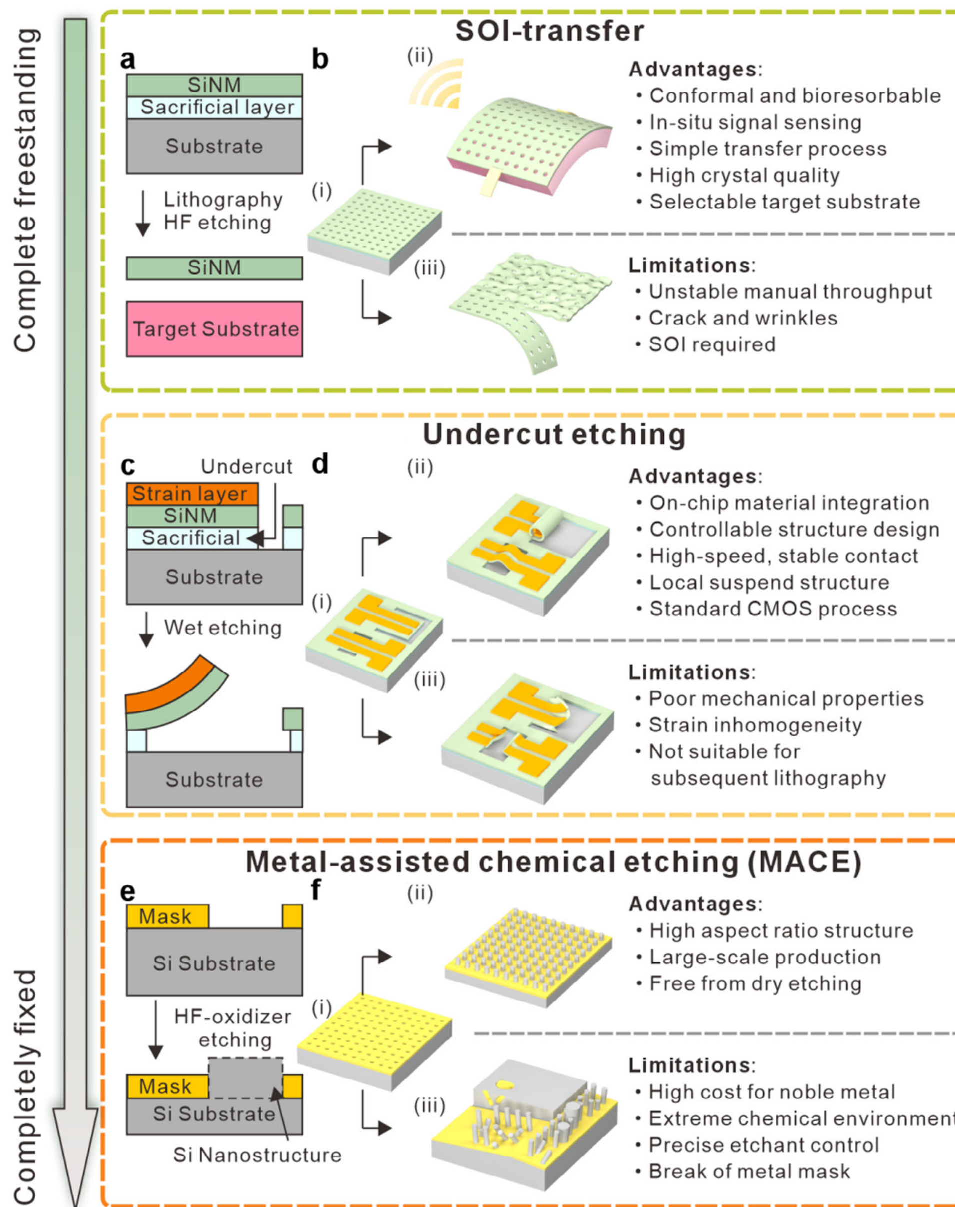

Figure 3. Preparation methods of SiNMs. a) Schematic diagram of SOI-transfer technique. b) Illustration of i) untransferred SOI, ii) advantages of transferred SOI, and iii) limitations of transferred SOI. c) Schematic diagram of undercut etching technique. d) Illustration of i) patterned SiNM/sacrificial layer structure, ii) advantages of undercut etching SiNM, and iii) limitations of undercut etching SiNM. e) Schematic diagram of MACE technique. f) Illustration of i) patterned metal mask/Si structure, ii) advantages of MACE etched SiNM, and iii) limitations of undercut etching SiNM.

high design freedom for patterns required by pre-defined structures. After local etching, the SiNM, which remains connected to the rigid substrate, is almost unaffected by the etching process, supporting stable contact and electrical input/output. However, in large-area fabrication, the edge non-uniformity of the strain layer may affect the formation of structures, and the mechanical fragility of the microstructures after etching does not support further photolithography definition, limiting its potential for subsequent post-processing (Figure 3c,d). 3) MACE uses noble metal catalysts (such as Au or Ag) in HF-oxidant solutions to induce localized redox reactions, enabling the efficient fabrication of silicon nanostructures with high aspect ratios (depth-to-width > 10:1).[64] Since this method uses bulk silicon as the substrate, the formation of structures depends only on the precision of the metal mask, making it suitable for large-scale fabrication without requiring dry etching devices such as reactive ion etching. However, the strong oxidizing agents and hydrofluoric acid require precise proportional combinations, and the choice of catalytic metals is limited to noble metals, which inevitably increases the experimental and application costs. During the etching process, the breakage or local defects of the metal mask may significantly alter the etching path of the pattern, imposing stringent

 © 2025 Wiley-VCH GmbH

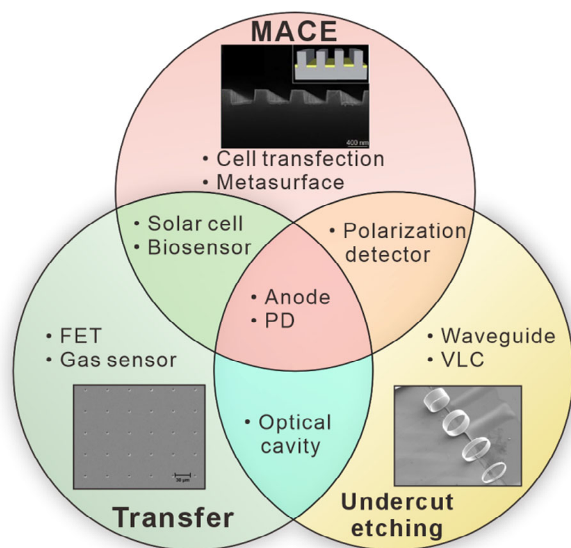

Figure 4. Application of different SiNM fabrication methods. Reproduced with permission.[59,74] Copyright 2012, American Chemical Society. Courtesy of Bofan Hu and Binmin Wu.

requirements on the cleanliness and uniformity of the etched surface (Figure 3e,f).

SiNM can be processed using the optimal method for specific fields by leveraging the advantages and addressing the limitations of the aforementioned three techniques (**Figure 4**). Notably, devices within the same application category can adopt different compatible processing approaches based on more specific requirements, providing diversified technical support for the development of next-generation electronic and optoelectronic devices. The transfer technique preserves the excellent electrical and optical properties of single-crystal silicon while imparting flexibility.[37b,60] This makes it particularly suitable for applications such as flexible gas sensors,[65] field-effect transistors,[63,66] solar cells,[35,67] and in situ biosensors.[20a,68] On the other hand, the undercut etching technique is mainly applied to on-chip integration of complex three-dimensional microstructures, making it ideal for highly integrated or multifunctional electronic/optoelectronic devices, such as cantilever waveguides[69] and visible light communication (VLC) devices.[21] The resulting three-dimensional structures can be tailored to meet wavelength or polarization detection requirements, forming optical microcavities[70] and polarization detectors.[14a] With its high-precision microstructure fabrication capabilities, SiNM enables efficient modulation and detection of optical signals. MACE technology excels in fabricating high aspect ratio nanostructures, addressing the needs of high specific surface area devices in fields such as optoelectronics and biology, including cell transfection,[71] metasurfaces,[72] and solar cells.[73] Correspondingly, anisotropic SiNM nanostructures can effectively couple with polarized electromagnetic waves. For battery anodes, the transfer process facilitates large-area single-layer SiNM, the curved SiNM formed by undercut etching increases ion sites within the same area, and MACE can create SiNM micropillars to enhance the specific surface area. In photodetectors, transferred SiNM is typically used for flexible photodetectors, undercut etching is suitable for multifunctional photodetectors, and MACE technology is ideal for high-absorption photodetectors. In summary, the cross-integration of these techniques in certain fields further broadens the application scope of SiNM, offering extensive technical support for the multi-functionalization and high performance of next-generation electronic and optoelectronic devices.

When it comes to the fabrication of SiNM devices, device processing based on two-dimensional (2D) thin-film morphologies is an important application direction. Therefore, studying the mechanical behavior of freestanding SiNM during transfer and undercut etching processes will provide a theoretical foundation for the design of device structures. The SiNMs can be transferred by stamps or deformed due to the intrinsic strain gradient. Understanding and analyzing the formation mechanisms of three-dimensional structures in strain-engineered SiNMs is crucial in their fabrication process. When fabricating out-of-plane buckled SiNMs using flexible substrates, the model typically adheres to the principles of elastic buckling (**Figure 5**a).[48] When utilizing the intrinsic strain of SiNMs for three-dimensional microstructure fabrication, the underlying principle typically involves exploiting mismatch from the lattice constants of material interfaces (Figure 5b), and thermal expansion coefficients of different NM layers (Figure 5c).[50] When the SiNM is subjected to compressive stress exceeding a certain critical value, it loses its equilibrium in the flat state and undergoes sudden deformation. Then, the SiNM is prone to perform out-plane deformation to reduce the strain energy (Figure 5d–f).[75] This behavior allows the film to transition from a high-energy equilibrium state to a more stable low-energy equilibrium state. The critical stress at which buckling occurs is generally calculated using the classical Euler buckling theory.[46c] In an ideal film model under uniaxial loading with simply supported boundary conditions, the bending moment equals the critical stress, and the relationship can be expressed as:[46c,77]

$$EI\,\frac{d^4 w(x)}{dx^4} = -P\frac{d^2 w(x)}{dx^2} \tag{3}$$

For an ideal buckling scenario with both ends fixed, the buckled shape typically takes the form of a sinusoidal function. The displacement of the buckled film can be described by:

$$w(x) = A\sin\left(\frac{n\pi x}{L}\right) \tag{4}$$

The characteristic equation for this buckling scenario, considering the sinusoidal displacement and boundary conditions, can be derived as follows:

$$P = \frac{EI(n\pi)^2}{L^2} \tag{5}$$

For a thin film with a rectangular cross-section, the moment of inertia (second moment of area) about the axis perpendicular to the plane of the film is given by:

$$I = \frac{bt^3}{12}\;\; P_{\mathrm{cr}} = \frac{\pi^2 E\left(\frac{bt^3}{12}\right)}{L^2} = \frac{\pi^2 Ebt^3}{12L^2} \tag{6}$$

 © 2025 Wiley-VCH GmbH

16163028, 2025, 35, Downloaded from https://advanced.onlinelibrary.wiley.com/doi/10.1002/adfm.202502191 by Fudan University, Wiley Online Library on [08/03/2026]. See the Terms and Conditions (https://onlinelibrary.wiley.com/terms-and-conditions) on Wiley Online Library for rules of use; OA articles are governed by the applicable Creative Commons License

16163028, 2025, 35, Downloaded from https://advanced.onlinelibrary.wiley.com/doi/10.1002/adfm.202502191 by Fudan University, Wiley Online Library on [08/03/2026]. See the Terms and Conditions (https://onlinelibrary.wiley.com/terms-and-conditions) on Wiley Online Library for rules of use; OA articles are governed by the applicable Creative Commons License

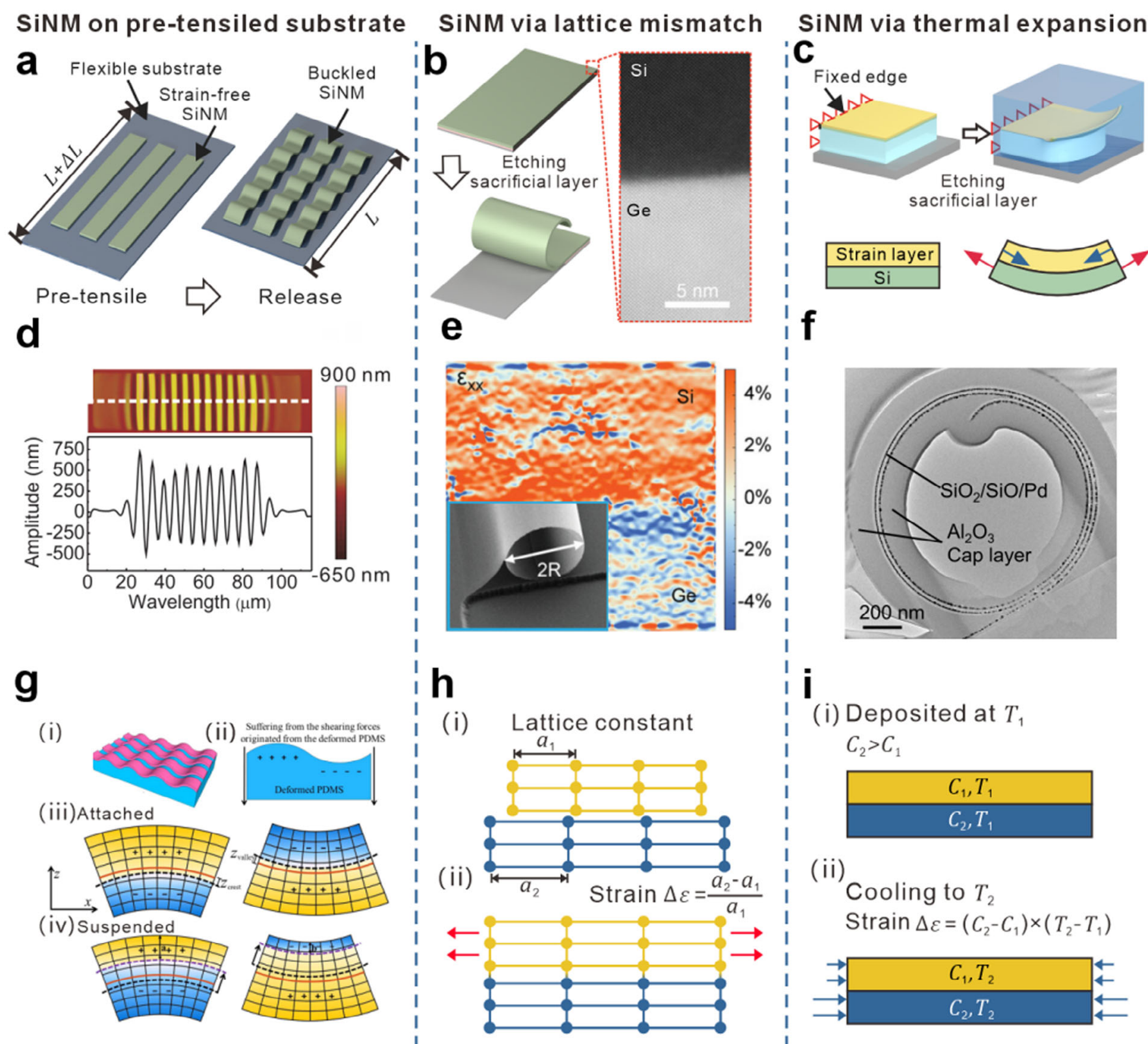

Figure 5. Fabrication of SiNM microstructures. a) Diagram of the formation of buckle SiNMs. b) Schematic of fabrication of rolled-up epitaxial SiNMs. c) Mechanism of 3D construction of rolled-up SiNM microstructures. Reproduced with permission.[50] Copyright 2024, Springer Nature. d) AFM image and amplitude curve of a wrinkle SiNM.[75] e) Strain distribution in epitaxial SiNM and SEM image of rolled-up c-Si microtube Reproduced with permission.[14a] Copyright 2023, Wiley-VCH. f TEM image of cross-sectional SiO_2/Si/Pd NM microtube. Reproduced with permission.[76] g) Strain distribution in attached SiNM/PDMS, and suspended SiNM/PDMS. e,g) Reproduced with permission.[75] Copyright 2013, American Institute of Physics. h) Mechanism of strain gradient via the difference between thermal expansion coefficients: i) NMs deposited at T_1; ii) NMs cooled to T_2. h) GPA analysis of strain ϵ_{xx} in epitaxial SiNM microtubes. i) Lattice constant of two layers of NMs; ii) NMs and strain gradient after epitaxy. i) Mechanism of strain gradient via lattice mismatch of a_1 and a_2.

Considering the boundary conditions with the effective length factor k, the critical buckling stress can be expressed as:

$$\sigma_{cr} = \frac{\pi^2 E}{(kL/t)^2 (1-\nu^2)} \tag{7}$$

After buckling deformation occurs (Figure 5g), the strain distribution in the thickness direction of the SiNM will also exhibit periodic variation, which can be expressed as:

$$\varepsilon_{xx}(x,y,z) = \varepsilon^0_{xx} + \frac{1}{4}k^2A^2 + \frac{1}{2}Ak^2\cos(kx)\,z \tag{8}$$

The position of natural surface is:[75,78]

$$z = \begin{cases} -\frac{\varepsilon^0_{xx}+\frac{1}{4}k^2A^2}{\frac{1}{2}Ak^2} < 0, \text{at the crest,} & \text{and } \cos(kx) = 1 \\ \frac{\varepsilon^0_{xx}+\frac{1}{4}k^2A^2}{\frac{1}{2}Ak^2} > 0, \text{at the valley,} & \text{and } \cos(kx) = -1 \end{cases} \tag{9}$$

In-situ preparation of SiNMs in conjunction with other NM systems can be achieved through methods such as electron beam evaporation and magnetron sputtering. During the deposition process, both the substrate and the deposited material are typically at high temperatures. Upon cooling to room temperature,

 © 2025 Wiley-VCH GmbH

the substrate and material undergo contraction. Meanwhile, the difference between deposition temperature and room temperature, coupled with the variance in thermal expansion coefficients of the materials in each NM layer, leads to the formation of a strain gradient across the layers upon cooling after deposition (Figure 5i).[50,76]

$$\Delta\varepsilon = \left(C_2 - C_1\right) \times \left(T_2 - T_1\right) \tag{10}$$

Here, C_1 and C_2 represent the thermal expansion coefficients of the materials, while T_1 and T_2 correspond to the deposition temperature and room temperature, respectively. This strain introduction method is commonly employed in the fabrication of self-rolling structures in amorphous SiNMs and silicon dioxide films.[34,76]

For single-crystalline SiNMs, the self-rolling behavior typically derives from strain induced by lattice constant mismatches during epitaxial growth with other film layers or from strain difference between regions near and far from the epitaxial interface within the film (Figure 5h).[14a] The resulting strain gradient is expressed as:

$$\Delta\varepsilon = \frac{a_2 - a_1}{a_1} \tag{11}$$

In typical SiNMs self-rolling processes, strain usually originates from both aforementioned factors simultaneously,[14a,b,79] as the deposition of electrodes during device fabrication introduces differences in temperature and material systems.

It is important to note that the deformation behavior of NMs under strain is closely related to their boundary conditions.[80] Beyond the commonly observed effects on out-of-plane deformation in cantilever and simply supported beam structures, the deformation state of a film in a single-ended supported condition is also significantly influenced by the length of the unconstrained film. Cendula et al.[46a,81] investigated the theoretical deformation model of bilayer NMs and found that when the film undergoes initial release—specifically at an etching depth of only 1–3 µm—even under a small strain gradient, cantilevered NMs tend to buckle and exhibit wrinkling (Figure 5j,k). In contrast, when the NM begins to roll, a planar strain model is considered, where the balance of forces and moments plays a critical role.[49a,82]

$$y_i = \sum\nolimits_{i=1}^{n} t_i \tag{12}$$

In the plane-strain model, there are:

$$\sigma_y = 0 \tag{13}$$

$$\varepsilon_z = \frac{1}{E}\left(\sigma_z - \nu\sigma_x\right) + \varepsilon^0 = 0 \tag{14}$$

In uniform bending, the strain in the rolling direction is distributed linearly through the thickness:

$$\varepsilon_x = c + \frac{y - y_b}{R} \tag{15}$$

y_b is the neutral plane of bending. Combined with the stress-strain relationship, we have:

$$\sigma_x = \frac{E}{1-\nu^2}\left[\varepsilon_x - (1+\nu)\,\varepsilon^0\right] \tag{16}$$

$$\sigma_x = \frac{E}{1-\nu^2}\left(c + \frac{y - y_b}{R} - (1+\nu)\,\varepsilon^0\right) \tag{17}$$

After the self-rolling process, the forces in the multilayer NM are balanced again. For the uniform strain:

$$\sum\nolimits_{i=1}^{n} \frac{E_i}{1-\upsilon_i^2} t_i \left(c - \left(1+\upsilon_i\right)\varepsilon_i^0\right) = 0 \tag{18}$$

For the bending strain, the balance equation can be written as:

$$\sum_{i=1}^{n} \int_{y_{i-1}}^{y_i} \frac{E_i}{1-\upsilon_i^2} \frac{\left(y - y_b\right)}{R} \mathrm{d}y = 0 \tag{19}$$

The balance in the bending moment is:

$$\sum_{i=1}^{n} \int_{y_{i-1}}^{y_i} \frac{E_i}{1-\upsilon_i^2} \left(c + \frac{y - y_b}{R} - \left(1+\upsilon_i\right)\varepsilon_i^0\right)\left(y - y_b\right) dy = 0 \tag{20}$$

Solving Equations (12)–(14) together, we can get:

$$c = \frac{\sum_{i=1}^{n} \frac{E_i}{1-\upsilon_i^2} t_i \varepsilon_i^0}{\sum_{i=1}^{n} \frac{E_i}{1-\upsilon_i^2} t_i} \tag{21}$$

$$t_b = \frac{\sum_{i=1}^{n} \frac{E_i}{1-\upsilon_i^2} t_i \left(y_i + y_{i-1}\right)}{2\sum_{i=1}^{n} \frac{E_i}{1-\upsilon_i^2} t_i} \tag{22}$$

$$\frac{1}{R} = \frac{3\sum_{i=1}^{n} \frac{E_i}{1-\upsilon_i^2} t_i \left(y_i + y_{i-1} - 2t_b\right)\left(c - \left(1+\upsilon_i\right)\varepsilon_i^0\right)}{2\sum_{i=1}^{n} \frac{E_i}{1-\upsilon_i^2} t_i \left[y_i^2 + y_i y_{i-1} + y_{i-1}^2 - 3t_b\left(y_i + y_{i-1} - t_b\right)\right]} \tag{23}$$

Based on the deformation description of SiNM systems from the aforementioned formulas, researchers can use numerical methods to design specific microstructures, providing a cost-effective and efficient validation approach.[84] Liu et al.[83] explored the nonlinear buckling and delamination behavior between rigid SiNM systems and soft substrates based on interfacial mechanics. By precisely designing the pre-strain of the elastic substrate and the length of the SiNM, complex 3D structures can be generated from 2D planar patterns, with corresponding phase diagrams analyzed. Model predictions of buckling and delamination behavior in various geometrical structures offer effective strategies for applying SiNMs in fields such as MEMS, photonic devices, and bio-integrated sensors (**Figure 6a**). Cheng and colleagues[32] proposed a method for achieving designated 3D film surfaces through microlattice design. This strategy controls material "porosity" to adjust its effective stiffness via a bidirectional design and modeling simulation feedback mechanism based on machine learning and regulates pre-strain on preset flexible substrates to achieve structural fabrication (Figure 6b).

© 2025 Wiley-VCH GmbH

16163028, 2025, 35, Downloaded from https://advanced.onlinelibrary.wiley.com/doi/10.1002/adfm.202502191 by Fudan University, Wiley Online Library on [08/03/2026]. See the Terms and Conditions (https://onlinelibrary.wiley.com/terms-and-conditions) on Wiley Online Library for rules of use; OA articles are governed by the applicable Creative Commons License

16163028, 2025, 35, Downloaded from https://advanced.onlinelibrary.wiley.com/doi/10.1002/adfm.202502191 by Fudan University, Wiley Online Library on [08/03/2026]. See the Terms and Conditions (https://onlinelibrary.wiley.com/terms-and-conditions) on Wiley Online Library for rules of use; OA articles are governed by the applicable Creative Commons License

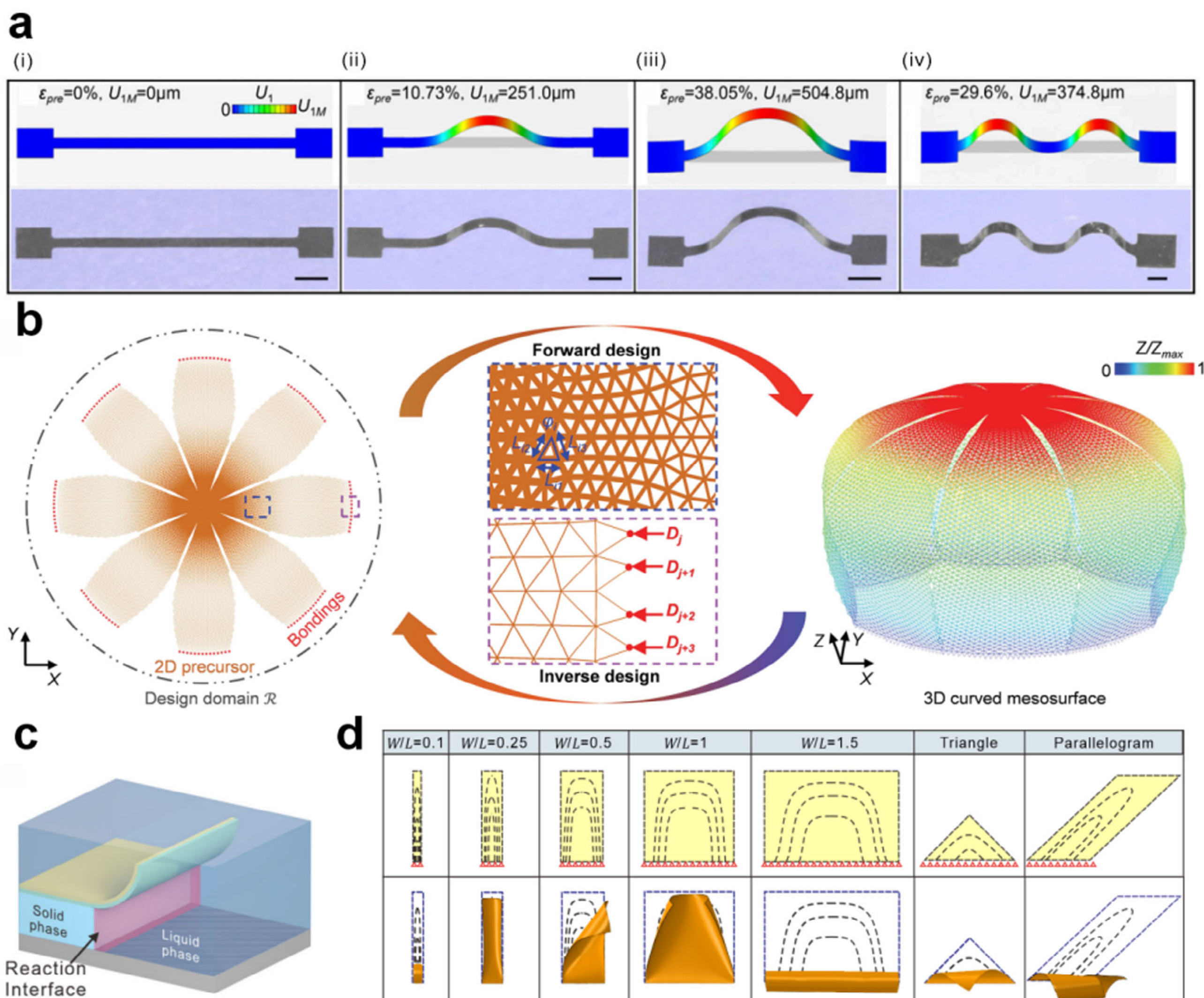

Figure 6. Numerical method and simulation of SiNM microstructures design. a) Experimental results and FEM simulation results of different construction modes in SiNM ribbons. Reproduced with permission.[83] Copyright 2019, National Academy of Sciences. b) Diagram of forward and inverse design of 3D microlattice NM mesosurfaces. Reproduced with permission.[32] Copyright 2023, AAAS. c) Chemical reaction model of rolled-up NMs. d) Schematics Si/Cr NMs with different sizes. Reproduced with permission.[50] Copyright 2024, Springer Nature.

This approach enables SiNM scaffolds to achieve customizable conformal assembly according to target morphologies, holding great potential in biomedical and microrobotics applications. Therefore, in the fabrication of SiNM microtube structures, it is common practice to utilize epitaxial layers or introduce additional strained layers to achieve a greater strain gradient. It is noteworthy that the formation of buckled structures and microtube structures depends not only on the minimization of the elastic energy but also on the actual boundary conditions. Zhang et al.[50] used Si/Cr NMs as an example and investigated the factors influencing the forming process of NMs. This study proposed an ideal model that considers the gradual change in boundaries during the sacrificial layer etching process, considering the effects of the aspect ratio of the pattern and the penetration angle of the etchant on self-rolling behavior. The orientation of etchant penetration varies with different aspect ratios, leading to the formation of various symmetrical and asymmetrical self-rolling structures. Under the influence of these factors, efficient design of three-dimensional structures can be achieved by adjusting the aspect ratio of patterns and conducting finite element pre-modeling (Figure 6c,d). The analysis of the forming process and mechanical theories of SiNMs will provide valuable guidance for subsequent device functionality and mechanical performance design, improving experimental efficiency while reducing costs.

The strain in SiNMs is crucial for predicting and validating their mechanical,[85] electrical[86] properties, and final forming states. Current methods for characterizing strain in SiNMs mainly include Raman spectroscopy, X-ray diffraction, and transmission electron microscopy. Raman spectroscopy infers strain by analyzing changes in the vibration frequency of Si–Si bonds in the silicon lattice. Tensile strain in the film shifts the Raman peak to lower frequencies, while compressive strain shifts it to higher frequencies. The unstrained Si-Si bond Raman peak is

 © 2025 Wiley-VCH GmbH

located at 520 cm^{-1}, and its displacement relation can be expressed as:[87]

$$\Delta\omega = b\varepsilon \quad (24)$$

where b represents the strain shift coefficient, allowing the calculation of actual strain based on the displacement of the Raman peak. This method can be applied to the characterization of stretchable devices, wrinkled devices, and rolled devices using SiNMs.[14a,57,88]

X-ray diffraction is also utilized to calculate the strain state by analyzing the characteristic changes in the diffraction peak position of the SiNM lattice.[89] When the $\epsilon = 0$, there is:

$$n\lambda = 2d_0 sin\theta \quad (25)$$

when the $\varepsilon \neq 0$, the shift of diffraction peak is $n\lambda = 2d_0(1 + \epsilon)\sin\theta'$. Since the film strain is very small, the shift can be approximated as $\theta' \approx \theta(1 + \epsilon)$, with the corresponding change in the diffraction angle is:

$$\Delta\theta \approx \theta\varepsilon \quad (26)$$

In X-ray diffraction (XRD), Reciprocal Space Mapping (RSM) serves as an advanced characterization technique that performs 2D scans of the crystal in reciprocal space, using diffraction and incident angles. This provides comprehensive information about the sample in reciprocal space. Compared to XRD, RSM can also reveal details about crystal quality, dislocation density, structural defects, and lattice curvature, enabling detailed analysis of strain along the thickness direction in SiNMs.[90] However, XRD struggles to analyze strain in amorphous SiNMs due to their highly disordered structure, which nearly eliminates diffraction peaks. Currently, transmission electron microscopy (TEM), a direct method for stress–strain analysis, allows for detailed examination of SiNMs through lattice fringe imaging. TEM can also analyze the crystallinity of SiNMs (whether single-crystal, polycrystalline, or amorphous) via diffraction patterns, with some research focusing on the strain in amorphous silicon-based nanofilms.[76,91] High-angle annular dark-field scanning TEM (HAADF-STEM) offers higher-resolution atomic-level imaging compared to TEM, enabling direct measurement of lattice spacing in SiNMs, making it one of the most ideal techniques for morphology characterization and strain analysis.[14a,50] At present, researchers can select appropriate characterization methods based on the crystal quality and structural morphology of SiNMs, ensuring a good correlation between experimental results and theoretical simulations.

3. SiNMs for Photodetection

In the field of photodetection, silicon is the most common material used in mature device fabrication processes. However, continuous advancements in technology have imposed higher demands on the performance and functionality of optoelectronic devices, such as multidimensional optical information detection (including angle, wavelength, and polarization), conformal detection, and in situ detection. Traditional bulk silicon optoelectronic devices typically rely on complex planar structure designs or additional optical components to achieve multidimensional optical information detection,[9a,92] while conformal detection is hard to realize due to the high bending stiffness of bulk silicon, which makes adherence challenging. As an ideal solution, SiNMs can compensate for the limitations of bulk silicon and planar photodetectors through their nearly non-degrading electrical performance after desorption from the substrate. This can be achieved via conformal light-sensitive arrays or microstructures with anisotropic responses to external optical signals. Additionally, SiNM offers a method to modulate the energy band of device via external forces or strain, thereby expanding the spectral range of silicon semiconductor devices for detection. This provides a "more-than-Moore" approach to designing optoelectronic devices, offering new possibilities (as shown in **Table 1**).[93]

3.1. Self-Rolled and Tensile-Strained SiNM Optoelectronics

According to the Beer–Lambert absorption law, the light absorption of nanoscale planar SiNM photodetectors is significantly weaker than that of bulk silicon, which has a critical impact on the sensitivity of photodetectors. However, thin film under strain engineering forms curved structures due to strain, enabling the convergence and multiple reflections of incident light.[100] This not only allows light to undergo multiple absorptions within the cavities formed by the NM but also grants the capability to detect additional information such as polarization and direction.[100b,101] SiNM-based photodetectors in microtube structures can achieve near-all-angle detection of incident light on the detection surface perpendicular to the tube axis. Xu et al.[14b] fabricated a microtube photodetector using single-crystalline SiNMs on SOI and Cr metal electrodes. In this device, the strain gradient was formed due to the difference in thermal expansion coefficients between the Cr layer and the SiNM, as well as the temperature differential during cooling. The tube diameter could be tuned by adjusting the thickness of the Cr layer. The rolled microtube structure can act as a microcavity that captures incident light and allows for multiple reflections, further enhancing the photoresponse. Additionally, the increased surface states following rolling help capture charges and reduce dark current, thereby overall enhancing the photoconductive on-off ratio. Moreover, the resulting microtube demonstrated an ultra-wide undistorted detection angle of nearly 150°, significantly greater than the mere 60° angle achievable in planar devices. Wu et al.[14a] developed a microtube photodetector using SiNMs epitaxially grown on Ge and Cr/Au electrodes, where the self-rolling strain primarily originate from lattice mismatch in epitaxy (**Figure 7a**). This device exhibited effective photoresponse from 400 to 1000 nm (Figure 7b). In this microtube detector, the spatial anisotropy of the microtube structure provided excellent detection capability for incident polarized light, achieving a polarization detection ratio of 1.42 at 830 nm, revealing potential for three-dimensional micro-structured semiconductor photodetectors in multidimensional optical information detection (Figure 7c). Zhang et al.[50] using a FEM-guided three-dimensional microstructure design approach, designed multiple types of three-dimensional photodetectors, including planar detectors, utilizing an amorphous silicon/Cr NM system (Figure 7d). By enhancing the spatial anisotropy of the structures, they achieved differential detection of the incident light angle (Figure 7e). This study collected

© 2025 Wiley-VCH GmbH

16163028, 2025, 35, Downloaded from https://advanced.onlinelibrary.wiley.com/doi/10.1002/adfm.202502191 by Fudan University, Wiley Online Library on [08/03/2026]. See the Terms and Conditions (https://onlinelibrary.wiley.com/terms-and-conditions) on Wiley Online Library for rules of use; OA articles are governed by the applicable Creative Commons License

16163028, 2025, 35, Downloaded from https://advanced.onlinelibrary.wiley.com/doi/10.1002/adfm.202502191 by Fudan University, Wiley Online Library on [08/03/2026]. See the Terms and Conditions (https://onlinelibrary.wiley.com/terms-and-conditions) on Wiley Online Library for rules of use; OA articles are governed by the applicable Creative Commons License

Table 1. Comparison between SiNM photodetectors.

Device structure	Wavelength [nm]	Responsivity	Response time	Additional feature	Refs.
3D tubular SiNM on insulator photodetector	780–1450 nm	–	–	Wide-angle light incident detection (20°–160°)	[14b]
3D tubular epitaxial SiNM photodetector	400–1100 nm	330 mA W^{-1}@ 700 nm	370 µs (rise)/ 440 µs (decay)	Dichroic ratio of 1.24 @ 940 nm and wide-angle light incident detection over ±75°	[14a]
a-SiNM/Cr bilayer photodetectors	400–800 nm	60 mA W^{-1}	≈100 µs	Direction detection accuracy with a resolution of 10°	[50]
Biaxial strain SiNM photodetector	SWIR	62.37 mA W^{-1}@980 nm	–	Enhanced photosensitivity under biaxial strain for SWIR detection	[44]
ZnO nanowires /honeycomb-structured SiNM	365–1100 nm	–	11 ms (rise)/12 ms (decay)	Wide-angle light incident detection over ±75°with flexibility	[93b]
SiNM back-gate TFT	400–700 nm	52 A W^{-1}	≈50 µs (rise)/≈110 µs (decay)	Stable responsivity with less than 5% variation under bending of 15 mm radius	[94]
n-channel SiNM MOSFETs on 3D architecture	Visible	–	–	Robustness under bending and shearing conditions	[31]
Hemispherical focal plane array with SiNM p-i-n photodiodes	543 nm; 594 nm; 633 nm	9.49 mA W^{-1}@543 nm, 6.24 mA W^{-1}@ 594 nm, 5.26 mA W^{-1}@ 633 nm	–	Conformal and wide-angle array photodetection	[95]
crumpled Si SiNM	405–1310 nm	≈33 mA W^{-1}@ 1310 nm	–	Strain-induced bandgap modulation for near-infrared (NIR) detection.	[30]
CdSe/ZnS QD on Back-gate SiNM FET	585–605 nm	≈0.1 A W^{-1}	–	Combination of photogating effect and photoconductive gain from QD	[96]
Suspended SiNM bolometer/cross-diabolo antenna	LWIR	114 mA W^{-1} @12.2 µm	>10 kHz	Low pixel pitch with high-speed infrared response	[20b]
NPN SiNM ribbon	450 nm	24.325 mA W^{-1}	≈50 ms	Large-scale production for SiNM array	[38]
Nanoroughened SiNM photodetector	980 nm	–	–	Dark current suppression with current on/off ratio of 10^4	[18a]
SiNM/P3HT/PbS QDs	375 nm, 532 nm, and 1342 nm	–	15.1 s	Capable of brightness and color perception	[97]
SiNM/ surface plasmon nanogroove	1550 nm	7 mA W^{-1}@1550 nm	–	High on/off current ratio in the negative photodetection	[98]
SiNM on optical fiber	633 nm	–	ms-level	Conformal coverage on bending surface	[99]

responses from various structured photodetectors to incident light from different directions and achieved incident light angle detection accuracy rates of 83% and 71% using deep neural networks, thereby avoiding the complexity of traditional CMOS process design (Figure 7f,g). In addition, although external strain-based SiNM cannot induce uniform large deflections in the film, its control methods typically offer variability and high precision. Therefore, strain can be applied to the attached substrate according to the actual optoelectronic detection requirements, enabling real-time, adjustable design of device performance. Katiyar et al.[44] processed SiNMs through external strain engineering, where biaxial tensile strain narrowed the optical bandgap of silicon, thereby extending its long-wave detection range. By applying the tensile strain using a pneumatic chamber, the SiNM detection range was extended to 1550 nm under ≈3.5% strain. Additionally, spherical SiNMs adhered to a pneumatic chamber can serve as hemispherical electronic eye arrays, offering new insights for LiDAR sensing and imaging systems (Figure 7h,i). In the future, the anisotropic characteristics of SiNM microtube structures can be further enhanced by integrating polarization-sensitive materials and plasmonic structures, thereby increasing the information detection density across material, structure, and device levels. This approach offers a new paradigm for next-generation visible/infrared photodetectors with advanced capabilities for wavelength, polarization, and direction detection.

© 2025 Wiley-VCH GmbH

16163028, 2025, 35, Downloaded from https://advanced.onlinelibrary.wiley.com/doi/10.1002/adfm.202502191 by Fudan University, Wiley Online Library on [08/03/2026]. See the Terms and Conditions (https://onlinelibrary.wiley.com/terms-and-conditions) on Wiley Online Library for rules of use; OA articles are governed by the applicable Creative Commons License

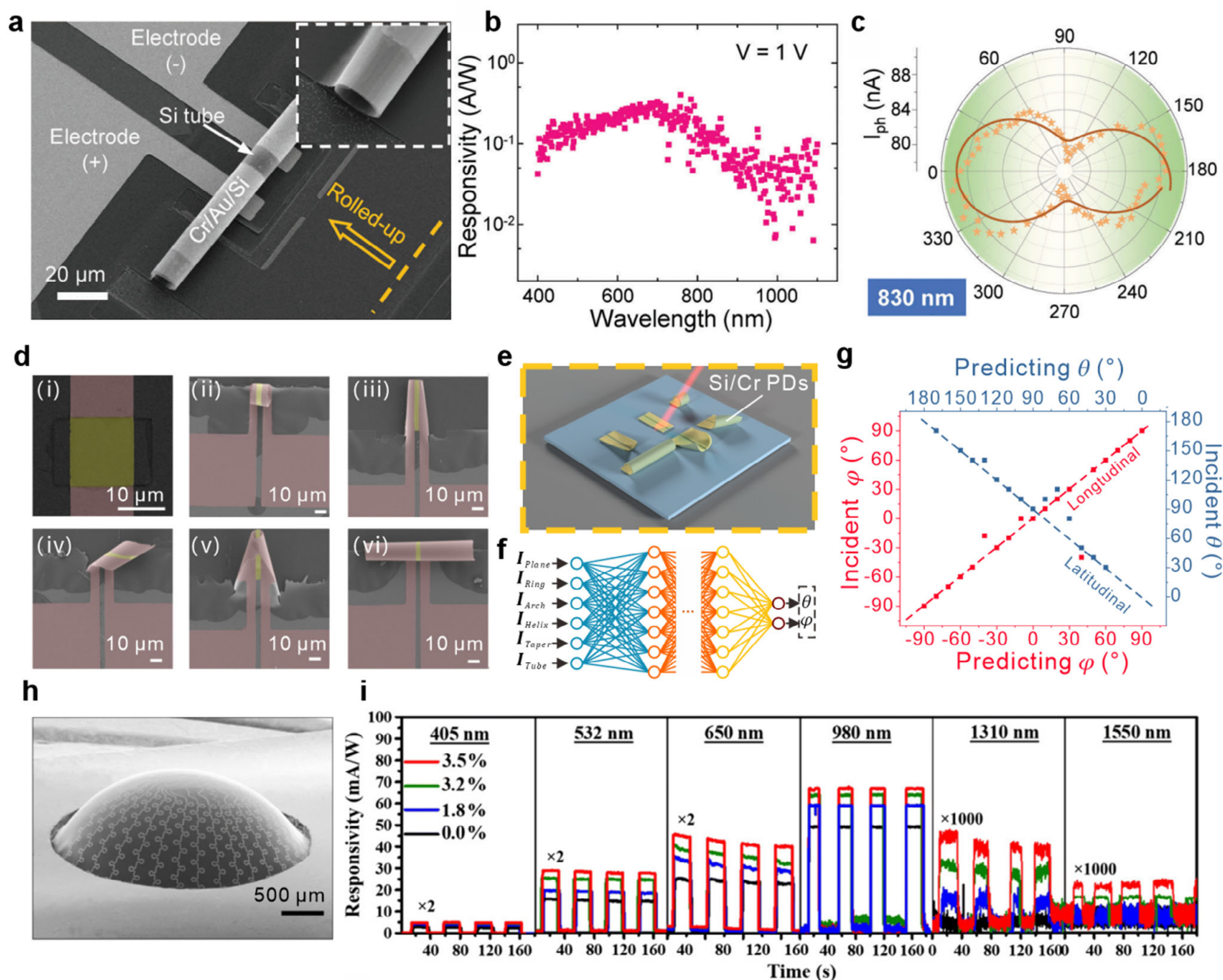

Figure 7. Self-rolled and tensile-strained SiNM photodetectors. a) SEM image of the rolled-up epitaxial SiNM photodetector. b) Responsivity-wavelength curve of rolled-up epitaxial SiNM photodetector. c) Photocurrent of 830 nm linear polarization light via epitaxial SiNM photodetector. Reproduced with permission.[14a] Copyright 2023, Wiley-VCH. d) Multiple structures of Si/Cr NM photodetectors. e) Schematic of directional photodetection of Si/Cr NM photodetectors. f) Diagram of neural network for direction identification via Si/Cr NM photodetectors. g) Angle identification of incident angle in longitudinal and latitudinal directions via neural network. Reproduced with permission.[50] Copyright 2024, Springer Nature. h) SEM image of the strained SiNM photodetector array on a PI substrate. i) Responsivity of the pressure-controlled SiNM photodetector array in various wavelengths. Reproduced with permission.[44] Copyright 2020, AAAS.

3.2. Buckled and Strain-Free SiNM Optoelectronics

SiNMs based on buckling or strain-free designs are primarily aimed at addressing challenges related to conformal attachment to complex surfaces and deformable sensing, which also benefit from the strong interaction of the SiNM interfaces.[96,102] Wrinkling in SiNM microstructures allows the device to achieve a higher absorption area under the same illumination projection area and improves robustness against external forces. When combined with buckle structures, the SiNM can release energy through out-of-plane warping in response to in-plane compressive strain, minimizing impact on device performance. Seo et al.[94] proposed a flexible phototransistor based on single-crystalline SiNMs, utilizing a flexible PET substrate. The introduction of a top silicon structure avoids the obstruction of light by metal layers or other materials, and the design of the detection layer enables sensitive detection across different wavelengths, achieving effective detection even under bending conditions (**Figure** 8a). Kim et al.[31] introduced a method for creating three-dimensional structures of SiNM MOSFETs and diode arrays through a buckling technique on a stretched elastic substrate. The serpentine design of the buckled structure ensures that strain during bending and deformation is primarily absorbed by the buckled connecting structures, preventing damage to the device while maintaining consistent performance (Figure 8b,c). This design is suitable for integration in optoelectronics and biomedical applications.

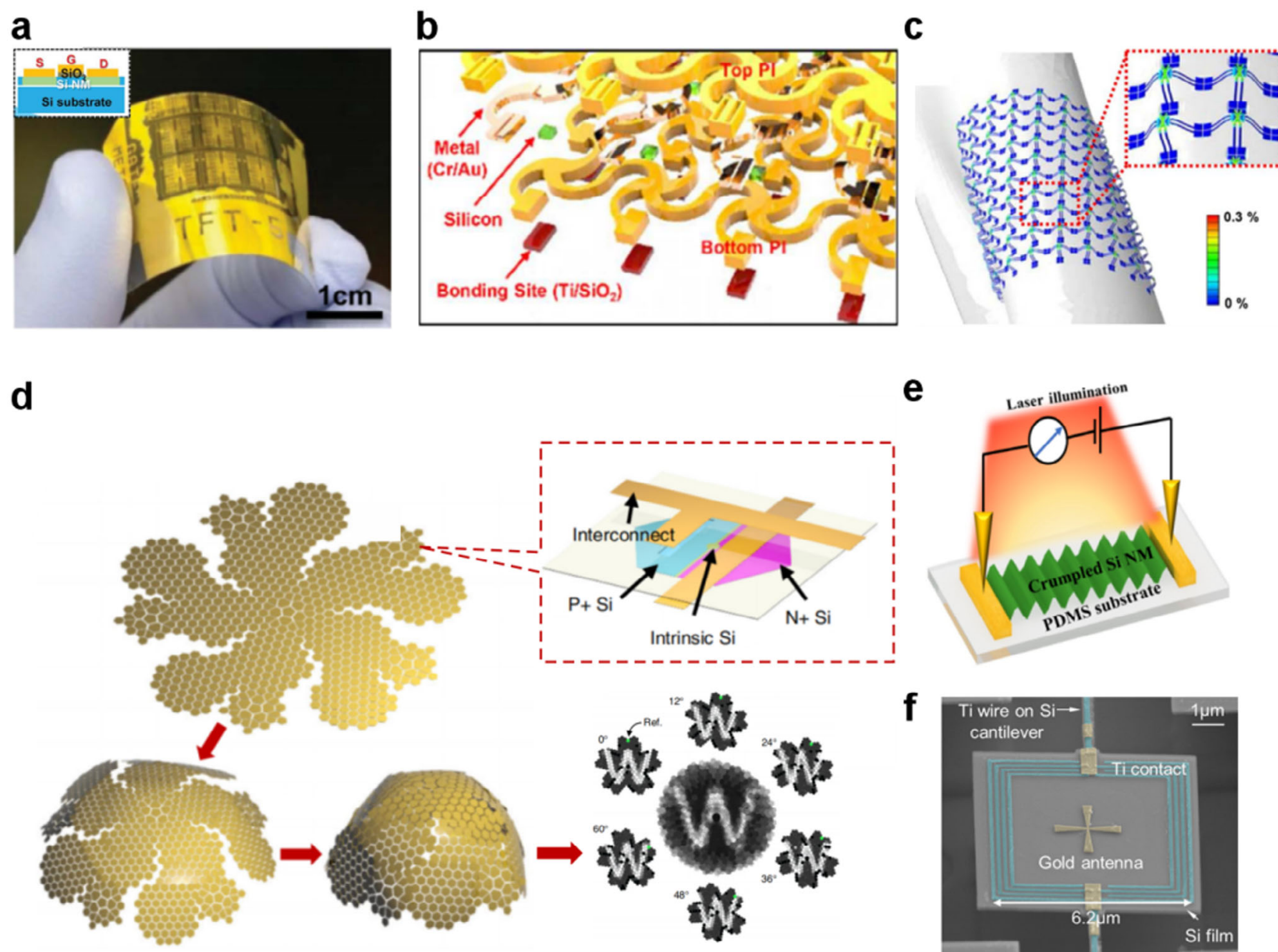

Figure 8. Design and performance of SiNM buckled and flexible structure photodetectors. a) Photograph of bending SiNM phototransistor. Reproduced with permission.[94] Copyright 2016, Wiley-VCH. b) Schematic of an integration of SiNM n-MOS and diodes on an un-buckled elastomer substrate. c) FEA simulation of strain distribution of buckled SiNM array on a bending and shearing elastomer substrate. Reproduced with permission.[31] Copyright 2018, American Chemical Society. d) Diagram and optical image of a SiNM photodiodes unit in the electronic eyes. Reproduced with permission.[95] Copyright 2017, Springer Nature. e) Diagram of wrinkled SiNM photodetectors.[30] Copyright 2024, AAAS. f) SEM image of SiNM-based micro-bridge bolometer. Reproduced with permission.[20b] Copyright 2021, American Chemical Society.

Strain-free SiNMs can also achieve the desired conformal coverage functionality through the design of flexible substrates or suspended structures.[103] Zhang et al.[95] presented a silicon-based photodetector array for a hemispherical electronic eye system, utilizing origami techniques. Compared to planar sensors, this design offers advantages in wide field-of-view and low image distortion. The electronic eye uses polygonal blocks as sensor pixels, folding the silicon-based device into a truncated icosahedral mesh, which is then folded into a hemisphere, enabling the creation of a hemispherical focal plane array imaging system without the need for complex external optical components (Figure 8d). Wang et al.[69b,104] achieved infrared light response at a wavelength of 1310 nm by compressing SiNMs on SOI, creating wrinkles and buckling that surpass the intrinsic absorption limits of silicon. The local strain within the wrinkled structures led to bandgap modulation, extending the range of light absorption. These wrinkled structures can be integrated into focal plane imaging systems. SiNMs have also found extensive applications in the optical field due to their transferability and process compatibility (Figure 8e). Chen et al.[20b] designed a SiNM-based micro-bridge bolometer for long-wave infrared (LWIR) light detection. The micro-bridge structure significantly reduces the thermal capacity of the device, enhancing the response time of photodetection and operating frequency. The device incorporates a compact cross-antenna design, which further improves infrared light absorption efficiency, with a pixel size of just 6.2 μm × 6.2 μm, and a thermal time constant (TTC) below 16 μs, making it at least 500 times faster than commercial amorphous silicon and vanadium oxide detectors (Figure 8f). Qu et al.[38] analyzed the adhesion energy between elastic stamps and SiNM ribbons, designing specific rectangular stamps. Through a repeated wet-etching-selective transfer process, they successfully achieved large-scale and reproducible SiNM ribbon assembly. This stamp-based approach enables large-scale vertical junction device integration on SiNMs and other inorganic thin-film systems.

© 2025 Wiley-VCH GmbH

16163028, 2025, 35, Downloaded from https://advanced.onlinelibrary.wiley.com/doi/10.1002/adfm.202502191 by Fudan University, Wiley Online Library on [08/03/2026]. See the Terms and Conditions (https://onlinelibrary.wiley.com/terms-and-conditions) on Wiley Online Library for rules of use; OA articles are governed by the applicable Creative Commons License

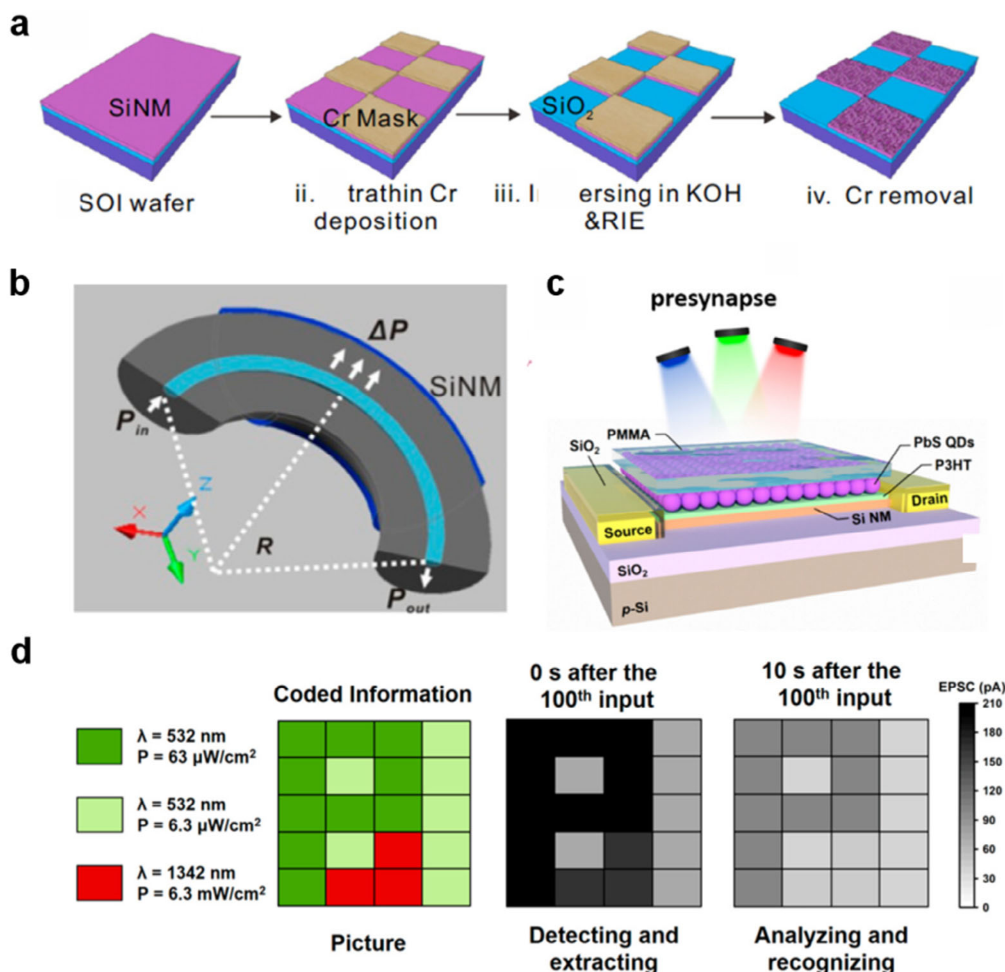

Figure 9. SiNMs for surface texturing and photonic applications. a) Illustration of the preparation of nanoroughed SiNM. Reproduced with permission.[18a] Copyright 2018, American Chemical Society. b) Schematic diagram of SiNM-wrapped single-mode fiber for loss detection. Reproduced with permission.[99] Copyright 2017, American Chemical Society. c) Diagram of a synaptic phototransistor based on SiNM/P3HT/PbS QDs. d) Detection, extraction, analysis, and recognition of a coded pattern by SiNM/P3HT/PbS QDs phototransistor. Reproduced with permission.[97] Copyright 2023, American Chemical Society.

Surface roughness and textures of SiNMs can also significantly impact their optoelectronic properties.[98,105] The goal of these two processing methods is to fabricate micro-nanostructures on SiNMs on rigid substrates, increasing the interfacial specific surface area, thereby altering the contact state and modulating thermal transport properties. Pan et al. achieved controllable nanoscale roughening through metal mask chemical etching without significantly altering the thickness of the SiNM. This treatment enhanced the Schottky barrier and reduced surface state recombination, thereby significantly lowering the dark current and improving the on-off ratio of photodetectors (**Figure** 9a,b).[18a] Pennelli et al. introduced surface roughness through nanoparticle doping and chemical etching, reducing thermal conductivity in primary heat transfer regions while maintaining electrical conductivity. This is because the rough surface of SiNM scatters phonons to suppress thermal conductivity without significantly affecting electron transport, presenting new opportunities for thermoelectric device development.[106]

SiNMs can also couple with planar photonic devices or conventional optical signal processing systems to enable in-situ optical modulation, detection, and selection.[34,107] Song et al.[99] designed a flexible photodetector by wrapping SiNM around an optical fiber to detect light leakage during fiber bending (Figure 9e). This device can detect bending curvatures with light leakage as high as 0.5 cm^{-1} without obvious mechanical strain, overcoming the limitations of traditional power meters that can only perform non-in situ detection at the input and output ends. This offers an effective method for performance monitoring in optical fibers, flexible photonic devices, and chips (Figure 9b). Its ultrathin nature allows it to function as a coupling element within optical microcavities, while its intrinsic photoresponse properties can serve as a benchmark for evaluating optical system performance. SiNMs can also further reduce device footprints, enhance integration, and increase functionality within fabrication processes compatible with photonic devices and systems. Wang et al.[97] formed a heterojunction by integrating SiNM with lead sulfide quantum dots (PbS QDs) and poly(3-hexylthiophene) (P3HT),

 © 2025 Wiley-VCH GmbH

16163028, 2025, 35, Downloaded from https://advanced.onlinelibrary.wiley.com/doi/10.1002/adfm.202502191 by Fudan University, Wiley Online Library on [08/03/2026]. See the Terms and Conditions (https://onlinelibrary.wiley.com/terms-and-conditions) on Wiley Online Library for rules of use; OA articles are governed by the applicable Creative Commons License

16163028, 2025, 35, Downloaded from https://advanced.onlinelibrary.wiley.com/doi/10.1002/adfm.202502191 by Fudan University, Wiley Online Library on [08/03/2026]. See the Terms and Conditions (https://onlinelibrary.wiley.com/terms-and-conditions) on Wiley Online Library for rules of use; OA articles are governed by the applicable Creative Commons License

achieving a broadband optical response from ultraviolet to near-infrared (Figure 9c). In this system, photogenerated electrons and holes are separated within the PbS QDs through the photoelectric effect, where electrons are trapped in the quantum dots while holes are transferred to the SiNM. This process modulates channel conductivity, enabling synaptic behavior under optical stimulation. The synaptic phototransistor not only senses light intensity in real-time but also adjusts short-term and long-term memory effects based on the intensity and frequency of optical stimulation. This allows for integrated sensors, memory, and computation under optical pulses, providing a new pathway for neuromorphic visual systems. Additionally, large-scale device fabrication is crucial for practical applications of SiNM devices (Figure 9d). Yang et al.[69b] developed a membrane reflector surface-emitting laser using transfer-printed SiNM layers and stamp-assisted transfer techniques. In this design, an InGaAs quantum well, serving as the active region of the laser, is sandwiched between two SiNM-based photonic crystal Fano reflectors, significantly reducing the size and thickness of the laser while overcoming the process incompatibilities of epitaxial or bonding methods. By further reducing the lateral cavity size, the pump threshold power at low temperatures was reduced to 8 mW, with a spectral linewidth as narrow as 0.6 nm. A multi-wavelength array can be achieved by controlling the temperature, providing a breakthrough technology for the development of integrated optoelectronic systems. Wei et al.[108] fabricated an embedded InAs/GaAs quantum dot laser directly grown on SOI using MBE, achieving monolithic coupling with silicon photonic waveguides. Based on predefined laser grooves and waveguide designs, the optical mode was directly coupled without additional components, with a coupling efficiency of −6.7 dB. Their application with the InAs/GaAs quantum dot laser demonstrates the integration potential of SiNM in chip-level optical interconnects, high-speed communications, and optical sensing. With the advancement of silicon photonics, the next important direction for SiNM photodetectors should focus on high-mobility, highly chemically stable microfabrication processes. Techniques based on Ge sacrificial layers or SiGeOI are expected to enable the integration of optical neural network systems, achieving post-processing and storage that match the frequencies of photonic systems.

4. SiNMs for Sensors

The ultra-thin characteristics of SiNMs enable them to overcome the limitations of bulk silicon and planar devices in the field of material sensing. In this domain, SiNMs are primarily applied through two pathways: 1) Morphology or resistance changes due to external stress or interaction with external substances.[26,109] These changes primarily originate from the conduction pathways within the SiNM, alterations in interfacial properties, and strain-induced modulation of the energy band structure. 2) Serving as a readout layer to receive feedback from functional materials placed above.[110] In this approach, SiNM can function by detecting changes in the resistance of functional materials or serve as a light readout layer, responding to modulation in the transmittance of the material. In addition, the sensitivity of SiNM interface allows target substances to adjust the barrier height at the interface, significantly affecting the electrical performance of the device and further enhancing sensor sensitivity.

4.1. SiNM Liquid Sensors

Since the components detected in liquids are relatively stable, the primary design approach is to develop liquid sensors based on SiNMs that are sensitive to potential or resistance changes. Chen et al.[111] utilized a notch-assisted transfer technique to generate multifunctional nanocracks in SiNMs. By employing photolithography and reactive ion etching, micro-patterns were fabricated on silicon wafers, and nanocracks were formed after transfer and subsequent stretching. A 30-nm-thick gold layer was deposited on the nanocracks to serve as a SERS substrate, which, in combination with a humidity-sensitive liquid bridge, enabled the detection of resistance changes. This approach achieved a current ratio of 10^4 and a rapid detection time of just 10 seconds (**Figure 10a–c**). Chen et al.[112] proposed a waterproof flexible FET fabricated using a single-crystalline SiNM encapsulation layer. This encapsulation, formed at high temperatures, creates a high-density, low-defect waterproof structure, enabling the FET to operate continuously and maintain stable performance in biological fluid environments. After 16 days in a 37 °C PBS solution, the encapsulation layer thickness was reduced by only 1%. The device utilizes Al_2O_3 as a sensing layer combined with Si FET. When detecting pH in a solution, the reaction of H^+ ions in the solution with the surface of the sensing layer causes a change in the surface potential, leading to a shift in gate-source voltage, which in turn modulates the conductivity of the semiconductor channel (Figure 10e). This device achieved high-sensitivity pH detection (≈58.5 mV pH^{-1}) and maintained excellent electrical performance even after 1200 bending cycles, providing an innovative strategy and integrated system for analytical chemistry as well as applications in the food and medical fields (Figure 10f). Dong and colleagues[113] fabricated a field-effect transistor by combining single-crystal silicon with thermally grown SiO_2 NMs, creating a material system that enables high-performance electronic signal transmission and a stable biofluid barrier structure (Figure 10g). The device, when paired with ion-selective membranes as gate electrodes, can detect corresponding biomarkers, providing a new device design for disease diagnosis and neural engineering (Figure 10h). Teng et al.[114] constructed silicon nanocones using the MACE method, with controllable height and surface properties. The relative standard deviation (RSD) of signal intensity point-to-point and between substrates was below 12.6%, and the detection limit reached as low as 1 fmol, enabling broad applications in fields such as clinical diagnosis, drug analysis, and environmental monitoring. In the future, microfluidics or optical liquid monitoring will become important development directions. SiNM-based electrical signal conversion ports can offer low-loss solutions for next-generation sensors (Figure 10i).

4.2. SiNM Gas Sensors

Gas sensing typically demands high performance in terms of detection time and limit of detection. Therefore, SiNM can provide a high specific surface area or offer sensitive interfacial

© 2025 Wiley-VCH GmbH

16163028, 2025, 35, Downloaded from https://advanced.onlinelibrary.wiley.com/doi/10.1002/adfm.202502191 by Fudan University, Wiley Online Library on [08/03/2026]. See the Terms and Conditions (https://onlinelibrary.wiley.com/terms-and-conditions) on Wiley Online Library for rules of use; OA articles are governed by the applicable Creative Commons License

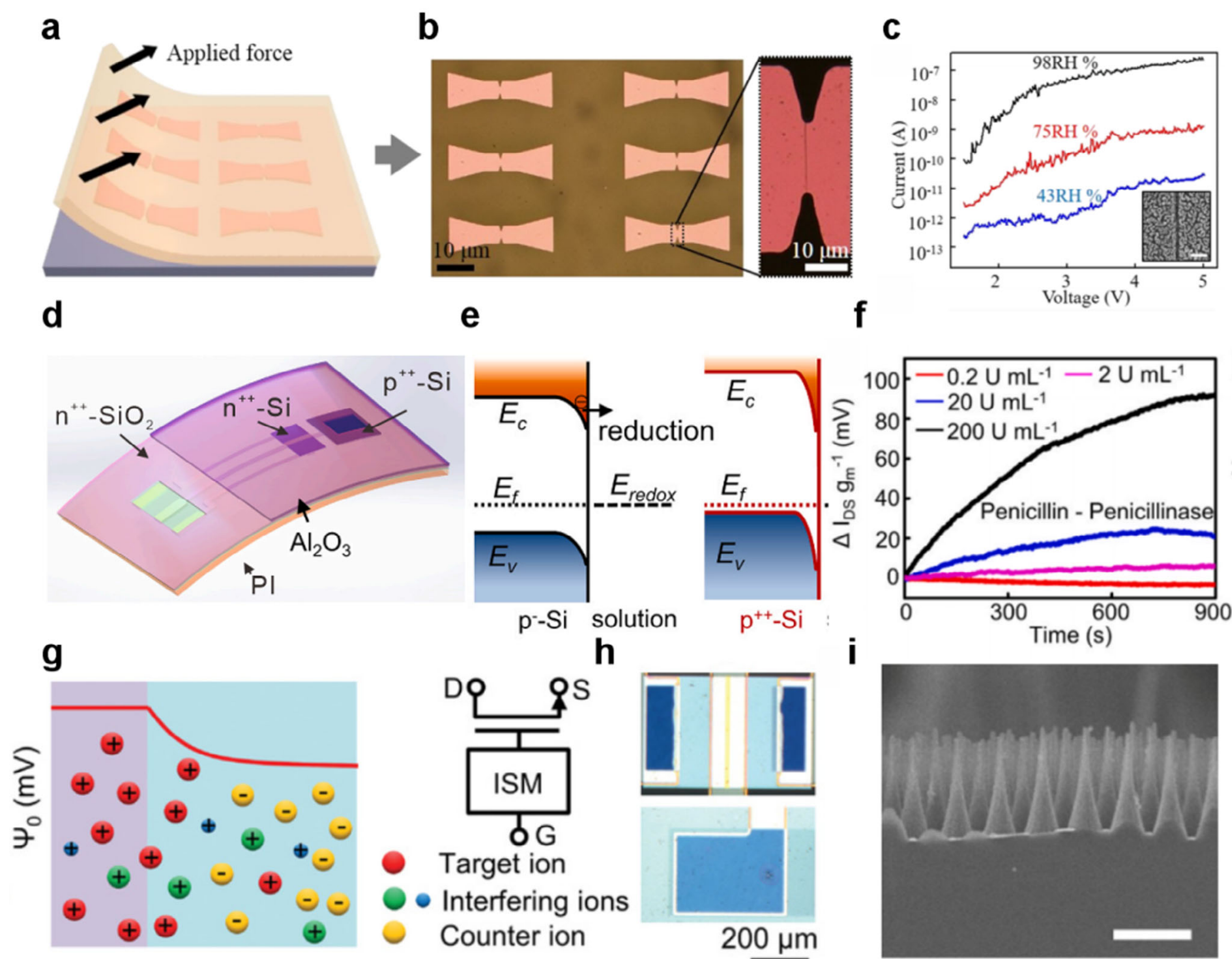

Figure 10. Liquid sensors based on SiNMs. a) Schematic of transferred SiNM nanocrack sensors. b) Optical images of SiNM nanocrack sensors. c) *I–V* relationship of humidity sensing in different relative humidity. Reproduced with permission.[111] Copyright 2018, American Chemical Society. d) Device structure of waterproof SiNM PH sensors. e) Schematic of the energy band of the interface between the solution and p-SiNM. f) Time response of SiNM PH sensor in penicillin-penicillinase reaction with different enzyme concentrations. Reproduced with permission.[112] Copyright 2022, Elsevier. g) Schematic of the potential of the ion-selective membrane (ISM). h) Optical image of SiNM/ISM MOSFET. Reproduced with permission.[113] Copyright 2022, Wiley-VCH. i) SEM image of Si nanocone arrays. Reproduced with permission.[114] Copyright 2018, Elsevier.

responses for high specific surface area functional materials, enabling efficient gas detection. Cho et al.[65a] optimized hydrogen sensing using SiNMs by developing SiNM transistors functionalized with Pd nanoparticles. The sensor, featuring a bottom-gate structure, exhibits rapid response and recovery, as well as enhanced sensitivity. The responses to hydrogen concentrations of 0.1%, 0.3%, 0.5%, and 0.7% was 38%, 98%, 169%, and 250%, respectively, under a gate bias of 0.3 V (**Figure 11a,b**). Li et al.[26] developed a SiNM phototransistor with multifunctional sensing applications in smart digital dust (Figure 11c,d). This sensor integrates photodetection (with an on-off ratio greater than 10^6 and a response time of ≈100 μs), hydrogen detection (with a detection limit as low as 0.05%), and humidity detection (ranging from 43% to 97% RH). It also enables dual-channel sensing and multimodal sensing capabilities. Furthermore, the process is compatible with large-scale wafer-level manufacturing, demonstrating the simplicity and efficiency of SiNM sensor fabrication, thereby providing new insights and technological support for the development of next-generation smart electronic devices. Ko et al.[65b] introduced a NO_x (NO and NO_2) gas sensing system using phosphorus-doped SiNMs and magnesium electrodes. The interaction between NO_x gases and the n-type semiconductor sensor surface induces changes in the surface depletion layer of sensor, with a detection limit of ≈20 ppb. The device showed a response to NO and NO_2 that was 100 times higher than for other substances and exhibited stable electrical performance during multiple bending (with a bending radius of 3 mm) and stretching (up to 40% strain) tests. The silicon and magnesium-based device system is fully degradable under physiological conditions without producing harmful substances, making it suitable for medical implants and environmental monitoring (Figure 11e). Shin et al.[116] combined SiNMs with matrix-assisted laser

 © 2025 Wiley-VCH GmbH

16163028, 2025, 35, Downloaded from https://advanced.onlinelibrary.wiley.com/doi/10.1002/adfm.202502191 by Fudan University, Wiley Online Library on [08/03/2026]. See the Terms and Conditions (https://onlinelibrary.wiley.com/terms-and-conditions) on Wiley Online Library for rules of use; OA articles are governed by the applicable Creative Commons License

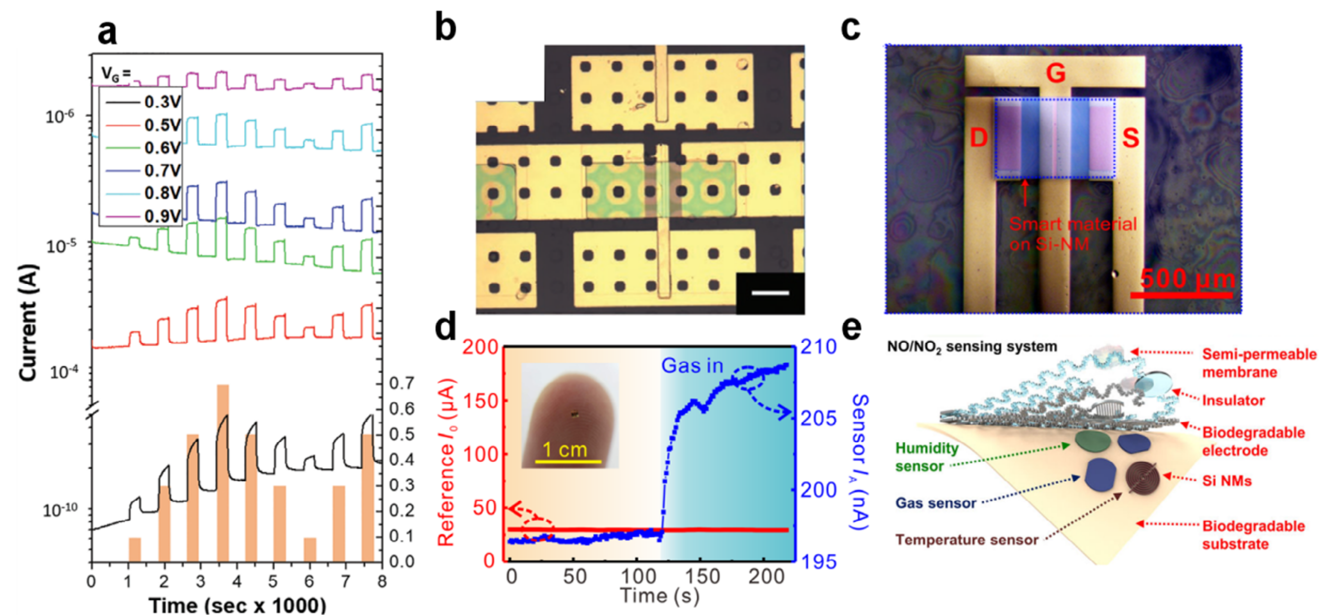

Figure 11. Gaseous sensors based on SiNMs. a) Relationship between sensing current and concentration of hydrogen in a SiNM sensor. b) Optical image of Pd-doped SiNM hydrogen sensors. Reproduced with permission.[65a] Copyright 2021, Wiley-VCH. c) Optical image of a SiNM FET multifunctional sensor. d) Current-time curves of a SiNM sensor and reference sensor for hydrogen sensing. Reproduced with permission.[115] Copyright 2020, AAAS. e) Device structure of serpent SiNM NO_x sensing system. Reproduced with permission.[65b] Copyright 2020, Springer Nature.

desorption/ionization time-of-flight mass spectrometry (MALDI-TOF-MS), enabling efficient detection of high-mass proteins ranging from 0.001 to 2 MDa. The SiNM facilitated ion collisions that emitted electrons, resulting in excellent detection efficiency. Xiao et al.[117] proposed a Schottky barrier field-effect transistor activated by gold source-drain electrodes, which utilizes the catalytic reaction between gold and NH_3 molecules. When NH_3 is adsorbed onto the Au electrode surface, it is catalyzed into NH_3^+ ions and electrons. The electrons migrate to the Au/Si interface, significantly lowering the Schottky barrier height. This sensor can detect NH_3 concentrations as low as 120 ppb at room temperature, demonstrating exceptional selectivity for other gases, and can quickly restore its state within 200 s by applying a reverse bias voltage. Guo et al.[118] proposed a suspended SiNM structure for CO_2 gas sensing using a micro-ring resonator. In this resonator, over 80% of the waveguide mode energy was distributed in the air, and Fano resonance was achieved through coupling between TE_0 and TE_1 modes, reaching a Q factor close to 10^6. This design offered a dynamic monitoring range from 0% to 100% concentration, demonstrating the feasibility of SiNM in planar optical components. With advances in low-dimensional material modification and nanostructuring techniques, SiNMs can be custom-developed for target analyte detection through optical coupling, chemical adsorption, and electrical property modulation at interfaces with other materials.

5. SiNMs for Biomedicine

Due to the mechanical properties of biological skin, organs, and tissues, as well as the need for real-time extraction of biological signals, the application of high-stiffness electronic devices in the biomedical field is significantly limited. Meanwhile, the biocompatibility of flexible organic semiconductors in implantable devices has not been fully resolved. As a biocompatible material, SiNM not only exhibits low stiffness, enabling integration with flexible substrates, but also forms buckle structures under compressive strain, which can further enhance force detection sensitivity. The mechanical properties of SiNMs are close to that of the human epidermis, allowing them to conform closely to the skin surface without imposing mechanical constraints on natural movements.[119] For implantable devices, SiNMs with appropriate surface treatments and encapsulation exhibit excellent biocompatibility, allowing long-term contact with human tissue without triggering obvious immune responses. At the nanoscale, they retain the electrical properties of silicon, ensuring stable operation until the end of their designated degradation lifespan. Their excellent biocompatibility enables SiNM devices to adhere tightly to the skin, internal organs, or microbes,[120] facilitating high-fidelity monitoring and precise therapeutic interventions.

5.1. Outplane SiNM Devices

Out-of-plane buckled SiNM systems are highly sensitive to external forces, making them ideal for fluid and strain analysis, which is crucial for monitoring human respiration, movement, and fluid circulation. When fluid flows, the resistance changes in the SiNM, and metal electrodes can dynamically reflect changes in the physiological indicators in the biological system. Kwon et al.[121] proposed a battery-free, wireless implantable device designed for real-time, continuous monitoring of vascular pressure, flow rate, and temperature. This study utilized SiNMs to design various types of strain gauges, incorporating out-of-plane buckled structures, in-plane interdigital structures, and microcantilever

© 2025 Wiley-VCH GmbH

16163028, 2025, 35, Downloaded from https://advanced.onlinelibrary.wiley.com/doi/10.1002/adfm.202502191 by Fudan University, Wiley Online Library on [08/03/2026]. See the Terms and Conditions (https://onlinelibrary.wiley.com/terms-and-conditions) on Wiley Online Library for rules of use; OA articles are governed by the applicable Creative Commons License

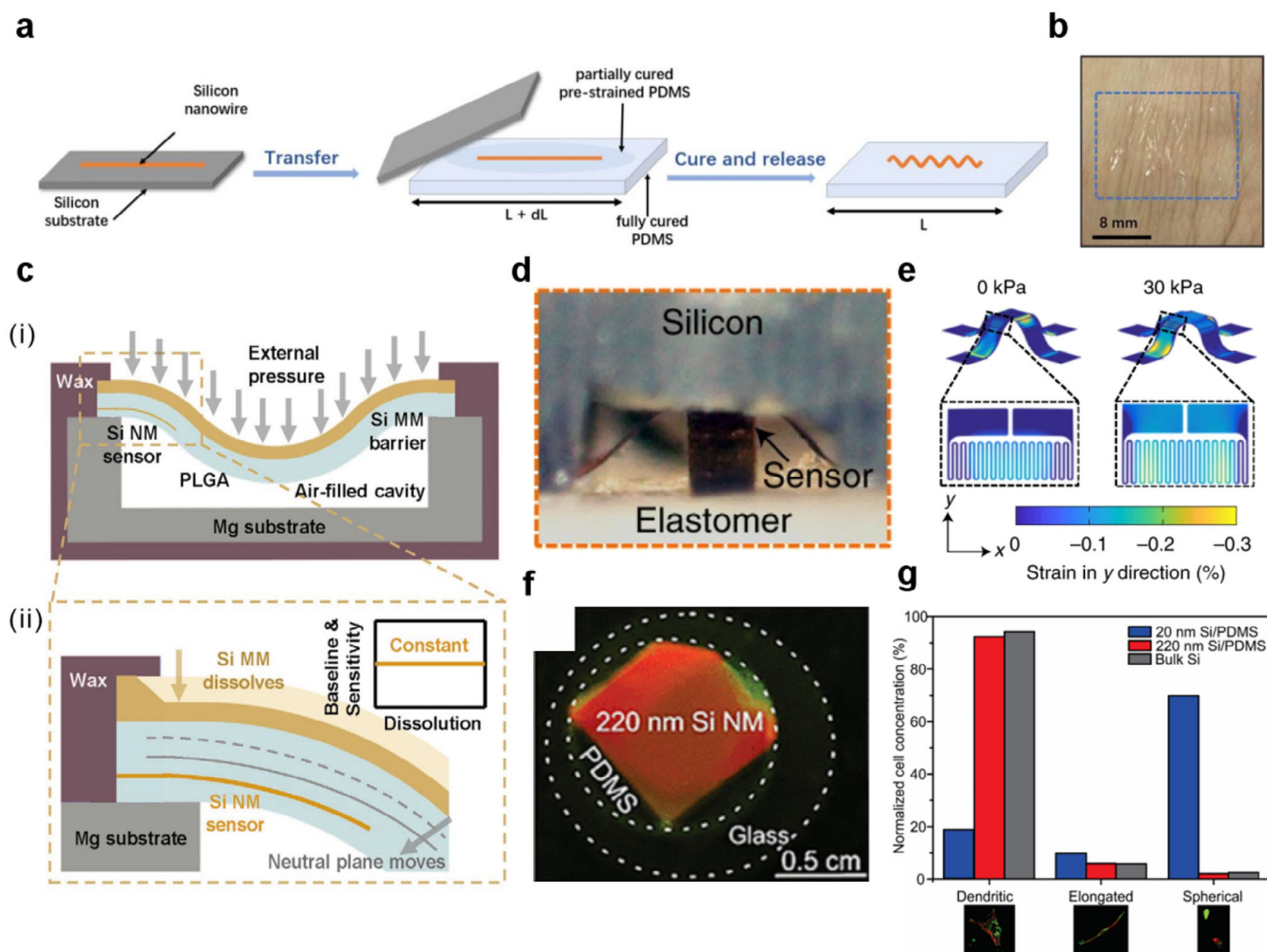

Figure 12. Design and application of SiNM buckled microstructure biomedical devices. a) Fabrication process of stretchable SiNW. b) Photograph of SiNW sensor on human skin. Reproduced with permission.[122] Copyright 2020, American Chemical Society. c) i) Design of SiNM bioresorbable monitoring system, which consists of SiNM and SiMM, Mg substrate, and air-filled microcavity. ii) Dissolution feature of SiNM-SiMM system. Reproduced with permission.[123] Copyright 2020, Wiley-VCH. d) Optical image of SiNM pressure sensor with additional silicon cavity. e) FEM simulation results of SiNM and Au layer of 3D pop-up pressure sensor at 0 kPa and 30 kPa.[10a] Copyright 2020, Springer Nature. f) Optical image of a fabricated SiNM effectively compliant layered substrates. g) Normalized average concentration of dendritic, elongated, and spherical cells on SiNM/PDMS and bulk Si substrates. Reproduced with permission.[124] Copyright 2020, American Chemical Society.

structures to develop sensors for intravascular flow rate, temperature, and blood pressure monitoring. The device demonstrated precision and sensitivity comparable to clinical tools in pig and sheep models, with potential future applications in monitoring the hemodynamic status of post-operative mobile patients. Huang et al.[122] developed an ultra-miniaturized stretchable strain sensor based on a single silicon nanowire (SiNW) for invisible electronic skin applications (**Figure 12**a). They employed a vapor-liquid-solid method assisted by a temperature gradient to fabricate centimeter-long SiNWs, which were then converted into stretchable forms through a pre-strained substrate, achieving up to 50% stretchability and high durability over more than 10 000 cycles (Figure 12b).

The buckle design of SiNM effectively utilizes the deformation caused by the extra length between fixed ends to withstand external forces, enabling cyclic elastic deformation. Yang et al.[123] designed a liquid barrier based on silicon micromembrane (SiMM) encapsulation and a strain sensor composed of SiNM. This sensor demonstrated stable performance over three weeks in a rat model, offering accuracy and reliability comparable to existing clinical-standard devices. Additionally, the encapsulation design allows the material to fully degrade within approximately four weeks in physiological conditions, reducing the need for subsequent handling or removal (Figure 12c). Han et al.[10a] transformed traditional 2D structures into three-dimensional pop-up platforms using compressive buckling techniques (Figure 12d). This platform integrates sensors for temperature, pressure, and electrophysiological signals, along with electrical and thermal actuators, enabling high-density spatiotemporal mapping of biological information. Moreover, it provided therapeutic functions such as programmable electrical stimulation, radiofrequency ablation, and irreversible electroporation (Figure 12e). Bai et al.[125] integrated SiNM-based devices, optical fibers, and multilayer optical filters to develop a photonic device capable of continuously

 © 2025 Wiley-VCH GmbH

16163028, 2025, 35, Downloaded from https://advanced.onlinelibrary.wiley.com/doi/10.1002/adfm.202502191 by Fudan University, Wiley Online Library on [08/03/2026]. See the Terms and Conditions (https://onlinelibrary.wiley.com/terms-and-conditions) on Wiley Online Library for rules of use; OA articles are governed by the applicable Creative Commons License

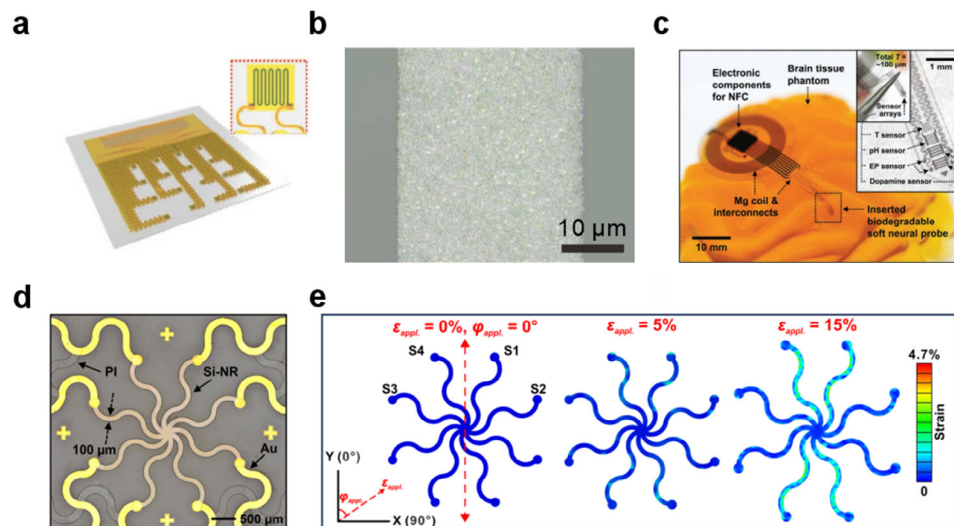

Figure 13. Wearable SiNM transient devices. a) Schematic of encapsulated Au-doped SiNM temperature sensors. b) Optical image of Au-doped SiNM. Reproduced with permission.[20a] Copyright 2021, Wiley-VCH. c) SiNM/2D TMD multifunctional probes on brain models. Reproduced with permission[68] Copyright 2022, Wiley-VCH. d) Optical image of sensing area of SiNM ribbon. e) FEM simulation of strain distribution in SiNM ribbon under 0%, 5%, and 15% of stretching strain along the *Y*-axis. Reproduced with permission[19] Copyright 2024, AAAS.

monitoring physiological parameters such as tissue oxygenation, temperature, and neural activity at specific depths within the body. This technology eliminates the need for secondary surgery associated with traditional electronic implants, making it valuable for neuroscience research, pathological studies of diseases, and postoperative recovery management. Abdul et al.[124] introduced the influence of the mechanical properties of SiNM on flexible substrates on single-cell behavior. Their research found that cells exhibited similar behavior on 220-nm-thick SiNMs as on bulk silicon, while on 20-nm-thick SiNM, there was reduced fibroblast and adhesion plaque activity, regulating cell behavior, highlighting its potential applications in microbiology (Figure 12f,g). In future research, microstructured SiNM devices could also be combined with actuator materials and design concepts, endowing the devices with multifunctional capabilities for both sensing and actuation.

5.2. Structured SiNM Devices

For viscoelastic substrates and surfaces, their mechanical-strain behavior is fundamentally different from that of linear elastic substrates. Large strains caused by external forces do not result in damage to viscoelastic materials, and the nonlinear stress-strain behavior provides more possibilities for optimizing the mechanical performance of SiNM/viscoelastic substrate systems. The combination of serpentine and island structures enables in-time and in-situ tactile and temperature feedback, providing prosthetics with sensory feedback and integration of rigid components.[45a,126] Through mechanically optimized planar designs, SiNMs can sensitively respond to strain states in biological regions without external force, typically measured by resistance changes in metal components. Additionally, component structures that can withstand large deformations ensure that SiNM devices remain attached to the target area during monitoring, preventing detachment. Sang et al.[20a] introduced an ultra-high sensitivity wearable temperature sensor array based on gold-doped SiNMs (**Figure** 13a,b). By controlling the gold doping concentration, the Fermi level and activation energy were adjusted, significantly improving the temperature coefficient of resistance (TCR) to −37 270.72 ppm °C^{-1}, which is ≈20 times higher than that of similar metal-based temperature sensors. The sensor exhibited a resistance change rate of ≈4% with a body surface temperature variation of just 1.5 °C. Additionally, the sensor array could provide high spatial resolution thermal imaging and demonstrate potential for chip- and wafer-level integration. Yang et al.[68] developed a biodegradable wireless neurochemical system combining SiNMs, 2D transition metal dichalcogenides, and nanoparticle systems. The integration of 2D materials provides additional active sites to enhance charge transfer, demonstrating excellent sensitivity and selectivity in electrochemical detection. Based on this system, the SiNM device enables multi-parameter synchronous detection of pH, temperature, and electrophysiological signals (Figure 13c). Kim et al.[113] enhanced silicon nanoribbon electronic skin by incorporating nanowire electrodes to transmit electrical signals, effectively simulating the sensory functions of natural skin. Additionally, these electrode surfaces were coated with cerium dioxide nanoparticles to suppress inflammatory responses.[127] Meng et al.[128] introduced a SiNM temperature-bending strain sensor that achieves decoupling of temperature and strain signals through a fast Fourier transform. Temperature signals are extracted in the frequency range below 1 Hz, while pulse signals are extracted above 1 Hz. Even within a wide temperature fluctuation range of 4 °C, the typical characteristic waves of the pulse can still be clearly detected. Hu and colleagues[19] arranged multiple silicon nanoribbons (Si-NRs) in different orientations to form an octopus-shaped sensor capable of omnidirectional detection of dynamic biomechanical strain on soft tissue surfaces (Figure 13d,e). This device not only monitors physiological signals such as human pulse and

 © 2025 Wiley-VCH GmbH

16163028, 2025, 35, Downloaded from https://advanced.onlinelibrary.wiley.com/doi/10.1002/adfm.202502191 by Fudan University, Wiley Online Library on [08/03/2026]. See the Terms and Conditions (https://onlinelibrary.wiley.com/terms-and-conditions) on Wiley Online Library for rules of use; OA articles are governed by the applicable Creative Commons License

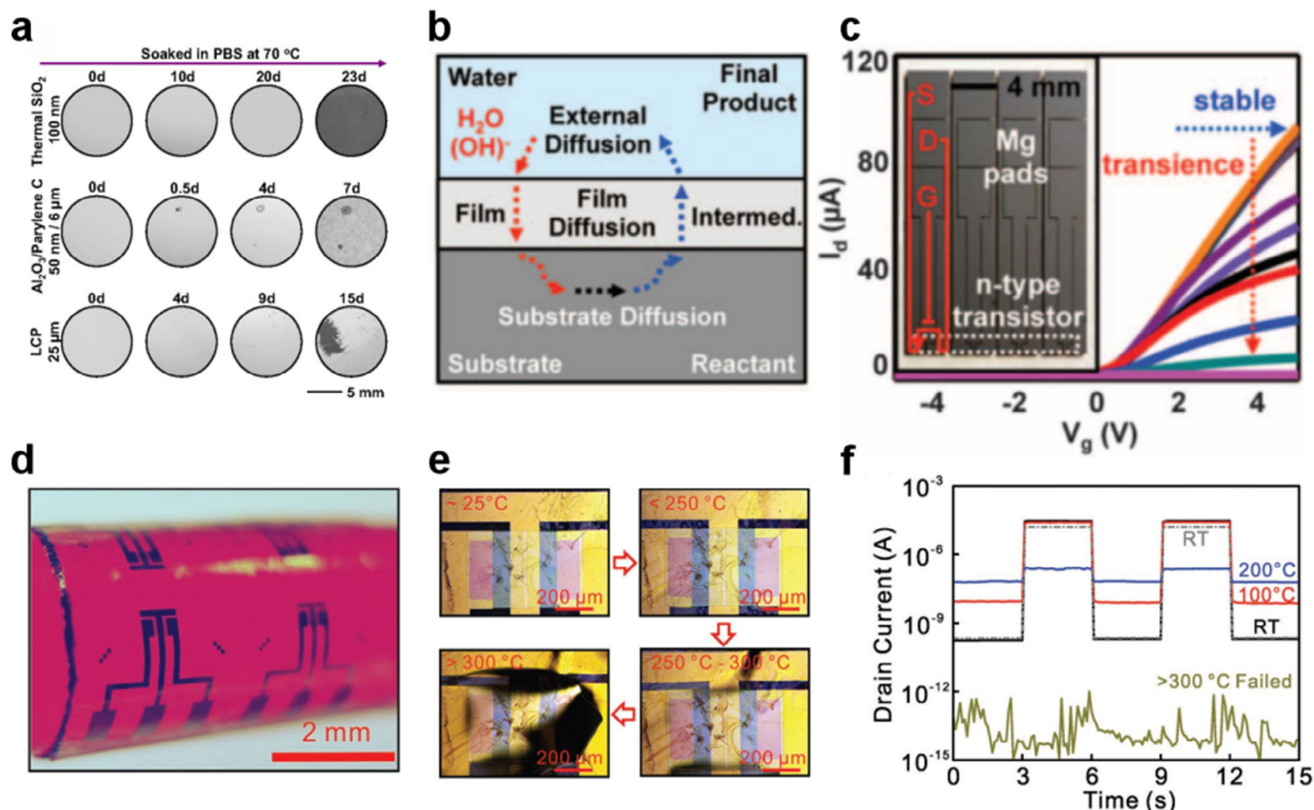

Figure 14. Mechanism and performance of implanted SiNM transient devices. a) Optical images of dissolution process of Mg encapsulated by thermal SiO_2, Al_2O_3/parylene C, and bulk liquid crystal polymer in time order. Reproduced with permission.[131] Copyright 2016, National Academy of Sciences. b) Reaction-diffusion model in transient SiNM devices. c) Design and performance of transient Mg/SiNM transistors.[135] d) Optical image of thermal-triggered SiNM transistor. e) Optical image of transient behavior in the SiNM transistor after heating. f) Transient *I*–*V* behavior of the SiNM transistor. Reproduced with permission.[129b] Copyright 2018, Wiley-VCH.

intraocular pressure but also detects pathological changes like myocardial infarction in animal models, significantly expanding the multifunctional applications of a single device. Currently, planar-structured devices have achieved effective sensing and stretching on attached objects. Future research will focus on adhesion and effective sensing of compressive or shear states on plastic surfaces.

5.3. Transient SiNM Devices

In biomedical applications, the stability duration of implanted devices in the body is not always preferable to be as long as possible. Aligning the lifespan of the device with the wound healing and inflammation recovery cycle can help reduce potential negative impacts on the body.[129] Benefit to the characteristic of silicon to undergo slow degradation in biological fluids, careful control of SiNM thickness and external encapsulation can allow the device to complete its monitoring tasks without requiring surgical retrieval. Consequently, transient SiNM devices have been proposed to create controllable, self-degrading biomedical devices.[130] Fang et al.[131] investigated the hydrolysis kinetics of single-crystalline SiNMs in biological fluids and various aqueous solutions, evaluating their dissolution behavior under different pH levels, ion concentrations, and temperatures, providing a design paradigm for transient SiNM devices (**Figure 14a**). Understanding and researching the degradation behavior of transient devices will greatly contribute to the controllable design of device performance and lifespan.[132] Subsequently, Hwang et al.[129c] utilized transfer printing, PVD, and solution casting techniques to combine single-crystalline SiNMs, magnesium (Mg) conductors, magnesium oxide (MgO) insulating layers, and silk substrates to fabricate implantable transient MOSFETs (Figure 14c,d). These devices maintained normal operation for at least 90 h in deionized water and fully dissolved within ≈3 weeks, producing harmless by-products, demonstrating the effectiveness of this technology for sterilization at surgical sites. Shin et al.[133] developed a bioresorbable pressure sensor for monitoring chronic diseases and healing processes. They employed thermally grown silicon dioxide (t-SiO_2) as a barrier against biological fluids and used amorphous silicon dioxide formed through the pyrolysis of PDMS as an adhesive layer. The sensor was fabricated by bonding a pair of SOI wafers, which extended the lifespan of the thermal oxide isolation layer to about a month. In in-vivo experiments with rats, the sensor was able to stably and accurately monitor intracranial pressure for up to 25 days, with performance comparable to non-bioresorbable clinical standard devices, providing a versatile platform for a wide range

© 2025 Wiley-VCH GmbH

of bioresorbable electronic devices. Kang et al.[43a] fabricated a bioresorbable pressure sensor with a membrane composed of poly(lactic-co-glycolic acid) (PLGA) with a thickness of 30 μm, supported by a nanoporous silicon or magnesium foil substrate with a thickness of 60–80 μm. The external miniaturized wireless potentiometer allows real-time and accurate data transmission from the sensor, although mobility is somewhat restricted. Additionally, SiNM transient devices hold potential value in information security and early warning systems for extreme conditions. Li et al.[129b] constructed a flexible transient phototransistor using SiNM, incorporating thermally degradable poly(α-methylstyrene) (PAMS) as a transient layer to achieve thermally triggered device failure. At ≈300 °C, the PAMS layer fully depolymerizes into volatile products within 5 minutes, leading to the structural breakdown of the phototransistor (Figure 14d–f). The ultrathin nature of SiNMs facilitates permanent device failure once trigger conditions are met, ensuring the security of sensitive data. Currently, transient SiNM devices still have two major directions for development: 1) When the expected lifespan of the device changes, it is necessary to explore whether SiNM degradation can be slowed down through non-contact methods. 2) For existing fast data transmission, the failure of transient devices needs to reach the millisecond level to meet the requirements for data security. The development of SiNM transient devices could incorporate additional functional materials in the future to enable rapid degradation triggered by specific conditions, or to serve as warning modules for transient device failure.[134]

5.4. Composited SiNM Devices

Benefiting the excellent chemical stability of SiNM, when integrated into composite systems with low-dimensional materials such as nanoparticles or nanowires, it can rapidly read or inject the electrical signals of the modified materials without undergoing chemical reactions at the interface. This ensures the stable operation of low-dimensional materials in wearable and implantable devices.[136] Composite material systems, centered on SiNM devices as a platform, can achieve breakthroughs in performance and functionality, enabling customizable and specialized detection tailored to specific biomedical needs.

Kim et al.[138] used direct printing of liquid metals to integrate Ag NM-nanowire antennas with SiNMs and flexible substrates, creating stretchable interconnect structures in contact lenses while meeting wireless communication needs. By embedding mechanical reinforcement rings in flexible regions to concentrate strain, they significantly enhanced the sensitivity of contact lenses. Tests on rabbits and 10 human participants demonstrated that the contact lens could safely and accurately provide quantitative intraocular pressure. The strain sensor accurately detected slight corneal deformations due to changes in IOP (≈0.03% per mmHg). Kim et al.[137] developed a floating-gate memory system based on gold nanoparticles, which were uniformly assembled on a large-area silicon platform using the Langmuir–Blodgett (LB) method. This design improves charge capture efficiency and long-term data retention in memory devices. Atomic force microscopy techniques were employed to inject and read charges into the nanocrystal floating gate (**Figure 15a**). The nanocrystalline monolayer assembled by the LB method exhibited high uniformity, and consistency was confirmed in a 22×22 memory array, providing a pathway for the realization of large-area multiplexed wearable SiNM electronic devices (Figure 15b). Kim et al.[110a] designed a flexible, transient electrochemical dopamine sensor based on bioresorbable SiNMs and iron-catalyst nanoparticles (Figure 15c). The sensor was composed of heavily doped SiNMs (≈300 nm thick) coated with iron-decorated carboxylated polypyrrole nanoparticles (Fe^{3+}-CPPy NPs) as the active sensing element. The Fe^{3+}-CPPy NPs could detect dopamine concentrations at picomolar levels, with performance comparable to platinum-based catalysts, and they fully dissolved within a few hours under physiological conditions, meeting biocompatibility requirements (Figure 15d,e). Son et al.[139] developed a system for controlling drug release through thermal stimulation. Gold nanoparticles (Au NPs) and TiO_2 layers in resistive random-access memory (RRAM) served as electron traps and resistive switches, respectively. The RRAM array was integrated with SiNM strain sensors and resistive heaters to precisely monitor tremor frequencies and adjust drug diffusion rates through temperature control, offering the potential for monitoring neurological diseases such as Parkinson's disease. Leveraging the thermoelectric, piezoelectric, and optoelectronic properties of low-dimensional materials, SiNM-based wearable and implantable devices could provide additional wireless power solutions, reducing reliance on external power sources. Nanomaterial-based drugs with medical applications could also be integrated onto the device surface, enabling in situ drug release and monitoring.[120a]

6. SiNMs for Energy Harvesting

In the field of energy harvesting, the low stiffness of SiNM can make contributions at both macroscopic and microscopic levels. In photovoltaic devices, their ultra-thin flexibility and excellent biocompatibility make them crucial for portable and implantable devices. In energy storage, the SiNMs can mitigate the volume changes and instability of the solid electrolyte interface that occur during ion insertion and extraction in batteries, thus preventing performance degradation caused by electrode material fracturing.[140]

6.1. Structured SiNMs for Energy Harvesting

The charge–discharge cycling process in ion batteries imposes high demands on the structural stability, interfacial layer behavior, and activity of the electrode. The primary challenge preventing the application of silicon as a high-capacity anode material arises from stress concentration and lattice defect issues in brittle silicon during volumetric expansion and contraction. In freestanding SiNM, the insertion and extraction of ions can be alleviated by deformation, making it possible to achieve low-damage and long-lifespan silicon battery electrodes. Additionally, the increased specific surface area contributes to higher capacity and energy density, further improving battery performance. Guo et al.[35] investigated a mechanical model based on plate theory to determine the critical conditions for different 2D geometries in surface tension and elastic film self-folding. Using capillary force-driven self-assembly, they placed silicon foils with specific geometries, thicknesses, and sizes on a hydrophobic surface,

 © 2025 Wiley-VCH GmbH

16163028, 2025, 35, Downloaded from https://advanced.onlinelibrary.wiley.com/doi/10.1002/adfm.202502191 by Fudan University, Wiley Online Library on [08/03/2026]. See the Terms and Conditions (https://onlinelibrary.wiley.com/terms-and-conditions) on Wiley Online Library for rules of use; OA articles are governed by the applicable Creative Commons License

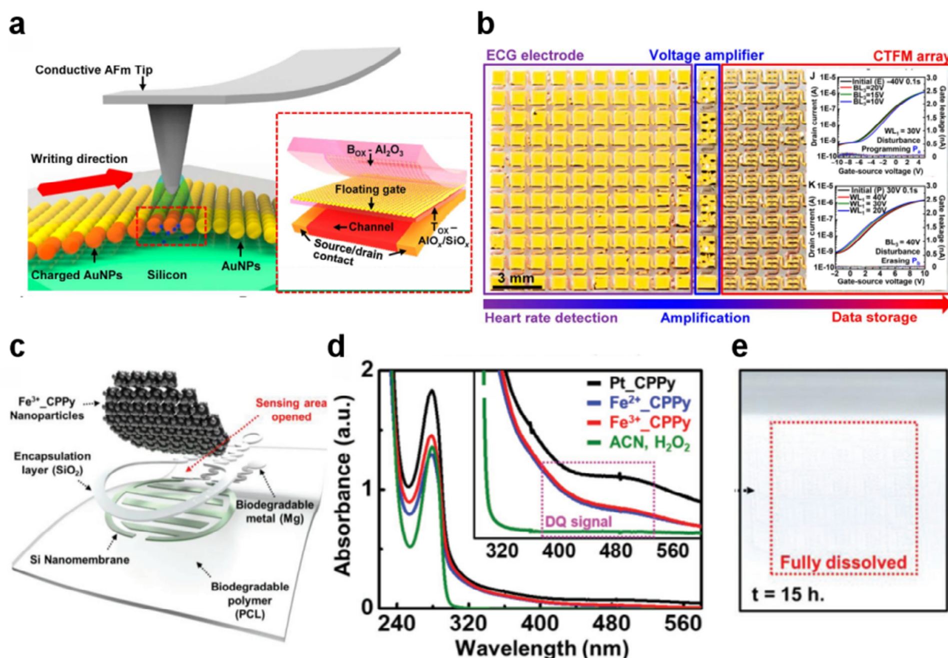

Figure 15. Biomedical devices based on SiNM/low-dimensional material systems. a) Diagram of charge injection of AuNPs on SiNM via AFM tips (inset device structure of a single charge trap floating gate memory unit). b) Optical image of a wearable charge trap floating gate memory array. Reproduced with permission.[137] Copyright 2016, AAAS. c) Exploded view of SiNM/Fe^{3+}-CPPy NPs neurotransmitter detector. d) UV–vis spectra of productions of dopamine-o-quinone with various catalysts. e) Optical image of SiNM/Fe^{3+}-CPPy NPs neurotransmitter detector dissolved after immersing in PBS(≈pH 11, 37 °C) for 15 h. Reproduced with permission.[110a] Copyright 2018, Wiley-VCH.

with a water droplet positioned at the center of the foil. As the water droplet evaporated, the capillary forces caused the SiNM to fold around the droplet into a predetermined 3D shape, successfully achieving the transition of monocrystalline SiNMs from 2D to 3D structures (**Figure 16a**). Further processing led to the creation of 3D photovoltaic devices made of thin single-crystalline SiNM foils (Figure 16b). This 3D architecture demonstrated advantages in light trapping and reduced reflection losses, resulting in 187% increase in energy conversion efficiency compared to planar devices, providing new insights and technological support for developing low-cost, high-efficiency photovoltaic devices in the future (Figure 16c). In energy storage, Huang et al.[36] studied the performance of rolled amorphous SiNMs (a-SiNMs) as anode materials for sodium-ion batteries. They aimed to address the challenges posed by the large sodium ion radius, which causes volume changes and slow Na^+ transport during sodiation/desodiation, leading to low capacity and poor cycling stability (Figure 16d). The rolled a-Si structure provided sufficient space to accommodate volume expansion, enhancing the mechanical stability of the anodes (Figure 16e). Electrochemical testing showed that a-SiNM achieved an initial discharge capacity of 661.1 mAh g^{-1} and an initial charge capacity of 283.4 mAh g^{-1} at a current density of 100 mA g^{-1}. After 50 cycles, the a-SiNM maintained a reversible capacity of 255 mAh g^{-1}. The sodium storage process of a-SiNM was primarily controlled by surface capacitive behavior, facilitating fast charge–discharge cycles and long cycle life, demonstrating potential in high-performance, low-cost sodium-ion batteries. Silicon is an ideal candidate for lithium-ion battery anodes due to its highest theoretical specific capacity (4200 mAh g^{-1}). However, the volume change during lithium-ion insertion and extraction (up to 400%) leads to electrode pulverization, loss of electrical contact, and rapid capacity decay. Huang et al.[142] utilized PVD and strain-release rolling techniques to fabricate TiO_x/Si/TiO_x NMs. The conductivity and amorphous structure of the TiO_x layer further enhance the electrochemical performance and structural stability of the anode material (Figure 16f). Both the TiO_x and Si layers were amorphous, with the TiO_x layer containing Ti^{3+} and oxygen vacancies that facilitated Li^+ and electron transport. The 3D TiO_x/Si/TiO_x NMs, due to their large surface area and low-stiffness structure, exhibited high mechanical tolerance and high loading density. When paired with a commercial cathode to assemble a complete lithium-ion battery, the TiO_x/Si/TiO_x NM anode demonstrated high energy density (525 Wh kg^{-1}) and excellent cycling stability, retaining 92% of its capacity after 50 cycles (Figure 16g). Thus, flexible SiNM batteries will greatly enhance the energy storage and functionality of implantable devices, providing convenience for their operation. Currently, SiNM battery electrodes are still arranged in a disordered and loose manner. In the future, the ordered arrangement and encapsulation of SiNM microstructured electrodes could provide more direct and shorter ion and electron transport pathways. Meanwhile, the ordered current distribution would reduce the formation of local hotspots or "dead zones," thereby improving electrode utilization and extending cycle life.

For buckled or strain-free SiNMs, their flexibility makes them particularly suitable for integration with flexible energy storage

© 2025 Wiley-VCH GmbH

16163028, 2025, 35, Downloaded from https://onlinelibrary.wiley.com/doi/10.1002/adfm.202502191 by Fudan University, Wiley Online Library on [08/03/2026]. See the Terms and Conditions (https://onlinelibrary.wiley.com/terms-and-conditions) on Wiley Online Library for rules of use; OA articles are governed by the applicable Creative Commons License

16163028, 2025, 35, Downloaded from https://advanced.onlinelibrary.wiley.com/doi/10.1002/adfm.202502191 by Fudan University, Wiley Online Library on [08/03/2026]. See the Terms and Conditions (https://onlinelibrary.wiley.com/terms-and-conditions) on Wiley Online Library for rules of use; OA articles are governed by the applicable Creative Commons License

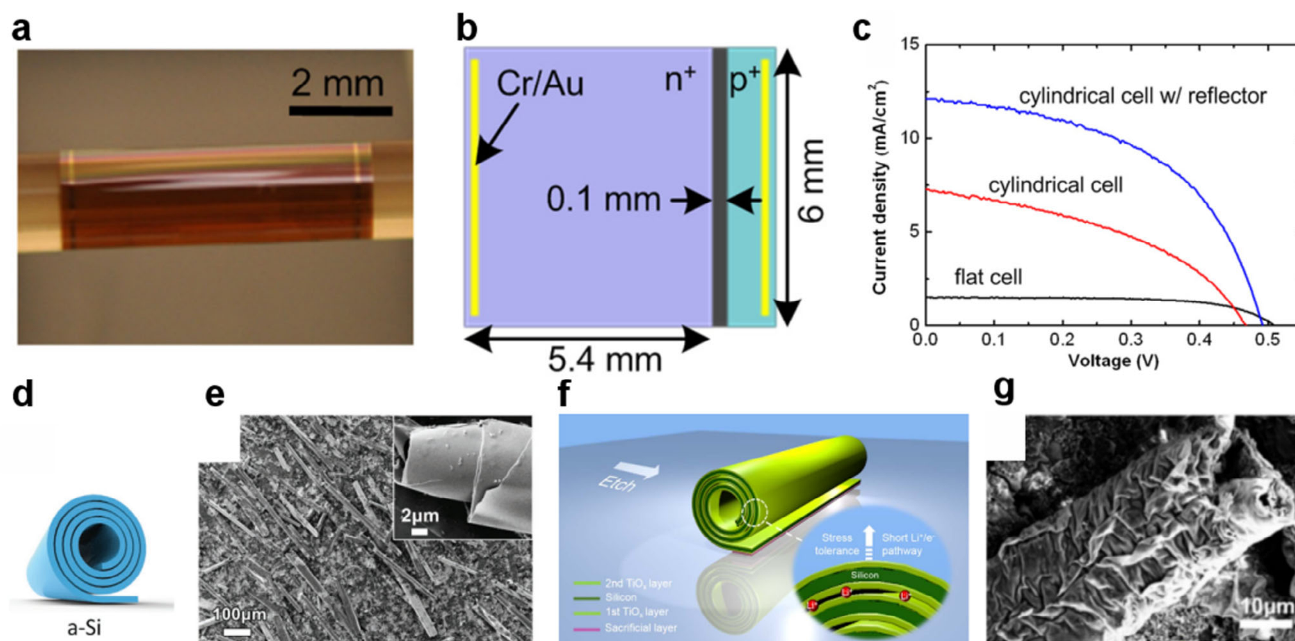

Figure 16. Energy storage principle and electrochemical performance of self-rolling SiNMs. a) Optical image of the cylindrical rolled-up SiNM cell on a cylindrical lens. b) Design of rolled-up SiNM solar cell. c) *I–V* relationship between flat SiNM, rolled-up SiNM, and rolled-up SiNM with reflector. Reproduced with permission.[35] Copyright 2009, National Academy of Sciences. d) Illustration and e) SEM image of a-SiNM electrode. Reproduced with permission.[36] Copyright 2018, Wiley-VCH. f) Schematic of rolled-up $TiO_x/Si/TiO_x$ NM structure for lithium storage. g) SEM image of $TiO_x/Si/TiO_x$ NM. Reproduced with permission.[141] Copyright 2018, Elsevier.

components in devices.[145] Yu et al.[143] investigated the use of flexible elastic substrates to relieve stress in lithium-ion battery silicon anode materials. On a PDMS substrate, the stress generated by SiNM during charge and discharge cycles is released through its buckled form, preventing electrode fragmentation and failure (**Figure 17a**). The half-cells assembled with SiNMs on flexible substrates maintained 85% of their capacity after 500 cycles, exhibiting an extremely low-capacity decay rate (0.033% per cycle), which is significantly better than traditional silicon electrodes (Figure 17b–d). Lu et al.[144] explored the feasibility of using biodegradable monocrystalline silicon photovoltaic microcells as a power source for temporary biomedical implants. They proposed a fully degradable photovoltaic platform based on monocrystalline silicon microcells, designed to operate LEDs at wavelengths with deep tissue penetration (red and near-infrared light). When placed under 4 mm thick pig skin and fat, the near-infrared light generated 64 μW of power with a V_{oc} of 4.25 V. In vivo experiments showed that a blue LED implanted subcutaneously in rats functioned normally for 3 days, and the photovoltaic system completely degraded after 4 months without causing an inflammatory response, making it a reliable option for powering biomedical implants (Figure 17e). High-specific surface area structures are an important technique for enhancing light absorption and improving the performance of photovoltaic devices. However, the dry etching process used in deep silicon etching has stringent processing requirements, and the slow etching of sidewalls cannot be ignored. Lin et al.[73a] utilized a dual-layer Ag/Au catalyst to prepare high-quality silicon micropillar arrays based on MACE. By controlling the thickness of the metal catalyst, they effectively regulated the structural uniformity and flatness of the micropillars ranging from the nanoscale to the microscale (Figure 17f,g). The high specific surface area of the silicon micropillar arrays significantly reduced the surface reflectance (≈11%), enabling more efficient capture of incident light compared to planar structures with reflectance exceeding 30%. After surface passivation, the performance of solar cells is comparable to that of planar silicon wafers, achieving a carrier lifetime of 220 μs and a cell efficiency of 14.6%. This design also shows potential for applications in photoelectrochemical cells and other related fields.

6.2. Flexible SiNMs Solar Cells

Since Si-based solar cells and photovoltaic devices currently play an important role in the photovoltaic industry, the flexibility of SiNMs can extend their application boundaries to implantable and portable devices. Compared to commonly used amorphous or polycrystalline Si flexible solar cells, SiNM solar cells enable the integration of single-crystal silicon into flexible energy harvesting systems. Building on existing flexible designs, they leverage the high crystalline quality of single-crystal silicon to further enhance photoelectric conversion efficiency.

As flexible processes and transfer techniques continue to mature, research on SiNM-based flexible solar cells needs to shift towards scalability and applicability of their photoelectric conversion performance. Therefore, maintaining flexibility and good crystal quality while using thicker SiNMs to enhance absorption is an important research direction. Lee et al.[67] proposed a highly integrable material platform by engineering photonic

 © 2025 Wiley-VCH GmbH

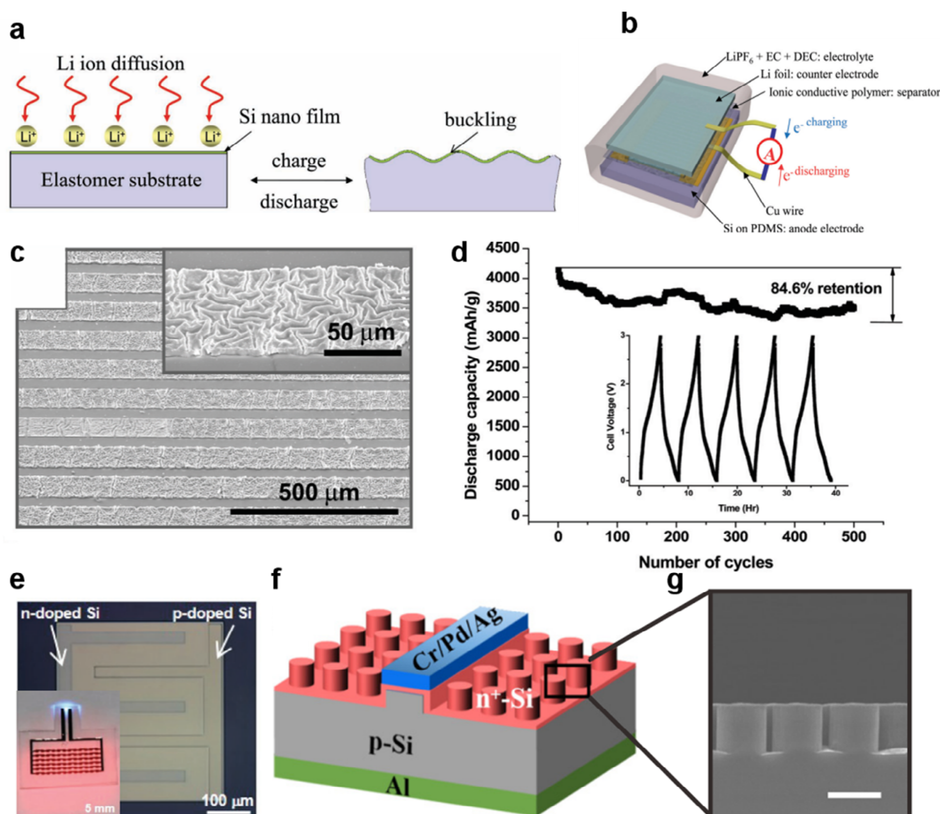

Figure 17. Charging and discharging principle and electrochemical performance of planar SiNM array. a) Schematic diagram of lithiation in SiNM/elastomer substrate system. b) Assembly of SiNM-based battery cell. c) SEM image of SiNM after lithiation. d) Long-term cycling stability of SiNM anode. Reproduced with permission.[143] Copyright 2012, Wiley-VCH. e) Optical image of biodegradable crystalline SiNM cells (inset: SiNM cell arrays for the operation of a bioresorbable LED). Reproduced with permission.[144] Copyright 2018, Wiley-VCH. f) Structure illustration of Si micropillar solar cell. g) SEM image of n-Si micropillar. Reproduced with permission.[73a] Copyright 2019, American Chemical Society.

nanostructures to directly fabricate ultrathin silicon solar microcells from the silicon wafer, which is compatible with large-scale assembly processes and reduces material costs (**Figure 18a**). With the optimized design of antireflective coatings and back reflectors, the printed ultrathin (≈8 μm) nanostructured silicon solar cells achieved a solar-to-electric conversion efficiency of 12.4%, demonstrating the potential for flexible silicon solar cells through optimized device and material design (Figure 18b,c). Lee and colleagues[60] proposed a method for generating ultra-thin SiNMs through multiple patterning and etching processes on bulk silicon. This approach utilizes photolithography to define interlocking and anchoring connections between microstrips, creating high-fill-factor SiNMs (Figure 18d). By controlling the etching depth, the thickness of the SiNM can be adjusted from 300 nm to 13 μm (Figure 18e). The interlocking SiNM can be used to fabricate centimeter-scale flexible solar cells, achieving a 7.9% conversion efficiency, and enabling low-cost, reproducible production of SiNM solar cells (Figure 18f). Liu and colleagues[16,42b] proposed a strategy to improve the flexibility of silicon wafers through edge passivation treatment, overcoming the brittleness limitation of traditional monocrystalline silicon wafers for large-scale applications. After HF_3 treatment, the maximum stress during bending was significantly reduced, lowering the risk of fracture (Figure 18g,h). Their wafer-scale (15.6×15.6 cm^2) flexible solar cells based on passivated silicon exhibited minimal performance loss under extreme temperature cycles from −70 to 85 °C, with a photoelectric conversion efficiency of 24.5%, far exceeding that of other commercial flexible solar cell materials, thus achieving high-performance, low-cost SiNM solar cells for commercial applications (Figure 18i–k). In the future, SiNM solar cells are expected to combine with organic, perovskite, and other material systems, advancing toward large-area, flexible tandem solar cells within composite material systems.[146]

7. SiNM in ICs

With the continuous increase in demands for computational speed and application scenarios of ICs, the traditional scaling approach for semiconductor devices has reached its bottleneck. Consequently, methods for achieving higher integration density of transistors and ICs in flexible technologies and heterogeneous integration have garnered attention.[17a,43b,147] By integrating SiNM devices at the chip and IC levels, it is possible to combine functions such as sensing, computation, and storage in a compact package, elevating the application potential and scope of SiNMs to new heights.

© 2025 Wiley-VCH GmbH
16163028, 2025, 35, Downloaded from https://advanced.onlinelibrary.wiley.com/doi/10.1002/adfm.202502191 by Fudan University, Wiley Online Library on [08/03/2026]. See the Terms and Conditions (https://onlinelibrary.wiley.com/terms-and-conditions) on Wiley Online Library for rules of use; OA articles are governed by the applicable Creative Commons License

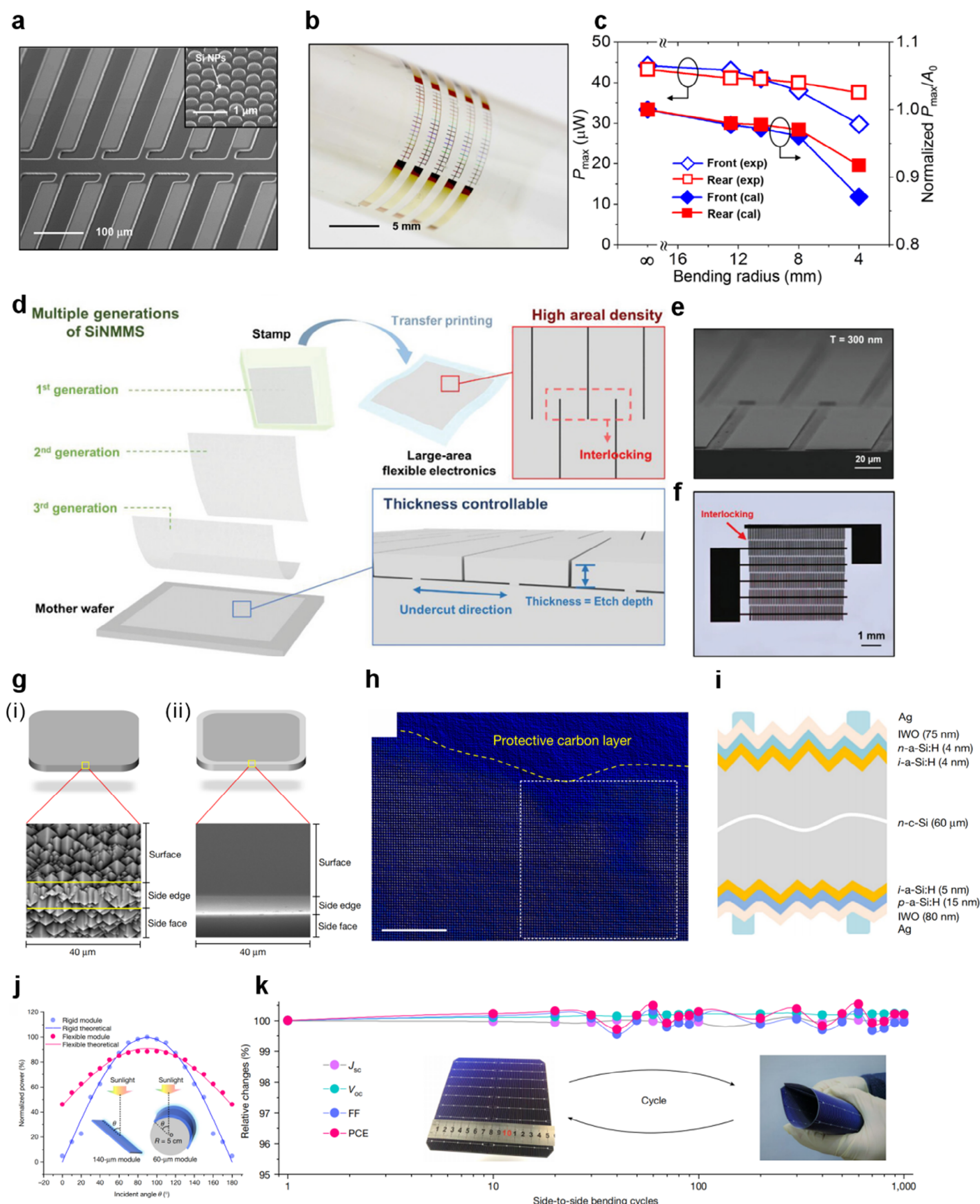

Figure 18. Preparation and performance of flexible and large-scale SiNM solar cells. a) SEM images of flexible SiNM microcells (inset: SiNM with nanopore structures). b) Flexible SiNM solar cells on a bending PET surface. c) Calculation and experimental results of the maximum power density of SiNM microcells. Reproduced with permission.[67] Copyright 2014, American Chemical Society. d) Illustration of recyclable fabrication of SiNMs from mother bulk Si. e) SEM image of interconnected SiNM on mother Si substrate. f) Optical image of flexible Si solar cell prepared with interlocking SiNMs. Reproduced with permission.[60] Copyright 2023, Wiley-VCH. g) Illustrations and SEM images of crystalline SiNM wafer (left) and marginal-blunted SiNM wafer (right). h) Colored HAADF-STEM image of the fracture surface of blunted-SiNM. i) Design of large-scale flexible SiNM solar cells. j) Relationship between collected power and incident angle in rigid and flexible SiNM solar cells. k) Bending stability of 15.6 cm × 15.6 cm SiNM solar cells. Reproduced with permission.[16] Copyright 2023, Springer Nature.

 © 2025 Wiley-VCH GmbH

16163028, 2025, 35, Downloaded from https://advanced.onlinelibrary.wiley.com/doi/10.1002/adfm.202502191 by Fudan University, Wiley Online Library on [08/03/2026]. See the Terms and Conditions (https://onlinelibrary.wiley.com/terms-and-conditions) on Wiley Online Library for rules of use; OA articles are governed by the applicable Creative Commons License

16163028, 2025, 35, Downloaded from https://advanced.onlinelibrary.wiley.com/doi/10.1002/adfm.202502191 by Fudan University, Wiley Online Library on [08/03/2026]. See the Terms and Conditions (https://onlinelibrary.wiley.com/terms-and-conditions) on Wiley Online Library for rules of use; OA articles are governed by the applicable Creative Commons License

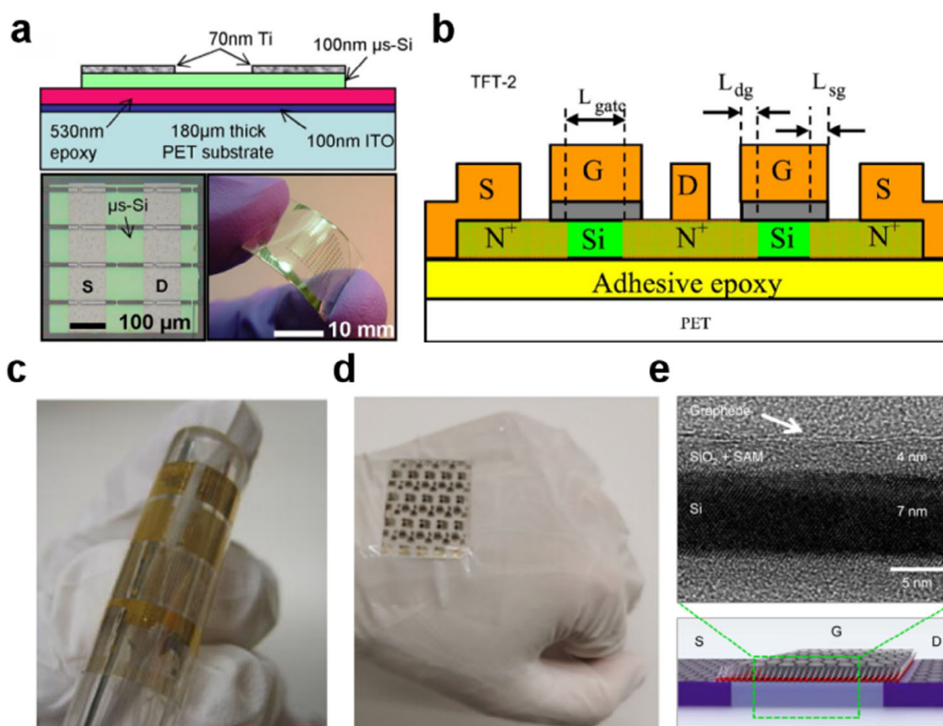

Figure 19. Design and frequency characteristics of SiNM flexible transistors. a) Structure and morphology of flexible SiNM ribbons transistors. Reproduced with permission.[148] Copyright 2005, AIP Publishing. b) Cross-sectional structure of a c-SiNM RF TFT. c) Optical image of a strained flexible c-SiNM RF TFT. Reproduced with permission.[66] Copyright 2007, AIP Publishing. d) Optical image of flexible SiNM synaptic transistor on human hand. Reproduced with permission.[62] Copyright 2025, Wiley-VCH. e) TEM image and illustration of graphene/ultrathin SiNM TFT. Reproduced with permission.[17a] Copyright 2013, American Chemical Society.

7.1. Flexible SiNM Devices for ICs

As one of the fundamental building blocks of ICs, the performance of FET devices will determine the computational speed and energy consumption of the whole system. Therefore, system-level integration of SiNMs primarily focuses on the flexibility and integration of logic computing devices and sensor components.

Menard et al.[148] introduced a method for fabricating monocrystalline Si thin-film transistors on plastic substrates using dry transfer printing (**Figure 19a**). These devices exhibited an effective electron mobility of ≈240 cm^2 V^{-1} s^{-1} in the linear mode and a threshold voltage close to 0 V, while maintaining reliable performance under external strains ranging from −1% to 1.5%. This manufacturing technique allows the use of high-quality inorganic semiconductor materials, such as monocrystalline silicon, gallium arsenide (GaAs), and indium phosphide (InP), in low-cost, large-area electronic systems. For example, recent advances in flexible electronics have demonstrated remarkable progress, with the development of ultraflexible monolithic three-dimensional static random access memory (SRAM) achieving unprecedented integration density and mechanical flexibility.[149] Similarly, Yuan et al.[66,23] designed monocrystalline SiNM transistors (TFTs) on flexible polymer substrates (Figure 19b,c). The strained silicon TFTs demonstrated significantly enhanced electrical performance compared to planar devices, including higher mobility and transconductance. Building on this foundation, recent research has achieved ultra-flexible high-linearity silicon NM synaptic transistor arrays that show exceptional potential for mobile artificial intelligence applications and edge computing (Figure 19d).[62] With appropriate modifications, the maximum cutoff frequency and oscillation frequency of these devices reached 7.8 GHz. The transistor arrays hold great potential for RF applications in communications, remote sensing, and surveillance, offering new ideas for developing high-performance, large-area flexible RF systems.[150] Kim et al.[151] achieved the release of single-crystal SiNM MOSFETs from (111)-oriented silicon substrates without the need for additional device fabrication on the target substrate. The transferred SiNM MOSFETs maintained a high mobility of 370 cm^2 V^{-1} s^{-1} and an on/off ratio exceeding >10^5, overcoming the limitations of traditional SiNM transfer processes in terms of fabrication challenges and functional complexity on the target substrate. At the device level, the unique optical properties and quantum effects of ultrathin SiNMs have already been applied. Koo et al.[17a] studied the quantum confinement effects of ultrathin SiNMs and their applications in flexible transparent devices, revealing their distinctive physical and electronic properties. As the thickness of SiNMs decreases to the nanoscale (particularly below 10 nm), their electronic and optical properties undergo changes due to quantum confinement effects, resulting in extremely high optical transparency in the visible light range. Transistors based on ultrathin SiNMs exhibit excellent electrical performance, including a high mobility of 200 cm^2 V^{-1} s^{-1} after flexing, a low subthreshold swing of less than 90 mV dec^{-1}, and a high on/off ratio of 10^6. Currently,

 © 2025 Wiley-VCH GmbH

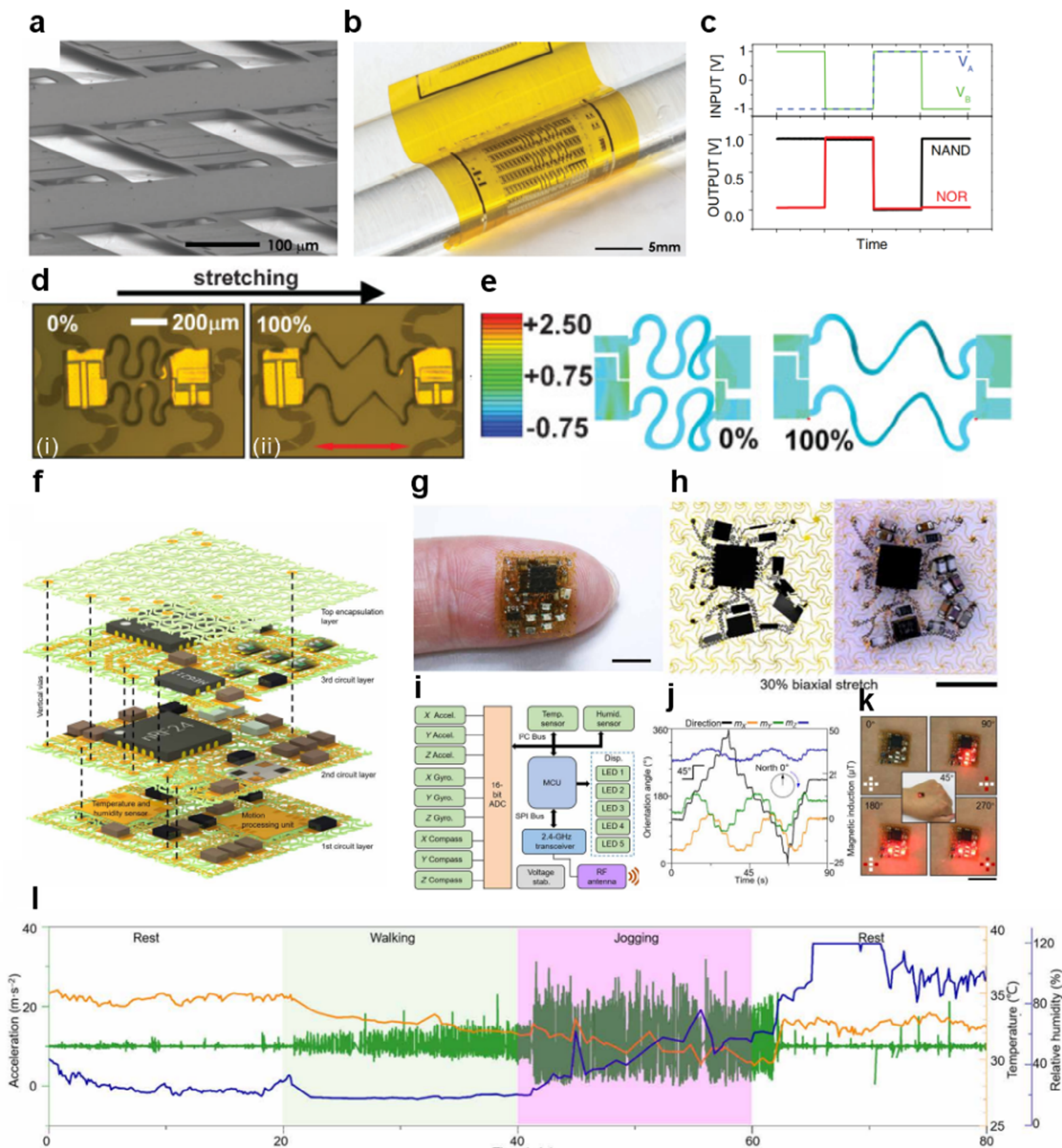

Figure 20. Design and array integration of SiNM flexible CMOS devices. a) SEM image of suspended c-SiNM MOSFET. b) Transferred c-SiNM MOSFET array on a flexible substrate. c) Logical operation of NAND and NOR logic gates based on flexible c-SiNM MOSFETs. Reproduced with permission.[63] Copyright 2011, Wiley-VCH. d) Optical image of stretchable serpent SiNM CMOS inverter. e) FEM simulation of serpentine SiNM CMOS inverter under tensile strain of 100% and then recover to 0%. Reproduced with permission.[153] Copyright 2009, Wiley-VCH.

flexible arrays of SiNMs are also advancing toward composite material systems and industrially compatible processes, further broadening their application potential (Figure 19e).[152]

SiNM-based CMOS devices have also been extensively studied, laying a solid foundation for the development of flexible ICs.[154] Chung et al.[63] developed a method for fabricating CMOS inverters and three-stage ring oscillators on PET substrates (**Figure 20**a,b). Under a supply voltage of 5 V, these CMOS inverters exhibited good transfer characteristics, with a gain of ≈150 and noise margins of ≈3.9 V and 0.6 V for high and low levels, respectively. When subjected to bending with radii between 25.5 and 4.5 mm, corresponding to surface strain values of 0.051%

 © 2025 Wiley-VCH GmbH

16163028, 2025, 35, Downloaded from https://advanced.onlinelibrary.wiley.com/doi/10.1002/adfm.202502191 by Fudan University, Wiley Online Library on [08/03/2026]. See the Terms and Conditions (https://onlinelibrary.wiley.com/terms-and-conditions) on Wiley Online Library for rules of use; OA articles are governed by the applicable Creative Commons License

16163028, 2025, 35, Downloaded from https://advanced.onlinelibrary.wiley.com/doi/10.1002/adfm.202502191 by Fudan University, Wiley Online Library on [08/03/2026]. See the Terms and Conditions (https://onlinelibrary.wiley.com/terms-and-conditions) on Wiley Online Library for rules of use; OA articles are governed by the applicable Creative Commons License

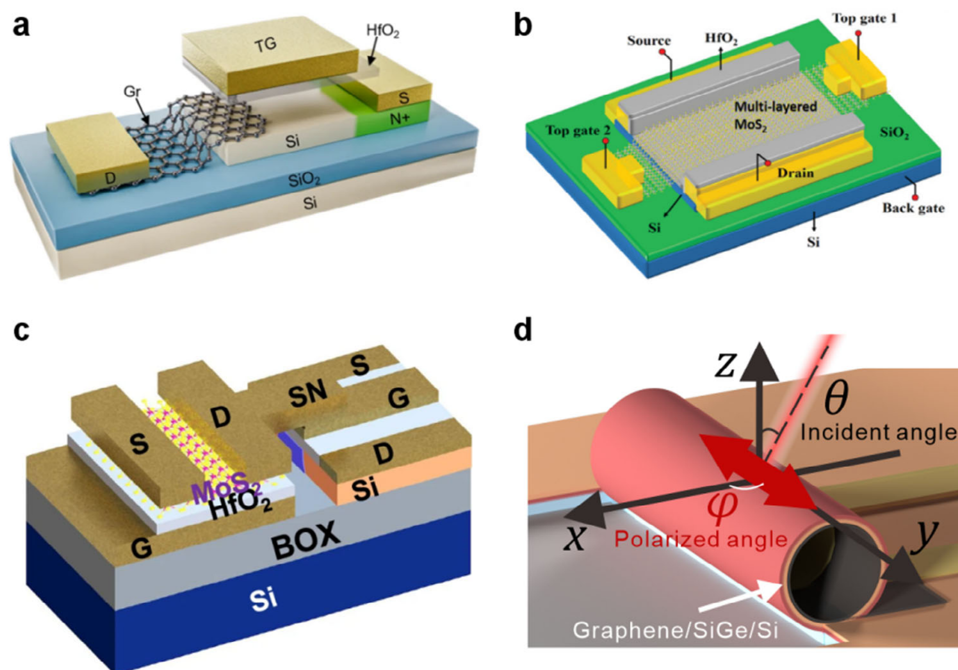

Figure 21. Device design based on 2D materials/SiNM. a) Schematic diagram of the graphene/SOI heterojunction VSFET device structure. Reproduced with permission.[157] Copyright 2024, Springer Nature. b) Schematic diagram of the MoS_2/HfO_2/SOI phototransistor. Reproduced with permission.[158] Copyright 2019, Wiley-VCH. c) Schematic diagram of 2T-eDRAM composed of p-type SOI FET and n-type MoS_2 FET. Reproduced with permission.[159] Copyright 2024, Wiley-VCH. d) Schematic diagram of the graphene/SiGe/SiNM microtube photodetector. Reproduced with permission.[21] Copyright 2024, Wiley-VCH.

to 0.29%, the results showed only slight deviations in maximum gain and noise margins with varying input voltages (Figure 20c). Building on this, Kim et al.[153] proposed a method for integrating high-quality electronic materials, such as monocrystalline Si nanoribbons, with ultrathin plastic and elastomer substrates to achieve high-performance n-type and p-type MOSFETs, CMOS logic gates, ring oscillators, and differential amplifiers (Figure 20d). FEM studies demonstrated that the circuit maintained its integrity even under compressive strains of −3.9%, showing broad application prospects in smart surgical gloves and electronic eye imaging devices (Figure 20e). Currently, ICs and microprocessors based on metal oxides have already been studied, while the standardized transfer and flexible processing of large-area SOI remain to be developed. These advancements are expected to contribute to the industrialization of flexible high-speed electronics.[155]

7.2. 2D Material/SiNM Electronics

2D materials, as an emerging material system, are attracting attention due to their high carrier mobility and unique band structures.[156] Das et al.[147e] utilized a 12 nm-thick ultrathin SiNM as the material for graphene-SiNM vertical field-effect tunneling transistors. Thanks to the atomic-scale thickness of SiNM, current transport in the transistor is primarily dominated by tunneling effects rather than thermally activated effects, ensuring good stability over a temperature range of 125–300 K. Additionally, the energy barrier of the ultrathin SiNM is only 87 meV, which facilitates electron tunneling, making it an ideal material for high-performance, low-power transistors. Combining these materials with SiNMs, known for their high stability and process maturity, offers transformative opportunities for "more-than-Moore" Law device designs. Yuan et al.[157] developed a vertical stacked FET (VSFET) based on graphene/silicon heterojunctions, using graphene as the drain material. The gate voltage enhances the electric field at the drain, triggering avalanche ionization in the depletion region and creating electron-hole pairs. This reduces the barrier height through a positive feedback mechanism, enabling steep switching behavior. The VSFET achieves an average subthreshold swing of 16 μV dec^{-1} at a low operating voltage of 0.4 V, significantly outperforming the thermodynamic limit of 60 mV dec^{-1} in conventional MOSFETs, which is critical for power-efficient high-integration devices (**Figure 21**a). Deng et al.[158] proposed a phototransistor using a MoS_2/HfO_2/SOI structure where photogating effects are simultaneously formed in the top MoS_2 gate and the substrate Si gate. These effects modulate the channel current, enabling tunable bipolar photoresponsivity ranging from +7000 A W^{-1} (Si gate-dominated) to 0 A W^{-1} (balanced) and −8000 A W^{-1} (MoS_2 gate-dominated). The top gate voltage corresponding to zero responsivity shifts with incident wavelength at a resolution as high as 2 nm, enabling filter-free color imaging and advanced high-dimensional optoelectronic sensing (Figure 21b). Xiao et al.[159] designed a 2T-eDRAM structure combining Si transistors for read operations and MoS_2 transistors for write operations. MoS_2, with its wide bandgap and atomic-layer thickness, suppresses short-channel effects and reduces off-state current, achieving static power

 © 2025 Wiley-VCH GmbH

16163028, 2025, 35, Downloaded from https://onlinelibrary.wiley.com/doi/10.1002/adfm.202502191 by Fudan University, Wiley Online Library on [08/03/2026]. See the Terms and Conditions (https://onlinelibrary.wiley.com/terms-and-conditions) on Wiley Online Library for rules of use; OA articles are governed by the applicable Creative Commons License

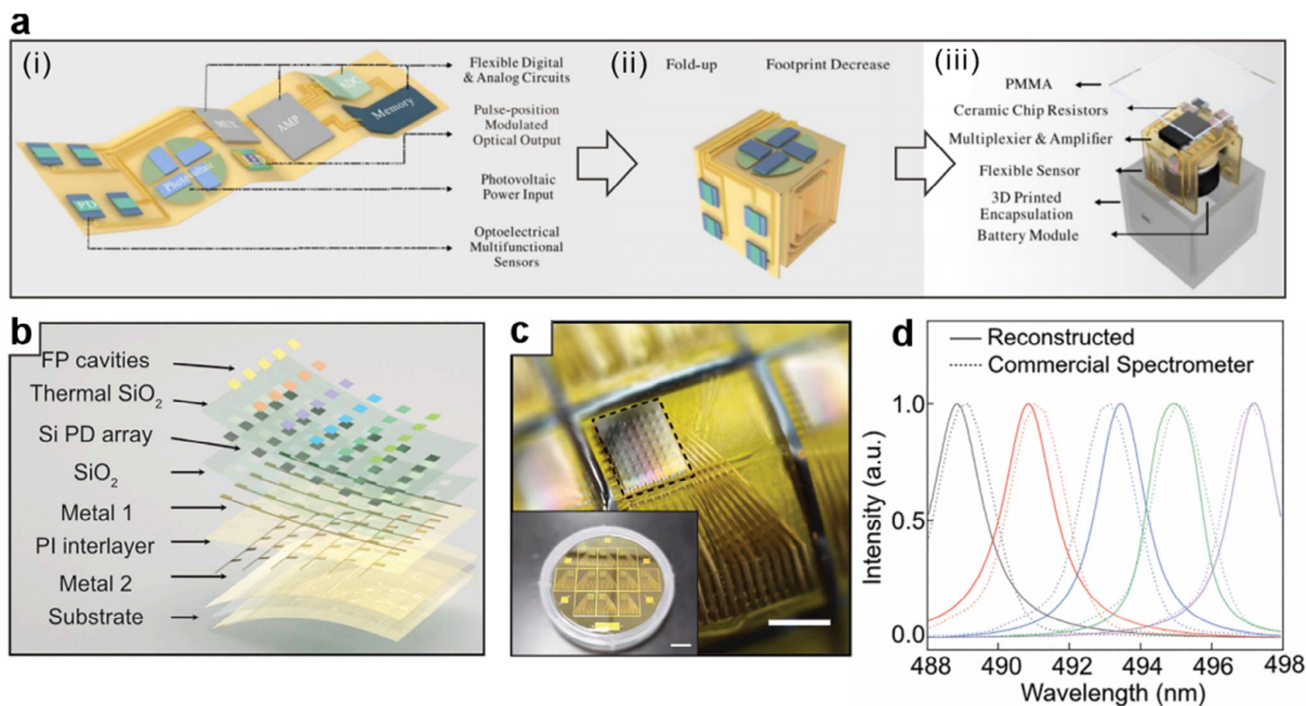

Figure 22. Systematical design of SiNM flexible devices and miniatured spectrometers. a) Schematic diagram of foldable SiNM digital dust: i) key part of an integrated smart digital dust, ii) miniatured integration of digital dust via flexible folding, and iii) system-level design of SiNM digital dust with encapsulation and external power. Reproduced with permission.[164] Copyright 2022, Elsevier. b) Exploded-view of SiNM miniaturized spectrometers. c) Optical image of a SiNM miniaturized spectrometer unit (Inset: 2-inch wafer of SiNM miniaturized spectrometers). d) Performance comparison between miniaturized SiNM spectrometer and commercial spectrometer in monochromatic spectra reconstruction. Reproduced with permission.[22c] Copyright 2024, National Academy of Sciences.

consumption five orders of magnitude lower than traditional DRAM (Figure 21c). It offers ultra-long data retention times (≈6000 s), while the Si transistor provides high on-current and sensitivity of 35 μA μm^{-1}. Tong et al.[160] introduced a vertically stacked CFET structure combining p-type SOI FETs with n-type MoS_2-based FETs. The three-layer MoS_2 serves as the n-type channel, and a stacked metal gate ensures mobility matching. The CFET inverter achieves a voltage gain of 142.3 at 3 V supply voltage and 1.2 at 100 mV supply, with power consumption as low as 64 pW. Its scalable fabrication on four-inch wafers demonstrates the feasibility of 2D materials/SiNM integration for production lines. Zhang et al.[21] utilized strain engineering to fabricate self-rolled graphene/SiGe/SiNM microtube photodetectors. Graphene enhances charge transport and readout efficiency, while the semiconductor NM compensates for the low absorption in graphene. The 3D microtube structure facilitates multiple light reflections and focuses light within the cavity. Coupled with the polarization sensitivity of graphene, the device achieves a high linear polarization detection ratio of 16.09 and a communication rate of 778 Mbps, making it promising for IoT and information security applications (Figure 21d). With the growing research on advanced material systems such as 2D semiconductors,[161] perovskites,[146a,162] and MXenes,[163] their synergistic integration with SiNMs is expected to open new directions for advanced functional devices, offering breakthroughs in optoelectronics, sensing, and energy applications (Figure 21a–d).

7.3. Integrated On-Chip SiNM Systems

Currently, most electronic and optoelectronic systems are centered around semiconductor electronic devices, which gives SiNM an advantage in terms of maturity for systematic integration processes. At the same time, thin-film optical systems composed of SiNM with low optical absorption can eliminate the bulky volume caused by complex optical paths or optical components. The low power consumption characteristics of SiNMs enable effective power management in high-density integration, reducing volume and providing an innovative design route for miniaturized, cost-effective semiconductor products. You et al.[164] proposed a micro multifunctional sensor based on folded circuits, which can be integrated into a miniature sensor platform with data acquisition, signal processing, and communication capabilities (**Figure 22a**). The smart digital dust, with a volume of less than 1 cm^3 after folded encapsulation, allows for visualization, storage, and analysis of the detected environmental information through a corresponding system and GUI, providing new technological support and broad application prospects for future IoT applications (Figure 22b). Moreover, they[22c] also designed a CMOS-compatible integrated Fabry-Perot resonator based on a SiNM system. Through the efficient fabrication of resonator structures with varying thicknesses, the device can achieve self-referencing for multiple wavelength bands of incident light (Figure 22c). Additionally, a high-precision spectral reconstruction was achieved through an adaptive algorithm, eliminating

 © 2025 Wiley-VCH GmbH

the need for manual parameter adjustments common in traditional methods. The SiNM-based miniaturized spectrometer can be manufactured at the wafer scale, with a resolution and measurement range comparable to commercial fiber spectrometers, showcasing the potential of SiNM in chip-level manufacturing and applications (Figure 22d).[22c]

8. Summary and Outlook

SiNMs and their microstructures exhibit promising applications in optoelectronic detection, material sensing, biological diagnostics, and energy storage. The preparation of materials fundamentally determines their mechanical, electrical, and thermal properties, while material uniformity and stability are critical for device array formation and yield in wafer-scale production. At the device level, the SiNM is engineered to achieve specific functionalities. The aim is to attain the desired performance in SiNM through appropriate design and fabrication processes, reducing most adverse effects on material properties during processing. Through coordinated functionality and integration at the system level, SiNM devices work in synergy to truly meet application demands. Compatibility with existing standards and production line processes is a key prerequisite for the usability of SiNM-based products. Consequently, research and optimization of these critical nodes will greatly advance the practical implementation of SiNMs (**Table 2**).

In the field of electronics and optoelectronics based on thin-film materials, especially flexible devices, various material systems beyond SiNM have also demonstrated unique properties and application potential, attracting widespread attention (**Figure 23** and **Table 3**). III-V semiconductor materials (e.g., InP, GaAs) are renowned for their excellent carrier mobility and high-frequency performance, making them widely used in high-speed electronic devices, optical communications, and lasers.[165] Their high mobility positions them prominently in high-frequency amplifiers and photodetectors. However, the epitaxy-based material preparation and complex quantum well designs pose cost challenges for widespread application, and their relatively weak resistance to oxidative acids hinders the advancement of flexible processes. Metal oxides (e.g., ZnO, IGZO) exhibit high transparency, showing tremendous potential in transparent flexible electronic devices and display technologies.[166] Preparation processes such as roll-to-roll techniques are relatively mature, enabling continuous, large-area production at low costs. However, the band structure of such materials inherently limits their carrier mobility, restricting their performance in high-speed devices. 2D materials (e.g., graphene, MoS_2) offer exceptional electrical properties and thermal conductivity due to their unique layered structures.[167] Furthermore, their atomic-scale thickness results in negligible bending rigidity, making them highly suitable for coupling with flexible substrates or surfaces. Although wafer-scale preparation and flexible integration of 2D materials have been achieved, there is still room for improvement in their compatibility with existing semiconductor processes and material uniformity. Perovskite materials (e.g., $MAPbX_3$, $CSPbX_3$) have garnered attention in photovoltaics and photodetection due to their excellent photoelectric conversion efficiency and low-cost solution synthesis and spin-coating preparation processes.[168] Their tunable bandgap and high light absorption capability make them suitable for flexible solar cells and photodetectors. Organic semiconductors, as emerging flexible electronic materials, can mostly be used to fabricate devices through solution-based spin coating or vacuum filtration methods.[169] These methods are friendly to flexible integration, and their electrical performance can rival that of traditional semiconductor materials. However, the potential toxicity of organic components and solvents in flexible applications, as well as the relatively high cost of raw materials, still fall short of meeting the requirements for large-scale applications. However, these materials exhibit relatively weak chemical and thermal stability, particularly prone to degradation under high humidity and high-temperature conditions, which significantly limits their applications in atmospheric environments or high-power devices. SiNM, as an ultrathin semiconductor material, combines the electrical and chemical properties of silicon, its compatibility with established fabrication processes, and the low rigidity required for flexible devices. Additionally, SiNM exhibits chemical and thermal stability comparable to bulk silicon, sufficient to maintain device performance after flexible processing. It also benefits from a well-established foundation in material preparation. Although material systems such as 2D materials and metal oxides offer irreplaceable advantages in ultrafast optoelectronic device performance and large-scale flexible devices, SiNM and SiNM-based integrated material systems are expected to play a key role in the flexible electronics and optoelectronics field in the future, particularly in the flexible adaptation of traditional planar semiconductor components and the design and standardized fabrication of novel semiconductor MEMS (**Figure 24**).

For different types of SiNM device systems, variations in their advantages and limitations also determine the focus areas for future research (Table 2). For planar high-performance SOI devices, high losses in photonics and chip coupling, as well as power consumption and thermal effects in electronics, are currently the bottlenecks limiting their performance development. For flexible devices, Current research on SiNM devices is particularly limited in terms of high-throughput manufacturing and standardized transfer processes, with SOI delamination still being performed manually. At present, there is no semi-automated or automated process dominated by processing equipment for the delamination of SOI. Especially for ultra-thin SiNMs, their ultra-low bending stiffness and equivalent Young's modulus also indicate their vulnerability to external forces and fragility. During transfer and self-assembly processes, they are also sensitive to surface tension, leading to film fracture or structural collapse. In ultrathin SiNMs, conventional ion implantation and etching processes become challenging to implement, as the thickness-dependent processing precision must be controlled to the nanometer or even sub-nanometer scale, which is far smaller than the cutoff depth of implanted ions. Additionally, the dominance of interface states necessitates timely encapsulation or deposition to prevent oxidation of SiNM at the interface with the atmosphere. Additionally, the corresponding systems for flexible SiNM devices still fall short of integration needs. Most energy storage, signal processing, and data transmission modules require wired connections or have not yet achieved the necessary flexibility, failing to meet the demands of portable devices and in situ biomedical monitoring. In most systems, SiNM devices only achieve standalone sensing or computing functions and are unable to complete the full signal reception-processing-feedback loop. Moreover, most

© 2025 Wiley-VCH GmbH

16163028, 2025, 35, Downloaded from https://advanced.onlinelibrary.wiley.com/doi/10.1002/adfm.202502191 by Fudan University, Wiley Online Library on [08/03/2026]. See the Terms and Conditions (https://onlinelibrary.wiley.com/terms-and-conditions) on Wiley Online Library for rules of use; OA articles are governed by the applicable Creative Commons License

Table 2. Comparison between thin film material for advanced electronics and optoelectronics.

Main material	Device type	Mobility	Response time	Operation wavelength/ bandwidth	Maximum strain/bending	Thermal conductivity	Preparation method	Device fabrication method	Scale	Application	Thermal stability	Chemical stability	Cost	Refs.
Si&Ge	220 nm SOI valley topological nanophotonic structure	N/A	N/A	1360–1492 nm	N/A	N/A	Commercial SOI	Lithography/ PVD/EBL	Device level	On-chip photonic applications.	High	High	Relatively low	[170]
	55–65 µm crystalline silicon solar cell	N/A	N/A	N/A	N/A	N/A	CZ method/ chemical blunting	Lithography/ PECVD/PVD/ screen printing	Device level, 15.6 cm × 15.6 cm wafer	Building-integrated photovoltaics	High	High		[42b]
	220 nm SOI photonic circuits	N/A	N/A	33 GHz	N/A	N/A	Commercial SOI	CMOS-compatible 90-nm lithography	System level	Dense wavelength division multiplexing transceivers	High	High		[171]
	Graphene/40 nm $Si_{0.4}Ge_{0.6}$/30 nm SiNM photodetector	N/A	75 ns (rise)/ 330 ns(fall)	785 MHz	~2.51%($Si_{0.4}Ge_{0.6}$/Si)	N/A	CVD for graphene/MBE for SiGe and Si	Wet transfer/ lithography/ wet etching	Device level, 2-inch wafer	VLC	High	High		[21]
	70 nm SiNM flexible transistor	~631 $cm^2 V^{-1} s^{-1}$	N/A	N/A	Bending radius = 40 mm (device)	N/A	Wet etching and roll printing from SOI	CVD/PVD	Device level	Large-area wearable systems	Medium	High		[172]
	10–100 nm SOI	N/A	N/A	N/A	N/A	100~300 W $m^{-1} K^{-1}$	Commercial SOI	Lithography	Device level	SOI MOSFETs	High	High		[173]
	300 nm SiNM strain gauge	N/A	~200 ms	N/A	30%(device)/ ~0.8 GPa (SiNM)	N/A	Wet etching/transferred from SOI	Wet transfer/ wet etching/ doping/ lithography/ spincoat/PVD	Device level	Human–Machine Interfaces	Medium	High		[174]
	300 nm SiNM/MoS_2/WS_2-Fe nanoparticle sensor	N/A	~second level	N/A	Bendable at cm level	N/A	Wet etching/transferred for SiNM/ MoS_2/WS_2	Thermal growth/lithography	System level	Neurochemical monitoring	Medium	Medium		[68]
	300 nm GeNM/GeO_x NM	~690 $cm^2 V^{-1} s^{-1}$	N/A	N/A	0.38%(GeNM)	N/A	Molecular beam deposition and annealing	N/A	Material level	High-speed flexible TFT	Medium	High		[175]

(*Continued*)

© 2025 Wiley-VCH GmbH
16163028, 2025, 35, Downloaded from https://advanced.onlinelibrary.wiley.com/doi/10.1002/adfm.202502191 by Fudan University, Wiley Online Library on [08/03/2026]. See the Terms and Conditions (https://onlinelibrary.wiley.com/terms-and-conditions) on Wiley Online Library for rules of use; OA articles are governed by the applicable Creative Commons License

Table 2. (Continued)

Main material	Device type	Mobility	Response time	Operation wavelength/bandwidth	Maximum strain/bending	Thermal conductivity	Preparation method	Device fabrication method	Scale	Application	Thermal stability	Chemical stability	Cost	Refs.
III-V semiconductor	500 nm InP laser	N/A	N/A	Laser at 930.5 nm	N/A	N/A	Metal–organic vapor-phase epitaxy (MOVPE)	Lithography/EBL/PECVD	Device level, 12-inch wafer	Distributed feedback laser	Medium	Medium	High	[165a]
	270 nm InGaAsP/250 nm SiNM waveguide	N/A	∼100 ps	Waveguide for 1470–1510 nm	N/A	N/A	MBE for InGaAsP	EBL/bonding/PECVD	Device level, 8 × 8 array	Optical communication and computation	Medium	Medium		[176]
	InGaAs PIN photodiodes	N/A	N/A	60 GHz (−3 dB)	N/A	N/A	Metal–organic CVD	Lithography/EBL/wet etching	Device level	Infrared photodetection	Medium	Medium		[165b]
	GaAs/AlGaAs/InAs/AlGaAs/GaAs coupler	N/A	N/A	N/A	N/A	Laser at 1270–1283 nm	MBE	Wet etching/PVD/FIB	System level	Laser on SOI	Medium	Medium		[108]
	$In_xGa_{1-x}As$/InP transistors	1.2×10^6 $cm^2 V^{-1} s^{-1}$	N/A	172 GHz	N/A	N/A	MBE	Lithography/EBL/wet etching	Device level	Low-noise amplifiers	Medium	Medium		[165c]
	GaN/ $Al_{0.4}Ga_{0.6}$ N:Si transistors	1970 $cm^2 V^{-1} s^{-1}$	N/A	N/A	N/A	N/A	MBE	Lithography/ALD/PVD	Device level	Photonic ICs	Medium	Medium		[177]
Metal oxide	ZnO nanotubes/Graphene flexible sensor	N/A	<100 ms	N/A	Bendable at cm level	N/A	MOVPE for ZnO/CVD for graphene	EBL/flipped transfer/PVD	Device level, 8 × 8 array	Wearable electronics	Medium	High	Low	[166a]
	16–45 µm WO_3 flexible sensor	N/A	∼1.5 s	N/A	Bendable at cm level	N/A	Hydrothermal method	Screen printing	Device level, 4 × 4 array	Respiration rate monitoring	High	High		[166b]
	β-Ga_2O_3 flexible photodetector	N/A	1.63 s (rise)/1.65 s(fall)	N/A	6%(β-Ga_2O_3/$LaSrMnO_3$/$SrTiO_3$)/Bending radius = 7.5 mm (device)	N/A	Pulsed laser deposition (PLD)	Wet etching/magnetron sputtering	Device level	Solar-blind photodetectors	High	High		[166c]
	V_2O_5/ZnO/ITO/PET	N/A	4.9 ms (rise)/9.79ms(fall)	N/A	N/A	N/A	PVD for V_2O_5/ZnO/ITO	PVD	Device level	Transparent photodetector	High	High		[178]
	20 nm ZnO/5 nm AlZnO/5 nm YZnO TFT	71.3 $cm^2 V^{-1} s^{-1}$	N/A	N/A	N/A	N/A	Spray pyrolysis	Lithography/magnetron sputtering/wet etching	Device level, array	High-resolution flat panel displays.	Medium	High		[179]
	Hollow TiO_2 fibrous flexible membrane	N/A	N/A	N/A	0.783 ± 0.234 MPa (TiO_2 flexible membrane)	0.0304 ± 0.00025 W $m^{-1} K^{-1}$	Coaxial electrospinning	Heating	Material level	Thermal insulation applications	High	High		[180]

(*Continued*)

© 2025 Wiley-VCH GmbH

16163028, 2025, 35, Downloaded from https://advanced.onlinelibrary.wiley.com/doi/10.1002/adfm.202502191 by Fudan University, Wiley Online Library on [08/03/2026]. See the Terms and Conditions (https://onlinelibrary.wiley.com/terms-and-conditions) on Wiley Online Library for rules of use; OA articles are governed by the applicable Creative Commons License

Table 2. (Continued)

Main material	Device type	Mobility	Response time	Operation wavelength/ bandwidth	Maximum strain/bending	Thermal conductivity	Preparation method	Device fabrication method	Scale	Application	Thermal stability	Chemical stability	Cost	Refs.
	15 nm IGZO flexible TFT	6.6 ± 1.9 $cm^2 V^{-1} s^{-1}$	N/A	N/A	Bending radius = 13.5 µm (device)/ 1%(IGZO)	N/A	Magnetron sputtering	Spincoat/PVD/ lithography/ wet etching	Device level	Flexible Active-matrix displays	Medium	Medium		[181]
	30 nm SnO_2–TiO_2 NM/perovskite flexible solar cell	N/A	N/A	N/A	Bending radius = 5 mm (device)	N/A	Spincoat for SnO_2–TiO_2/Solution deposition for perovskite/	PVD	Device level	Flexible perovskite solar cells	Medium	Low		[182]
2D materials	Graphene/ metasurface photodetector	900 $cm^2 V^{-1} s^{-1}$	N/A	420 GHz	N/A	N/A	CVD for graphene	EBL/ALD/PVD	Device level	High-speed infrared pho-todetection	Medium	High	Medium	[167a]
	MoS_2 FET	40.65 $cm^2 V^{-1} s^{-1}$	N/A	N/A	N/A	N/A	CVD	Lithography/ALD	Device level, 12-inch wafer	ICs	Medium	Medium		[156c]
	5 µm BP/MXene flexible thin film	N/A	10.9 ms (rise)/ 12.9 ms (fall)	N/A	Bendable at mm level	N/A	Ball milling and sonication for BP/wet etching for MXene	Vacuum filtration	Device level	Biomedical devices and self-powered systems	Low	Low		[167b]
	h-BN/WSe_2/ h-BN flexible photodetector	35 $cm^2 V^{-1} s^{-1}$	0.3 s (rise)/ 13 s (fall)	N/A	Bending radius = 3 cm (device)	N/A	Mechanical exfoliation	Dry transfer/lithography/ PVD/annealing	Device level	High-temperature photodetec-tion	Medium	Medium		[167c]
	PVDF/MoS_2@ZnO nanoparticles flexible membrane	N/A	N/A	N/A	7.97±3.65% (device)	N/A	Liquid exfoliation for MoS_2/liquid growth for ZnO	Spray/ spincoat	Device level	Flexible piezoelectric	Medium	Medium		[183]
	MoS_2 flexible TFT	70 $cm^2 V^{-1} s^{-1}$ (flexible) 100 $cm^2 V^{-1} s^{-1}$ (rigid)	6.7 ns (in oscillator)	24.8 MHz (in oscillator)	Bending radius = 2.4 mm (device)	N/A	CVD	Lithography/ALD/ wet etching	Device level, 4-inch wafer	Implantable logic unit	Medium	Medium		[184]
	Flexible graphene-oxide-based graphene	N/A	N/A	N/A	16% (graphene-oxide/graphene)	1940 ± 113 $W m^{-1} K^{-1}$	Thermal annealing	Thermal annealing	Material level	High-power flexible devices	Medium	High		[185]

(*Continued*)

© 2025 Wiley-VCH GmbH

16163028, 2025, 35, Downloaded from https://advanced.onlinelibrary.wiley.com/doi/10.1002/adfm.202502191 by Fudan University, Wiley Online Library on [08/03/2026]. See the Terms and Conditions (https://onlinelibrary.wiley.com/terms-and-conditions) on Wiley Online Library for rules of use; OA articles are governed by the applicable Creative Commons License

Table 2. (Continued)

Main material	Device type	Mobility	Response time	Operation wavelength/ bandwidth	Maximum strain/bending	Thermal conductivity	Preparation method	Device fabrication method	Scale	Application	Thermal stability	Chemical stability	Cost	Refs.
Perovskite	$MAPbBr_3$/Si photodetector	N/A	520 ns (rise)/2435 ns (fall)	0.67 MHz	N/A	N/A	Vapor-assisted crystallization for $MAPbBr_3$	PVD	Device level	Broadband, highspeed photodetection	Medium	Medium	Relatively low	[168a]
	$CH_3NH_3PbI_3$ film	N/A	N/A	N/A	N/A	0.32 ± 0.03 W m^{-1} K^{-1}	Thermal evaporation	PVD	Device level	Thermoelectrics	Low	Low		[168b]
	$MAPb(I_{n\cdot 9}Cl_{n\cdot 1})$ 3 flexible X-ray detector	0.015 cm^2 V^{-1} (Mobility-Lifetime Product)	6.5 µs	N/A	Bending radius = 2 mm (device)	N/A	Vacuum infiltration and annealing	Lamination/ thermal evaporation	Device level, 7 × 12 array	Medical and industrial imaging	Low	Low		[186]
	$FA_{0.8}Cs_{0.2}PbI_3$/ $CsPbBr_3$/$Cs_{0.75}EA_{0.25}PbBr_3$ flexible LED	N/A	N/A	N/A	N/A	N/A	Recrystallization and dissolution	Inkjet printing	Device level, 6 × 6 cm^2	Flexible lighting and display	Medium	Low		[187]
Non-perovskite organics	PVK/26DC zppy/TPBi/ Hex-$Ir(phq)_2(acac)$/ Ir(ppy)/$Ir(Fppy)_3$ flexible LED	N/A	N/A	N/A	1.5% (device)	N/A	Solution dip-coating	Annealing/thermal evaporation/ALD	Device level	Wearable textile displays	Medium	Medium	High	[169a]
	Rubrene single-crystal nanobelts	21.4–25.2 cm^2 V^{-1}	N/A	N/A	Bending radius = 1.3 mm (device)	N/A	Physical vapor transport	Lithography/ spincoat	Device level	Conformal transistor	Medium	Low		[169b]
	PDMS/PEMF microfiber	N/A	N/A	N/A	N/A	Up to 38.27 W m^{-1} K^{-1}	Vacuum infiltration	Heating	Material level	Thermal interface for LED	Medium	Medium		[188]
	D18-Cl/Y6 photodetector	N/A	81 µs (rise)/ 77 µs (fall)	8.2 kHz (−3dB)	Bending radius = 2 mm (device)	N/A	Solution casting	Spincoat/PVD	Device level	Rare-earth element detection	Medium	Medium		[189]

© 2025 Wiley-VCH GmbH

16163028, 2025, 35, Downloaded from https://advanced.onlinelibrary.wiley.com/doi/10.1002/adfm.202502191 by Fudan University, Wiley Online Library on [08/03/2026]. See the Terms and Conditions (https://onlinelibrary.wiley.com/terms-and-conditions) on Wiley Online Library for rules of use; OA articles are governed by the applicable Creative Commons License

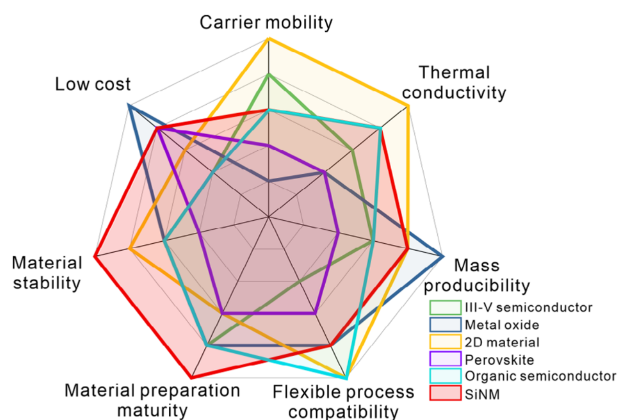

Figure 23. Comparison of material performance and scalability between SiNM, III-V semiconductor, metal oxide, 2D material, perovskite, and organic semiconductor.

flexible SiNM devices are fabricated on SOI wafers, which are significantly more expensive than bulk silicon.

In the case of self-rolled SiNM devices, several major challenges exist: First, the three-dimensional structures on rigid substrates are extremely fragile under external forces, and device movement or environmental vibrations can significantly compromise their stability. Moreover, the formation of three-dimensional structures typically relies on the deposition of strain layers and wet etching processes for sacrificial layers, which impose strict requirements on the uniformity of the device and the chemical stability of the etching process. The integration of a greater variety of materials in the device layer further reduces the options available for sacrificial layer materials. Currently, the self-rolled SiNM is still predominantly metal-Si-metal, lacking gate-controlled device designs that offer lower energy consumption and higher speed. There is limited experience in developing array structures, subsequent encapsulation, and chip-level designs. Additionally, application scenarios beyond photodetectors remain relatively limited (Figure 24).

SiNM with MACE techniques can directly serve as device structures. However, the strong corrosiveness of the etching solution and the inability to detach from the bulk silicon substrate mean that hetero-integration with other thin-film materials is nearly impossible. Moreover, the primary focus of this process is to enhance intrinsic properties such as absorption rate and specific surface area, while it contributes little to introducing new functionalities for system applications.

1) At the material level, finding an economical and efficient method to fabricate single-crystal SiNM is crucial. Currently, the price of SOI remains at least 10 times higher than that of monocrystalline silicon of the same size.[190] The primary research and development directions should focus on repeatable SOI processing methods and equipment-driven semi-automated or automated transfer processes, aiming to reduce costs from the two main steps of flexible device fabrication.[60] The development of transfer stamp materials or target substrates aimed at transfer processes will also help improve the efficiency and stability of large-scale SiNM production.[191] By utilizing the physical and chemical properties of the surface energy and surface states of SiNM itself, techniques for the transfer and modification of ultra-thin SiNM can be developed, enabling fabrication schemes with nanometer-level precision.[38,55,192] Developing a flexible substrate transfer method that enables simultaneous separation and bonding of SiNM onto substrates would help achieve lower-cost self-assembly.[193] Moreover, strain SOI or advanced epitaxial methods based on material lattice mismatch can address issues such as crystal quality and defects in SiNM.[194] In the future, it is also expected that thinned SOI substrates could be introduced into roll-to-roll processing systems,

Table 3. Comparison of the characteristics and perspectives of SiNMs via different methods.

Type	Advantages	Applications	Challenges	Development route
Strain-free SiNM on rigid substrate	High mechanical stability; Mature process; large-scale fabrication; Maintains crystalline quality	Optoelectronic devices; Large-scale ICs; Precision optical components	Non-stretchable; Difficult to miniaturize; Poor biocompatibility	3D ICs; Photonic and optoelectronic systems
Strain-free SiNM on flexible substrate	Adapts to non-planar surfaces; Lightweight and highly portable; Implantable with good biocompatibility	Physiological monitoring devices; Flexible displays; In-situ sensors	Complex fabrication processes; Limited reliability; Poor cycle durability; Lack of standardized	High-stability, high-sensitivity devices; Large-area transfer; High-precision alignment technology
Self-rolled SiNM with intrinsic strain gradient	Simple process; functional integration; Good control	MEMS; Multi-dimensional optoelectronic detectors; Drug delivery and microfluidic components	Relatively poor performance consistency; Structural design time-consuming; Encapsulation and integration	Large-area microstructured device fabrication; Developing encapsulation and integration processes for microstructures; Strengthening theoretical models to guide design
Buckled SiNM with external strain engineering	Structural stability; Tunable strain	Wearable/implantable sensors; Photodetectors	Complex processing and design; Limited range of material	Identifying and integrating functional material systems; Developing reconfigurable devices
MACE SiNM structures	High aspect ratio; Free to dry etching	Solar cells; Metasurfaces	Incompatible to most material; Unable to release	Buffer layer structure; Alternative metal mask

© 2025 Wiley-VCH GmbH

16163028, 2025, 35, Downloaded from https://onlinelibrary.wiley.com/doi/10.1002/adfm.202502191 by Fudan University, Wiley Online Library on [08/03/2026]. See the Terms and Conditions (https://onlinelibrary.wiley.com/terms-and-conditions) on Wiley Online Library for rules of use; OA articles are governed by the applicable Creative Commons License

16163028, 2025, 35, Downloaded from https://advanced.onlinelibrary.wiley.com/doi/10.1002/adfm.202502191 by Fudan University, Wiley Online Library on [08/03/2026]. See the Terms and Conditions (https://onlinelibrary.wiley.com/terms-and-conditions) on Wiley Online Library for rules of use; OA articles are governed by the applicable Creative Commons License

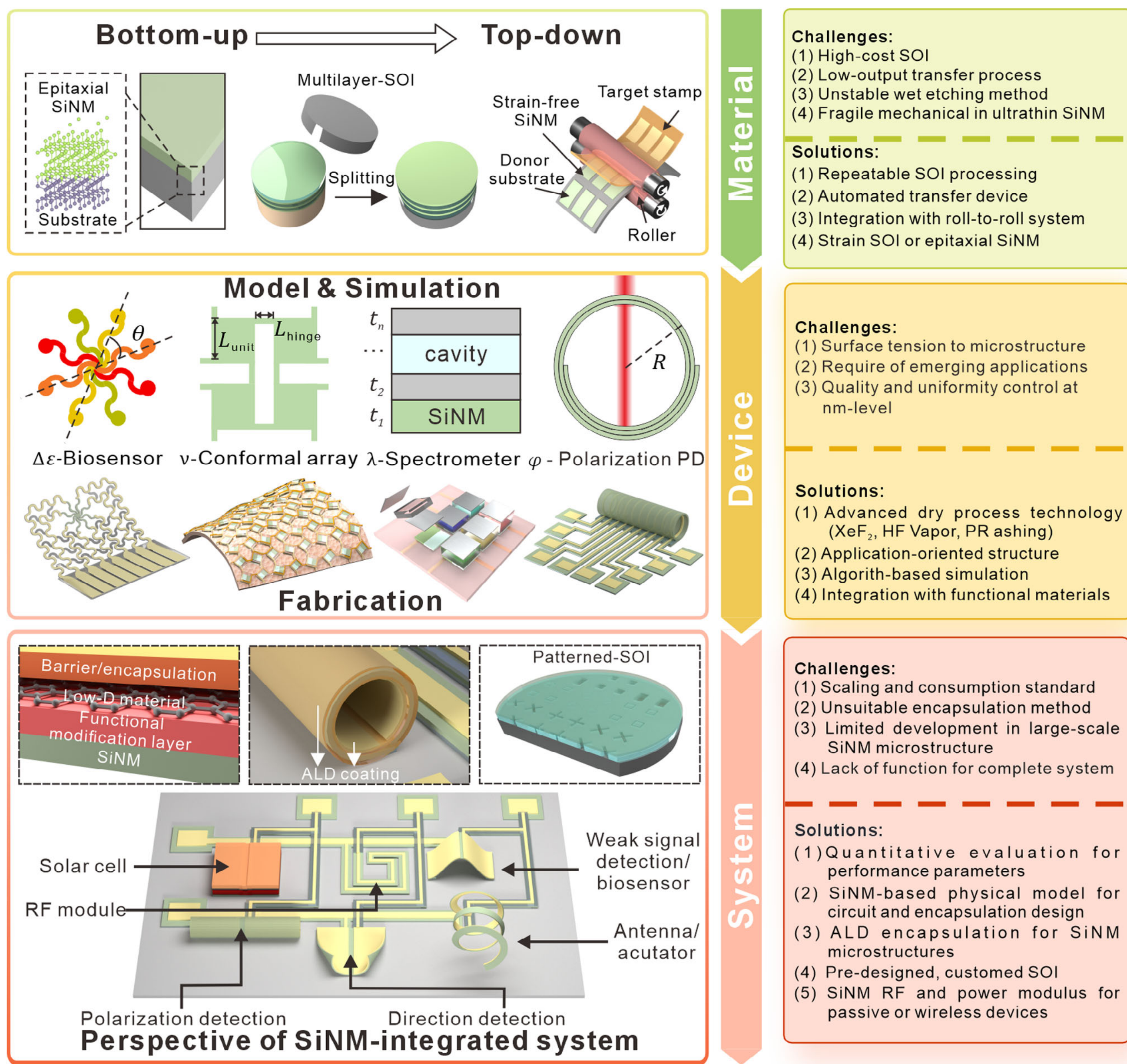

Figure 24. Key issues and development strategies for integration and application of SiNMs.

enabling the streamlined production of desired SiNM components through large-scale, high-yield transfer. SiNM processing based on thinning methods bypasses the transfer step, achieving flexibility while remaining on the substrate. By improving these material fabrication techniques, the overall cost and efficiency of SiNM film production can be enhanced. When the cost of SOI-based wafers is reduced to 30%–50% of the current level, SiNM flexible devices can be applied in a wider range of fields.

2) At the device level, the exploration of SiNM in multifunctional applications and emerging silicon-based fields (e.g., silicon photonics and three-dimensional FET structures) remains limited, posing new requirements for the coupling of non-destructive device fabrication processes with the latest material systems. Relying solely on the electrical properties of silicon itself, devices will be insufficient to meet the performance requirements of current advanced applications. By employing advanced XeF_2/HF etching and common gas-phase etching techniques, it is possible to effectively etch conventional oxides, nitrides, and metallic materials without causing damage to SiNM.[195] Currently, SiNM faces challenges in adapting to small curvature or highly plastic surfaces in flexible applications, which can be addressed by optimizing metamaterial structures. Such structures, with negative Poisson's ratios, can exhibit remarkable stretchability and compression sensing capabilities in nonlinear elastic materials.[196] Meanwhile, in situ coupling with ferroelectric and 2D materials enables the integration of sensing, storage, and computation within a

 © 2025 Wiley-VCH GmbH

single SiNM-based device, granting SiNM devices the potential to transcend traditional architectures. Transfer techniques allow the vertical position of SiNM in three-dimensional device structures to be freely determined. Controlling strain gradients is crucial to ensuring uniform performance in buckled and self-rolled SiNM devices. For buckled SiNM, theoretical modeling and finite element analysis methods need to be established to guide the formation of buckled structures, enabling precise control over the amplitude, periodicity, and other morphological details of the buckles.[32] The complex optical propagation along the in-plane direction of thin films in out-of-plane structures can also provide new momentum for the development of optical neural networks, with particular attention to modules involving randomization and loss functions. For SiNM structures fabricated using the MACE process, the development of thick silicon substrates with buffer layers and low-cost metal masks will help mitigate application constraints. Therefore, the pursuit of low-damage processes and the application of new mechanical, optical, and electrical models will be key objectives for SiNM devices.

3) At the system integration level, compared with the mature planar CMOS process, the scaling technology and energy consumption of SiNM systems have not yet been fully addressed and remain at the stage of feasibility verification. To advance toward system and product-level applications, it is necessary to evaluate component quality within the system using quantitative metrics such as yield, mobility, and threshold voltage. Additionally, the introduction of physical models and device simulations at the ICs scale for SiNMs, with the consideration of flexibility or microstructures as coupling factors, is essential to enable the application of carrier transport mechanisms in SiNM-based systems.[197] While exploring compatibility with existing semiconductor production lines, it is crucial to design macroscopic encapsulation modules that ensure signal integrity. The development of linear arrays based on identical microtubes and focal plane arrays with multiple microtubes holds great potential, as they offer a wide field of view without requiring additional optical components.[198] Encapsulation technologies that do not conflict with 3D structures and their functionalities should be considered.[199] Traditional encapsulation methods, such as flip-chip bonding and resin encapsulation, may not be suitable for self-rolled devices. A promising approach is to use ALD to deposit Al_2O_3 thin films to stabilize the structures and isolate them from the external environment, followed by wire bonding to connect the chip to an external framework. In MEMS applications, SOI substrates with pre-designed sacrificial layers or microcavities can be used for fabrication, eliminating the cost of additional exposure and etching in subsequent processes. Research is also needed to develop SiNM devices that integrate components such as capacitors, inductors, and resistors into ICs, enabling efficient fabrication of multiple components on a single chip while maintaining compatibility with most existing silicon process production lines.[200] Meanwhile, the introduction of 3D architectures can further enhance the integration density of SiNM, and on this basis, modularization with interfaces can be conveniently integrated into any required scenarios. It should be noted that SiNM systems cannot fully replace existing ICs; instead, they are more inclined to serve as optimized options in specific application scenarios. However, to realize this vision, it is essential to accelerate the industrialization and practical application of SiNM systems.

In summary, SiNMs represent an emerging class of semiconductor materials that offer compatibility with most traditional silicon semiconductor processes and mature device design, while their nanoscale thickness imparts low bending stiffness and remarkable deformation capabilities. Their quasi-2D nature bridges the gap between nanoscale and macroscale structures. To date, many traditional semiconductor functional devices have been successfully fabricated using SiNMs. The preparation of SiNMs has been extensively studied, including bottom-up deposition methods and top-down etching techniques, with corresponding processes developed to produce strain-free or specifically strain-graded SiNMs. Building on the above foundation, SiNMs can be designed and fabricated into flexible devices, buckled microstructures, rolled microstructures, and high aspect ratio structures, overcoming the integration and functional limitations of planar silicon devices, and elevating the application value and potential of silicon semiconductor devices to new heights. Currently, efforts are being directed toward the development of complete systems and products. Although challenges remain in large-scale integrated manufacturing, process costs, and practicality, clear development roadmaps and promising technologies currently exist to address these issues. The unique material and structural properties of SiNMs have already demonstrated their value in fields such as optoelectronics, biomedicine, energy, and material sensing. We believe that in the coming decades, SiNM materials and technologies will become an indispensable aspect of the ICs field.

Acknowledgements

Z.Z. and Y.W. contributed equally to this work. This work was supported by the National Key Technologies R&D Program of China (No. 2021YFA0715302, 2022YFB3204800, and 2022YFB4400010), the National Natural Science Foundation of China (No. 523B2107, 61975035, 62375054, and 62404232), the Science and Technology Commission of Shanghai Municipality (No. 21142200200 and 22ZR1405000), the China National Postdoctoral Program for Innovative Talents (No. BX20240394), the China Postdoctoral Science Foundation (No. 2024M763410), Shanghai Post-doctoral Excellence Program (No. 2024797), CAS Project for Young Scientists in Basic Research (Grant No. YSBR-081), and Strategic Priority Research Program of the Chinese Academy of Sciences (Grant No. XDB0670000). Z.Z. is supported by the Special Program for Doctoral Students under the Youth Talent Support Project of the China Association for Science and Technology.

Conflict of Interest

The authors declare no conflict of interest.

Keywords

device and system integration, energy harvesting, photodetectors, sensors, silicon nanomembrane

Received: January 22, 2025
Revised: March 12, 2025
Published online: April 1, 2025

 © 2025 Wiley-VCH GmbH

16163028, 2025, 35, Downloaded from https://advanced.onlinelibrary.wiley.com/doi/10.1002/adfm.202502191 by Fudan University, Wiley Online Library on [08/03/2026]. See the Terms and Conditions (https://onlinelibrary.wiley.com/terms-and-conditions) on Wiley Online Library for rules of use; OA articles are governed by the applicable Creative Commons License

[1] a) C. Ballif, F.-J. Haug, M. Boccard, P. J. Verlinden, G. Hahn, *Nat. Rev. Mater.* **2022**, *7*, 597; b) S. Shekhar, W. Bogaerts, L. Chrostowski, J. E. Bowers, M. Hochberg, R. Soref, B. J. Shastri, *Nat. Commun.* **2024**, *15*, 751; c) C. Liu, J. Guo, L. Yu, J. Li, M. Zhang, H. Li, Y. Shi, D. Dai, *Light. Sci. Appl.* **2021**, *10*, 123; d) M. Ge, C. Cao, G. M. Biesold, C. D. Sewell, S.-M. Hao, J. Huang, W. Zhang, Y. Lai, Z. Lin, *Adv. Mater.* **2021**, *33*, 2004577; e) M. F. Gonzalez-Zalba, S. de Franceschi, E. Charbon, T. Meunier, M. Vinet, A. S. Dzurak, *Nat. Electron.* **2021**, *4*, 872.

[2] M. Ieong, B. Doris, J. Kedzierski, K. Rim, M. Yang, *Science* **2004**, *306*, 2057.

[3] a) V. K. Khanna, in *Integrated Nanoelectronics: Nanoscale CMOS, Post-CMOS and Allied Nanotechnologies*, Springer India, New Delhi, **2016**; b) S. Jallepalli, J. Bude, W. K. Shih, M. R. Pinto, C. M. Maziar, A. F. Tasch, *IEEE Trans. Electron. Dev.* **1997**, *44*, 297.

[4] a) F. Cavallo, M. G. Lagally, *Soft Matter* **2010**, *6*, 439; b) D. H. Kim, J. H. Ahn, W. M. Choi, H. S. Kim, T. H. Kim, J. Z. Song, Y. G. Y. Huang, Z. J. Liu, C. Lu, J. A. Rogers, *Science* **2008**, *320*, 507; c) J. J. Wortman, R. A. Evans, *J. Appl. Phys.* **1965**, *36*, 153.

[5] a) M. W. M. Graef, in *IEEE Int. Roadmap for Devices Systems Outbriefs*, IEEE, Piscataway, NJ **2021**; b) H. Wong, *2021 IEEE 32nd International Conference on Microelectronics (MIEL)*, IEEE, Piscataway, NJ **2021**.

[6] S. A. Ahad, T. Kennedy, H. Geaney, *ACS Energy Lett.* **2024**, *9*, 1548.

[7] a) T. Zhang, Y. Sun, R. Hu, W. Qian, L. Yu, *Adv. Electron. Mater.* **2024**, 2400615; b) L. Wu, Z. Hu, L. Liang, R. Hu, J. Wang, L. Yu, *Nat. Commun.* **2025**, *16*, 965.

[8] a) A. B. Sachid, M. Tosun, S. B. Desai, C.-Y. Hsu, D.-H. Lien, S. R. Madhvapathy, Y.-Z. Chen, M. Hettick, J. S. Kang, Y. Zeng, J.-H. He, E. Y. Chang, Y.-L. Chueh, A. Javey, C. Hu, *Adv. Mater.* **2016**, *28*, 2547; b) R. S. Pal, S. Sharma, S. Dasgupta, *2017 Conference on Emerging Devices and Smart Systems (ICEDSS)* **2017**; c) Y. C. Huang, M. H. Chiang, S. J. Wang, J. G. Fossum, *IEEE J. Electron. Devices Soc.* **2017**, *5*, 164.

[9] a) C. Rogers, A. Y. Piggott, D. J. Thomson, R. F. Wiser, I. E. Opris, S. A. Fortune, A. J. Compston, A. Gondarenko, F. Meng, X. Chen, G. T. Reed, R. Nicolaescu, *Nature* **2021**, *590*, 256; b) T. Komljenovic, D. Huang, P. Pintus, M. A. Tran, M. L. Davenport, J. E. Bowers, *Proc. IEEE* **2018**, *106*, 2246; c) W. Bogaerts, L. Chrostowski, *Laser Photonic Rev.* **2018**, *12*, 1700237.

[10] a) M. Han, L. Chen, K. Aras, C. Liang, X. Chen, H. Zhao, K. Li, N. R. Faye, B. Sun, J. H. Kim, W. Bai, Q. Yang, Y. Ma, W. Lu, E. Song, J. M. Baek, Y. Lee, C. Liu, J. B. Model, G. Yang, R. Ghaffari, Y. Huang, I. R. Efimov, J. A. Rogers, *Nat. Biomed. Eng.* **2020**, *4*, 997; b) W. J. Westerveld, M. Mahmud-Ul-Hasan, R. Shnaiderman, V. Ntziachristos, X. Rottenberg, S. Severi, V. Rochus, *Nat. Photonics* **2021**, *15*, 341; c) A. Y. Takabayashi, H. Sattari, P. Edinger, P. Verheyen, K. B. Gylfason, W. Bogaerts, N. Quack, *J. Microelectromech. Syst.* **2021**, *30*, 322.

[11] X. Zhu, J. Li, H. Yang, F. Zhu, Z. Guo, K. Huang, P. Hang, T. Chen, X. Yu, D. Yang, *Phys. Status Solidi RRL* **2024**, *18*, 2300349.

[12] a) A. M. Kiefer, D. M. Paskiewicz, A. M. Clausen, W. R. Buchwald, R. A. Soref, M. G. Lagally, *ACS Nano* **2011**, *5*, 1179; b) W. Peng, M. Zamiri, S. A. Scott, F. Cavallo, J. J. Endres, I. Knezevic, M. A. Eriksson, M. G. Lagally, *Phys. Rev. Appl.* **2018**, *9*, 024037.

[13] J. L. Snyder, J. Getpreecharsawas, D. Z. Fang, T. R. Gaborski, C. C. Striemer, P. M. Fauchet, D. A. Borkholder, J. L. McGrath, *Proc. Natl. Acad. Sci. U.S.A.* **2013**, *110*, 18425.

[14] a) B. Wu, Z. Zhang, Z. Zheng, T. Cai, C. You, C. Liu, X. Li, Y. Wang, J. Wang, H. Li, E. Song, J. Cui, G. Huang, Y. Mei, *Adv. Mater.* **2023**, *35*, 2306715; b) C. Xu, R. Pan, Q. Guo, X. Wu, G. Li, G. Huang, Z. An, X. Li, Y. Mei, *Adv. Opt. Mater.* **2019**, *7*, 1900823; c) Y. Zhang, Z. Yan, K. Nan, D. Xiao, Y. Liu, H. Luan, H. Fu, X. Wang, Q. Yang, J. Wang, W. Ren, H. Si, F. Liu, L. Yang, H. Li, J. Wang, X. Guo, H. Luo, L. Wang, Y. Huang, J. A. Rogers, *Proc. Natl. Acad. Sci. U.S.A.* **2015**, *112*, 11757.

[15] B. Jeong, H. Cho, H. Keum, S. Kim, D. Michael McFarland, L. A. Bergman, W. P. King, A. F. Vakakis, *Nanotechnology* **2014**, *25*, 465501.

[16] W. Liu, Y. Liu, Z. Yang, C. Xu, X. Li, S. Huang, J. Shi, J. Du, A. Han, Y. Yang, G. Xu, J. Yu, J. Ling, J. Peng, L. Yu, B. Ding, Y. Gao, K. Jiang, Z. Li, Y. Yang, Z. Li, S. Lan, H. Fu, B. Fan, Y. Fu, W. He, F. Li, X. Song, Y. Zhou, Q. Shi, et al., *Nature* **2023**, *617*, 717.

[17] a) H. Jang, W. Lee, S. M. Won, S. Y. Ryu, D. Lee, J. B. Koo, S.-D. Ahn, C.-W. Yang, M.-H. Jo, J. H. Cho, J. A. Rogers, J.-H. Ahn, *Nano Lett.* **2013**, *13*, 5600; b) P. Feng, I. Mönch, G. Huang, S. Harazim, E. J. Smith, Y. Mei, O. G. Schmidt, *Adv. Mater.* **2010**, *22*, 3667.

[18] a) R. Pan, Q. Guo, G. Li, E. Song, G. Huang, Z. An, Z. Di, Y. Mei, *ACS Appl. Mater. Interfaces* **2018**, *10*, 41497; b) A. K. Katiyar, A. A. Davidson, H. Jang, Y. Hwangbo, B. Han, S. Lee, Y. Hagiwara, T. Shimada, H. Hirakata, T. Kitamura, J. H. Ahn, *Nanoscale* **2019**, *11*, 15184; c) J. A. Rogers, M. G. Lagally, R. G. Nuzzo, *Nature* **2011**, *477*, 45.

[19] B. Hu, D. Xu, Y. Shao, Z. Nie, P. Liu, J. Li, L. Zhou, P. Wang, N. Huang, J. Liu, Y. Lu, Z. Wu, B. Wang, Y. Mei, M. Han, R. Li, E. Song, *Sci. Adv.* **2024**, *10*, adp8804.

[20] a) M. Sang, K. Kang, Y. Zhang, H. Zhang, K. Kim, M. Cho, J. Shin, J. H. Hong, T. Kim, S. K. Lee, W. H. Yeo, J. W. Lee, T. Lee, B. Xu, K. J. Yu, *Adv. Mater.* **2021**, *34*, 2105865; b) C. Chen, C. Li, S. W. Min, Q. S. Guo, Z. Y. Xia, D. Liu, Z. Q. Ma, F. N. Xia, *Nano Lett.* **2021**, *21*, 8385.

[21] Z. Zhang, T. Cai, Z. Li, B. Wu, Z. Zheng, C. You, G. Jiang, M. Ma, Z. Xu, C. Shen, X. Z. Chen, E. Song, J. Cui, G. Huang, Y. Mei, *Adv. Mater.* **2025**, *37*, 2413771.

[22] a) J. Shin, Z. H. Liu, W. B. Bai, Y. H. Liu, Y. Yan, Y. G. Xue, I. Kandela, M. Pezhouh, M. R. MacEwan, Y. G. Huang, W. Z. Ray, W. D. Zhou, J. A. Rogers, *Sci. Adv.* **2019**, *5*, aaw1899; b) Z. Rao, Y. Lu, Z. Li, K. Sim, Z. Ma, J. Xiao, C. Yu, *Nat. Electron.* **2021**, *4*, 513; c) C. You, X. Li, Y. Hu, N. Huang, Y. Wang, B. Wu, G. Jiang, J. Huang, Z. Zhang, B. Chen, Y. Wu, J. Liu, X. Chen, E. Song, J. Cui, P. Zhou, Z. Di, Z. An, G. Huang, Y. Mei, *Proc. Natl. Acad. Sci. U.S.A.* **2024**, *121*, 2403950121.

[23] H. C. Yuan, Z. Q. Ma, *Appl. Phys. Lett.* **2006**, *89*, 212105.

[24] S. Kim, J. Wu, A. Carlson, S. H. Jin, A. Kovalsky, P. Glass, Z. Liu, N. Ahmed, S. L. Elgan, W. Chen, P. M. Ferreira, M. Sitti, Y. Huang, J. A. Rogers, *Proc. Natl. Acad. Sci. U.S.A.* **2010**, *107*, 17095.

[25] E. Song, C. H. Chiang, R. Li, X. Jin, J. Zhao, M. Hill, Y. Xia, L. Li, Y. Huang, S. M. Won, K. J. Yu, X. Sheng, H. Fang, M. A. Alam, Y. Huang, J. Viventi, J. K. Chang, J. A. Rogers, *Proc. Natl. Acad. Sci. U.S.A.* **2019**, *116*, 15398.

[26] G. J. Li, Z. Ma, C. Y. You, G. S. Huang, E. M. Song, R. B. Pan, H. Zhu, J. Q. Xin, B. R. Xu, T. Lee, Z. H. An, Z. F. Di, Y. F. Mei, *Sci. Adv.* **2020**, *6*, aaz6511.

[27] Q. Guo, Y. Fang, M. Zhang, G. Huang, P. K. Chu, Y. Mei, Z. Di, X. Wang, *IEEE Trans. Electron. Dev.* **2017**, *64*, 1985.

[28] A. M. Clausen, D. M. Paskiewicz, A. Sadeghirad, J. Jakes, D. E. Savage, D. S. Stone, F. Liu, M. G. Lagally, *Extreme Mech. Lett.* **2014**, *1*, 9.

[29] H. Zhao, Y. Kim, H. Wang, X. Ning, C. Xu, J. Suh, M. Han, G. J. Pagan-Diaz, W. Lu, H. Li, W. Bai, O. Aydin, Y. Park, J. Wang, Y. Yao, Y. He, M. T. A. Saif, Y. Huang, R. Bashir, J. A. Rogers, *Proc. Natl. Acad. Sci. U.S.A.* **2021**, *118*, 2100077118.

[30] A. K. Katiyar, B. J. Kim, G. Lee, Y. Kim, J. S. Kim, J. M. Kim, S. Nam, J. Lee, H. Kim, J. H. Ahn, *Sci. Adv.* **2024**, *10*, adg7200.

[31] B. H. Kim, J. Lee, S. M. Won, Z. Q. Xie, J. K. Chang, Y. Yu, Y. K. Cho, H. Jang, J. Y. Jeong, Y. Lee, A. Ryu, D. H. Kim, K. H. Lee, J. Y. Lee, F. Lu, X. J. Wang, Q. Z. Huo, S. Min, D. Wu, B. W. Ji, A. Banks, J. Kim, N. Oh, H. M. Jin, S. Han, D. Kang, C. H. Lee, Y. M. Song, Y. H. Zhang, Y. G. Huang, et al., *ACS Nano* **2018**, *12*, 4164.

[32] X. Cheng, Z. Fan, S. Yao, T. Jin, Z. Lv, Y. Lan, R. Bo, Y. Chen, F. Zhang, Z. Shen, H. Wan, Y. Huang, Y. Zhang, *Science* **2023**, *379*, 1225.

 © 2025 Wiley-VCH GmbH

16163028, 2025, 35, Downloaded from https://advanced.onlinelibrary.wiley.com/doi/10.1002/adfm.202502191 by Fudan University, Wiley Online Library on [08/03/2026]. See the Terms and Conditions (https://onlinelibrary.wiley.com/terms-and-conditions) on Wiley Online Library for rules of use; OA articles are governed by the applicable Creative Commons License

[33] M. Huang, C. Boone, M. Roberts, D. E. Savage, M. G. Lagally, N. Shaji, H. Qin, R. Blick, J. A. Nairn, F. Liu, *Adv. Mater.* **2005**, *17*, 2860.
[34] R. Songmuang, A. Rastelli, S. Mendach, C. Deneke, O. G. Schmidt, *Microelectron. Eng.* **2007**, *84*, 1427.
[35] X. Guo, H. Li, B. Yeop Ahn, E. B. Duoss, K. J. Hsia, J. A. Lewis, R. G. Nuzzo, *Proc. Natl. Acad. Sci. U.S. A.* **2009**, *106*, 20149.
[36] S. Huang, L. Liu, Y. Zheng, Y. Wang, D. Kong, Y. Zhang, Y. Shi, L. Zhang, O. G. Schmidt, H. Y. Yang, *Adv. Mater.* **2018**, *30*, 1706637.
[37] a) Z. Mu, M. Zhang, Z. Xue, G. Sun, Q. Guo, D. Chen, G. Huang, Y. Mei, P. K. Chu, Z. Di, X. Wang, *Appl. Phys. Lett.* **2015**, *106*, 174102; b) W. Peng, M. Roberts, E. Nordberg, F. Flack, P. Colavita, R. Hamers, D. Savage, M. Lagally, M. Eriksson, *ECS Trans.* **2007**, *6*, 333.
[38] C. Qu, Q. Guo, X. Wu, C. You, B. Wu, Z. Zhang, Y. Mei, *Mater. Today Phys.* **2023**, *35*, 101090.
[39] M. M. Roberts, L. J. Klein, D. E. Savage, K. A. Slinker, M. Friesen, G. Celler, M. A. Eriksson, M. G. Lagally, *Nat. Mater.* **2006**, *5*, 388.
[40] X. Feng, M. A. Meitl, A. M. Bowen, Y. Huang, R. G. Nuzzo, J. A. Rogers, *Langmuir* **2007**, *23*, 12555.
[41] a) H. Yi, M. Seong, K. Sun, I. Hwang, K. Lee, C. Cha, T. i. Kim, H. E. Jeong, *Adv. Funct. Mater.* **2018**, *28*, 1706498; b) S. Qiao, N. Lu, *Extreme Mech. Lett.* **2016**, *7*, 136; c) D. S. Grierson, F. S. Flack, M. G. Lagally, K. T. Turner, *J. Appl. Phys.* **2016**, *120*, 093103.
[42] a) H. Fang, K. J. Yu, C. Gloschat, Z. Yang, E. Song, C.-H. Chiang, J. Zhao, S. M. Won, S. Xu, M. Trumpis, Y. Zhong, S. W. Han, Y. Xue, D. Xu, S. W. Choi, G. Cauwenberghs, M. Kay, Y. Huang, J. Viventi, I. R. Efimov, J. A. Rogers, *Nat. Biomed. Eng.* **2017**, *1*, 0038; b) W. Liu, Y. Liu, Z. Yang, C. Xu, X. Li, S. Huang, J. Shi, J. Du, A. Han, Y. Yang, *Nature* **2023**, *617*, 717.
[43] a) S. K. Kang, R. K. J. Murphy, S. W. Hwang, S. M. Lee, D. V. Harburg, N. A. Krueger, J. H. Shin, P. Gamble, H. Y. Cheng, S. Yu, Z. J. Liu, J. G. McCall, M. Stephen, H. Z. Ying, J. Kim, G. Park, R. C. Webb, C. H. Lee, S. J. Chung, D. S. Wie, A. D. Gujar, B. Vemulapalli, A. H. Kim, K. M. Lee, J. J. Cheng, Y. G. Huang, S. H. Lee, P. V. Braun, W. Z. Ray, J. A. Rogers, *Nature* **2016**, *530*, 71; b) C. Liu, Z. Wang, Y. Zhang, H. Lü, Y.-M. Zhang, *Adv. Mater. Interfaces* **2022**, *9*, 2201477.
[44] A. K. Katiyar, K. Y. Thai, W. S. Yun, J. Lee, J.-H. Ahn, *Sci. Adv.* **2020**, *6*, abb0576.
[45] a) J. A. Fan, W.-H. Yeo, Y. Su, Y. Hattori, W. Lee, S.-Y. Jung, Y. Zhang, Z. Liu, H. Cheng, L. Falgout, M. Bajema, T. Coleman, D. Gregoire, R. J. Larsen, Y. Huang, J. A. Rogers, *Nat. Commun.* **2014**, *5*, 3266; b) W. Peng, M. M. Roberts, E. P. Nordberg, F. S. Flack, P. E. Colavita, R. J. Hamers, D. E. Savage, M. G. Lagally, M. A. Eriksson, *Appl. Phys. Lett.* **2007**, *90*, 183107; c) J. Maire, E. Chávez-Ángel, G. Arregui, M. F. Colombano, N. E. Capuj, A. Griol, A. Martínez, D. Navarro-Urrios, J. Ahopelto, C. M. Sotomayor-Torres, *Adv. Funct. Mater.* **2021**, 2105767.
[46] a) P. Cendula, S. Kiravittaya, Y. F. Mei, C. Deneke, O. G. Schmidt, *Phys. Rev. B* **2009**, *79*, 085429; b) H. Qin, N. Shaji, N. E. Merrill, H. S. Kim, R. C. Toonen, R. H. Blick, M. M. Roberts, D. E. Savage, M. G. Lagally, G. Celler, *New J. Phys.* **2005**, *7*, 241; c) L. D. Landau, E. M. Lifshitz, R. Atkin, N. Fox, in *Physics of Continuous Media*, CRC Press, Boca Raton, FL **2020**.
[47] a) S. Xu, Z. Yan, K.-I. Jang, W. Huang, H. Fu, J. Kim, Z. Wei, M. Flavin, J. McCracken, R. Wang, A. Badea, Y. Liu, D. Xiao, G. Zhou, J. Lee, H. U. Chung, H. Cheng, W. Ren, A. Banks, X. Li, U. Paik, R. G. Nuzzo, Y. Huang, Y. Zhang, J. A. Rogers, *Science* **2015**, *347*, 154; b) Z. Song, C. Lv, M. Liang, V. Sanphuang, K. Wu, B. Chen, Z. Zhao, J. Bai, X. Wang, J. L. Volakis, L. Wang, X. He, Y. Yao, S. Tongay, H. Jiang, *Small* **2016**, *12*, 5401.
[48] D. Y. Khang, H. Q. Jiang, Y. Huang, J. A. Rogers, *Science* **2006**, *311*, 208.
[49] a) G. P. Nikishkov, *J. Appl. Phys.* **2003**, *94*, 5333; b) S. Timoshenko, *J. Opt. Soc. Am.* **1925**, *11*, 233; c) G. Li, M. Yarali, A. Cocemasov, S. Baunack, D. L. Nika, V. M. Fomin, S. Singh, T. Gemming, F. Zhu, A. Mavrokefalos, O. G. Schmidt, *ACS Nano* **2017**, *11*, 8215; d) R. Songmuang, C. Deneke, O. G. Schmidt, *Appl. Phys. Lett.* **2006**, *89*, 223109.
[50] Z. Zhang, B. Wu, Y. Wang, T. Cai, M. Ma, C. You, C. Liu, G. Jiang, Y. Hu, X. Li, X.-Z. Chen, E. Song, J. Cui, G. Huang, S. Kiravittaya, Y. Mei, *Nat. Commun.* **2024**, *15*, 3066.
[51] D. Grimm, R. B. Wilson, B. Teshome, S. Gorantla, M. H. Rümmeli, T. Bublat, E. Zallo, G. Li, D. G. Cahill, O. G. Schmidt, *Nano Lett.* **2014**, *14*, 2387.
[52] G. J. Meyer, N. L. Dias, R. H. Blick, I. Knezevic, *IEEE Trans. Nanotechnol.* **2007**, *6*, 446.
[53] J.-T. Sun, Z. Wang, S. Meng, S. Du, F. Liu, H. J. Gao, *2D Mater.* **2016**, *3*, 035026.
[54] X. Y. Guo, H. Li, B. Y. Ahn, E. B. Duoss, K. J. Hsia, J. A. Lewis, R. G. Nuzzo, *Proc. Nat. Acad. Sci U.S.A.* **2009**, *106*, 20149;
[55] H. Jang, T. Das, W. Lee, J.-H. Ahn, in *Silicon Nanomembranes: Fundamental Science and Applications*, Wiley-VCH, Weinheim, Germany **2016**.
[56] P. Zhang, E. Tevaarwerk, B. N. Park, D. E. Savage, G. K. Celler, I. Knezevic, P. G. Evans, M. A. Eriksson, M. G. Lagally, *Nature* **2006**, *439*, 703.
[57] S. Lee, K. Kim, K. P. Dhakal, H. Kim, W. S. Yun, J. Lee, H. Cheong, J.-H. Ahn, *Nano Lett.* **2017**, *17*, 7744.
[58] S. Neogi, J. S. Reparaz, L. F. C. Pereira, B. Graczykowski, M. R. Wagner, M. Sledzinska, A. Shchepetov, M. Prunnila, J. Ahopelto, C. M. Sotomayor-Torres, D. Donadio, *ACS Nano* **2015**, *9*, 3820.
[59] H. C. Ko, A. J. Baca, J. A. Rogers, *Nano Lett.* **2006**, *6*, 2318.
[60] J. Y. Lee, J. Shin, K. Kim, J. E. Ju, A. Dutta, T. S. Kim, Y. U. Cho, T. Kim, L. Hu, W. K. Min, H. S. Jung, Y. S. Park, S. M. Won, W. H. Yeo, J. Moon, D. Y. Khang, H. J. Kim, J. H. Ahn, H. Cheng, K. J. Yu, J. A. Rogers, *Small* **2023**, *19*, 2302597.
[61] a) J. Yun, S. Varlamov, J. Huang, K. Kim, M. A. Green, *Appl. Phys. Lett.* **2014**, *104*, 242102; b) A. Michael, C. Y. Kwok, P. Wang, O. Kazuo, S. Varlamov, *J. Microelectromech. Syst.* **2015**, *24*, 1951.
[62] J. Zhu, C. Liu, R. Gao, Y. Zhang, H. Zhang, S. Cheng, D. Liu, J. Wang, Q. Liu, Z. Wang, X. Wang, Y. Jin, M. Zhang, *Adv. Mater.* **2025**, *37*, 2413404.
[63] H. J. Chung, T. i. Kim, H. S. Kim, S. A. Wells, S. Jo, N. Ahmed, Y. H. Jung, S. M. Won, C. A. Bower, J. A. Rogers, *Adv. Funct. Mater.* **2011**, *21*, 3029.
[64] a) S. Surdo, G. Barillaro, *Small* **2024**, *20*, 2400499; b) J. D. Kim, M. Kim, L. Kong, P. K. Mohseni, S. Ranganathan, J. Pachamuthu, W. K. Chim, S. Y. Chiam, J. J. Coleman, X. Li, *ACS Appl. Mater. Interfaces* **2018**, *10*, 9116.
[65] a) M. Cho, I. Cho, K. Kim, I. Park, *Adv. Mater. Technol.* **2021**, *6*, 2000847; b) G.-J. Ko, S. D. Han, J.-K. Kim, J. Zhu, W. B. Han, J. Chung, S. M. Yang, H. Cheng, D.-H. Kim, C.-Y. Kang, S.-W. Hwang, *NPG Asia Mater.* **2020**, *12*, 71.
[66] H. C. Yuan, G. K. Celler, Z. Q. Ma, *J. Appl. Phys.* **2007**, *102*, 034501.
[67] S. M. Lee, R. Biswas, W. G. Li, D. Kang, L. Chan, J. Yoon, *ACS Nano* **2014**, *8*, 10507.
[68] S. M. Yang, J. H. Shim, H. U. Cho, T. M. Jang, G. J. Ko, J. Shim, T. H. Kim, J. Zhu, S. Park, Y. S. Kim, S. Y. Joung, J. C. Choe, J. W. Shin, J. H. Lee, Y. M. Kang, H. Cheng, Y. Jung, C. H. Lee, D. P. Jang, S. W. Hwang, *Adv. Mater.* **2022**, *34*, 2108203.
[69] a) Q. Qiao, H. Sun, X. Liu, B. Dong, J. Xia, C. Lee, G. Zhou, *Micromachines* **2021**, *12*, 1311; b) R. Guo, Q. Lang, Z. Zhang, H. Hu, T. Liu, J. Wang, Z. Cheng, *Chip* **2024**, *3*, 100104.
[70] a) G. S. Huang, S. Kiravittaya, V. A. Bolaños Quiñones, F. Ding, M. Benyoucef, A. Rastelli, Y. F. Mei, O. G. Schmidt, *Appl. Phys. Lett.* **2009**, *94*, 141901; b) X. Lin, Y. Fang, L. Zhu, J. Zhang, G. Huang, J. Wang, Y. Mei, *Adv. Opt. Mater.* **2016**, *4*, 936.
[71] C. Chiappini, E. De Rosa, J. O. Martinez, X. Liu, J. Steele, M. M. Stevens, E. Tasciotti, *Nat. Mater.* **2015**, *14*, 532.

© 2025 Wiley-VCH GmbH

16163028, 2025, 35, Downloaded from https://advanced.onlinelibrary.wiley.com/doi/10.1002/adfm.202502191 by Fudan University, Wiley Online Library on [08/03/2026]. See the Terms and Conditions (https://onlinelibrary.wiley.com/terms-and-conditions) on Wiley Online Library for rules of use; OA articles are governed by the applicable Creative Commons License

[72] a) K. Li, S. Ali, M. Wojcik, V. De Andrade, X. Huang, H. Yan, Y. S. Chu, E. Nazaretski, A. Pattammattel, C. Jacobsen, *Optica* **2020**, *7*, 410; b) H. Ohlin, T. Frisk, I. Sychugov, U. Vogt, *Micro Nano Eng* **2023**, *19*, 100178.
[73] a) H. Lin, F. Wu, P. Gao, W. Shen, *ACS Appl. Energy Mater.* **2019**, *2*, 5871; b) F. Wu, H. Lin, Z. Yang, M. Liao, Z. Wang, Z. Li, P. Gao, J. Ye, W. Shen, *Nano Energy* **2019**, *58*, 817.
[74] N. Geyer, B. Fuhrmann, Z. Huang, J. de Boor, H. S. Leipner, P. Werner, *J. Phys. Chem. C* **2012**, *116*, 13446.
[75] Q. Guo, M. Zhang, Z. Xue, L. Ye, G. Wang, G. Huang, Y. Mei, X. Wang, Z. Di, *Appl. Phys. Lett.* **2013**, *103*, 264102.
[76] Z. Zheng, C. Liu, W. He, J. Huang, J. He, G. Huang, Y. Mei, C. Zheng, *Appl. Phys. Lett.* **2024**, *124*, 101903.
[77] a) E. Cerda, L. Mahadevan, *Phys. Rev. Lett.* **2003**, *90*, 074302; b) S. P. Timoshenko, J. M. Gere, *Theory of elastic stability*, Courier Corporation, Mineola, New York, USA **2012**.
[78] Z. Y. Huang, W. Hong, Z. Suo, *J. Mech. Phys. Solids* **2005**, *53*, 2101.
[79] S. V. Golod, V. Y. Prinz, P. Wägli, L. Zhang, O. Kirfel, E. Deckhardt, F. Glaus, C. David, D. Grützmacher, *Appl. Phys. Lett.* **2004**, *84*, 3391.
[80] C. Chen, P. Song, F. Meng, P. Ou, X. Liu, J. Song, *Appl. Phys. Lett.* **2018**, *113*, 112104.
[81] P. Cendula, S. Kiravittaya, I. Monch, J. Schumann, O. G. Schmidt, *Nano Lett.* **2011**, *11*, 236.
[82] C.-H. Hsueh, *J. Appl. Phys.* **2002**, *91*, 9652.
[83] Y. Liu, X. Wang, Y. Xu, Z. Xue, Y. Zhang, X. Ning, X. Cheng, Y. Xue, D. Lu, Q. Zhang, F. Zhang, J. Liu, X. Guo, K. C. Hwang, Y. Huang, J. A. Rogers, Y. Zhang, *Proc. Natl. Acad. Sci. U.S.A.* **2019**, *116*, 15368.
[84] a) W. Huang, S. Koric, X. Yu, K. J. Hsia, X. Li, *Nano Lett.* **2014**, *14*, 6293; b) I. S. Chun, A. Challa, B. Derickson, K. J. Hsia, X. Li, *Nano Lett.* **2010**, *10*, 3927; c) S. Alben, B. Balakrisnan, E. Smela, *Nano Lett.* **2011**, *11*, 2280; d) C. Chen, P. Song, F. Meng, P. Ou, X. Liu, J. Song, *Nanotechnology* **2018**, *29*, 345301.
[85] a) F. Ericson, J. Å. Schweitz, *J. Appl. Phys.* **1990**, *68*, 5840; b) J. Camassel, L. A. Falkovsky, N. Planes, *Phys. Rev. B* **2000**, *63*, 035309.
[86] a) M. V. Fischetti, Z. Ren, P. M. Solomon, M. Yang, K. Rim, *J. Appl. Phys.* **2003**, *94*, 1079; b) M. V. Fischetti, F. Gamiz, W. Hänsch, *J. Appl. Phys.* **2002**, *92*, 7320; c) T. Sato, Y. Takeishi, H. Hara, Y. Okamoto, *Phys. Rev. B* **1971**, *4*, 1950.
[87] a) S. Nakashima, T. Mitani, M. Ninomiya, K. Matsumoto, *J. Appl. Phys.* **2006**, *99*, 053512; b) L. H. Wong, C. C. Wong, J. P. Liu, D. K. Sohn, L. Chan, L. C. Hsia, H. Zang, Z. H. Ni, Z. X. Shen, *Jpn. J. Appl. Phys.* **2005**, *44*, 7922.
[88] a) Q. Guo, M. Zhang, Z. Xue, J. Zhang, G. Wang, D. Chen, Z. Mu, G. Huang, Y. Mei, Z. Di, X. Wang, *AIP Adv.* **2015**, *5*, 037115; b) M. A. Ochoa, Y. S. Li, *Solid State Commun.* **2021**, *325*, 114154.
[89] a) M. Erdtmann, T. A. Langdo, *J. Mater. Sci. Mater. Electron.* **2006**, *17*, 137; b) A. Ogura, D. Kosemura, K. Yamasaki, S. Tanaka, Y. Kakemura, A. Kitano, I. Hirosawa, *Solid State Electron.* **2007**, *51*, 219.
[90] a) P. F. Fewster, *Crit. Rev. Solid State Mater. Sci.* **1997**, *22*, 69; b) E. Mukhamedzhanov, M. Kummer, A. Dommann, *J. Phys. D: Appl. Phys.* **2000**, *33*, 2087.
[91] a) C. F. Huang, Y. J. Yang, C. Y. Peng, F. Yuan, C. W. Liu, *Appl. Phys. Lett.* **2006**, *89*, 103502; b) N. M. p Johnson, F. A. Ponce, R. A. Street, R. J. Nemanich, *Phys. Rev. B* **1987**, *35*, 4166.
[92] a) Z. Wang, X. Zhang, J. Wu, L. Liang, X. Niu, Q. Chen, R. Li, J. Luo, *Adv. Opt. Mater.* **2023**, *11*, 2202383; b) L. Li, J. Wang, L. Kang, W. Liu, L. Yu, B. Zheng, M. L. Brongersma, D. H. Werner, S. Lan, Y. Shi, Y. Xu, X. Wang, *ACS Nano* **2020**, *14*, 16634; c) R. Li, C. Zhang, X. Li, *Appl. Phys. Lett.* **2017**, *110*, 013902.
[93] a) M. Cho, J.-H. Seo, D. Zhao, J. Lee, K. Xiong, X. Yin, Y. Liu, S.-C. Liu, M. Kim, T. J. Kim, X. Wang, W. Zhou, Z. Ma, *J. Vac. Sci. Technol. B* **2016**, *34*, 040601; b) S. Lim, D.-S. Um, M. Ha, Q. Zhang, Y. Lee, Y. Lin, Z. Fan, H. Ko, *Nano Res.* **2017**, *10*, 22.
[94] J. H. Seo, K. Zhang, M. Kim, D. Y. Zhao, H. J. Yang, W. D. Zhou, Z. Q. Ma, *Adv. Opt. Mater.* **2016**, *4*, 120.
[95] K. Zhang, Y. H. Jung, S. Mikael, J.-H. Seo, M. Kim, H. Mi, H. Zhou, Z. Xia, W. Zhou, S. Gong, Z. Ma, *Nat. Commun.* **2017**, *8*, 1782.
[96] W. Peng, S. Sampat, S. M. Rupich, B. Anand, H. M. Nguyen, D. Taylor, B. E. Beardon, Y. N. Gartstein, Y. J. Chabal, A. V. Malko, *Nanoscale* **2015**, *7*, 8524.
[97] Y. Wang, L. Yin, S. Huang, R. Xiao, Y. Zhang, D. Li, X. Pi, D. Yang, *Nano Lett.* **2023**, *23*, 8460.
[98] R. Pan, Q. Guo, J. Cao, G. Huang, Y. Wang, Y. Qin, Z. Tian, Z. An, Z. Di, Y. Mei, *Nanoscale* **2019**, *11*, 16844.
[99] E. M. Song, Q. L. Guo, G. S. Huang, B. Jia, Y. F. Mei, *ACS Appl. Mater. Interfaces* **2017**, *9*, 12171.
[100] a) X. Zhou, Z. Tian, H. J. Kim, Y. Wang, B. Xu, R. Pan, Y. J. Chang, Z. Di, P. Zhou, Y. Mei, *Small* **2019**, *15*, 1902528; b) H. Wang, H. Zhen, S. Li, Y. Jing, G. Huang, Y. Mei, W. Lu, *Sci. Adv.* **2016**, *2*, 1600027.
[101] a) T. Deng, Z. Zhang, Y. Liu, Y. Wang, F. Su, S. Li, Y. Zhang, H. Li, H. Chen, Z. Zhao, Y. Li, Z. Liu, *Nano Lett.* **2019**, *19*, 1494; b) J. Xu, Q. Wang, M. Shen, Y. Yang, H. Liu, X. Yuan, Y. Zhang, K. Liu, S. Cai, Y. Huang, X. Ren, *ACS Nano* **2024**, *18*, 14978.
[102] a) M. Cho, J.-H. Seo, J. Lee, D. Zhao, H. Mi, X. Yin, M. Kim, X. Wang, W. Zhou, Z. Ma, *Appl. Phys. Lett.* **2015**, *106*, 181107; b) Z. Xia, H. Song, M. Kim, M. Zhou, T.-H. Chang, D. Liu, X. Yin, K. Xiong, H. Mi, X. Wang, F. Xia, Z. Yu, Z. Ma, Q. Gan, *Sci. Adv.* **2017**, *3*, 1602783.
[103] A. Varpula, K. Grigoras, K. Tappura, A. V. Timofeev, A. Shchepetov, J. Hassel, J. Ahopelto, M. Prunnila, *Proceedings* **2018**, *2*, 894.
[104] G. A. Rodriguez, P. Markov, A. P. Cartwright, M. H. Choudhury, F. O. Afzal, T. Cao, S. I. Halimi, S. T. Retterer, I. I. Kravchenko, S. M. Weiss, *Opt. Express* **2019**, *27*, 9536.
[105] X. Liu, R. Guo, S. Zhang, Z. Zhang, J. Wang, T. Liu, Z. Cheng, *Appl. Phys. Lett.* **2024**, *125*, 111102.
[106] G. Pennelli, E. Dimaggio, M. Macucci, *IEEE Trans. Nanotechnol.* **2018**, *17*, 500.
[107] a) X. Xu, H. Subbaraman, D. T. Pham, A. Hosseini, A. Ghaffari, R. T. Chen, *J. Phys.: Conf. Ser.* **2011**, *276*, 012096; b) H. Yang, D. Zhao, S. Liu, Y. Liu, J.-H. Seo, Z. Ma, W. Zhou, *Photonics* **2015**, *2*, 1081.
[108] W. Q. Wei, A. He, B. Yang, Z. H. Wang, J. Z. Huang, D. Han, M. Ming, X. Guo, Y. Su, J. J. Zhang, T. Wang, *Light. Sci. Appl.* **2023**, *12*, 84.
[109] a) M. Cho, J. Yun, D. Kwon, K. Kim, I. Park, *ACS Appl. Mater. Interfaces* **2018**, *10*, 12870; b) L. Wang, Y. Gao, F. Dai, D. Kong, H. Wang, P. Sun, Z. Shi, X. Sheng, B. Xu, L. Yin, *ACS Appl. Mater. Interfaces* **2019**, *11*, 18013; c) Y. Minrui, H. Minghuang, D. E. Savage, M. G. Lagally, R. H. Blick, *IEEE Trans. Nanotechnol.* **2011**, *10*, 21; d) J. Park, R. Blick, *Sensors* **2016**, *16*, 200.
[110] a) H. S. Kim, S. M. Yang, T. M. Jang, N. Oh, H. S. Kim, S. W. Hwang, *Adv. Healthcare Mater.* **2018**, *7*, 1801071; b) K. M. McElhinny, G. Gopalakrishnan, D. E. Savage, J. C. Silva-Martínez, M. G. Lagally, M. V. Holt, P. G. Evans, *J. Phys. D: Appl. Phys.* **2015**, *48*, 015306; c) W.-C. Lai, S. Chakravarty, Y. Zou, R. T. Chen, *Opt. Lett.* **2012**, *37*, 1208.
[111] Y. Chen, Q. L. Guo, G. S. Huang, G. J. Li, L. Wang, Z. Tian, Y. Z. Qin, Z. F. Di, Y. F. Mei, *ACS Appl. Mater. Interfaces* **2018**, *10*, 25644.
[112] S. Chen, Y. Dong, T. L. Liu, J. Li, *Biosens. Bioelectron.* **2022**, *195*, 113683.
[113] Y. Dong, S. Chen, T. L. Liu, J. Li, *Small* **2022**, *18*, 2106866.
[114] F. Teng, Q. Zhu, Y. Wang, J. Du, N. Lu, *Talanta* **2018**, *179*, 583.
[115] G. Li, Z. Ma, C. You, G. Huang, E. Song, R. Pan, H. Zhu, J. Xin, B. Xu, T. Lee, Z. An, Z. Di, Y. Mei, *Sci. Adv.* **2020**, *6*, aaz6511.
[116] H. C. Shin, D. Deterra, J. Park, H. Kim, M. Nishikiori, C. Uetrecht, P. G. Ahlquist, M. Arbulu, R. H. Blick, *J. Proteomics* **2018**, *175*, 5.
[117] K. Xiao, H. Wang, H. Xie, S. Li, Z. Zhao, Z. Cui, Q. Chen, P. Zhou, F. Liu, Y. Xu, Y. L. Jiang, J. Wan, *IEEE Trans. Instrum. Meas.* **2024**, *73*, 1.
[118] R. Guo, Q. He, Z. Zhang, Y. Xu, S. Zhang, Q. Lang, S. Xiao, P. Han, J. Wang, T. Ding, T. Liu, H. K. Tsang, K. Goda, Z. Cheng, *Appl. Phys. Rev.* **2024**, *11*, 021417.

 © 2025 Wiley-VCH GmbH

16163028, 2025, 35, Downloaded from https://advanced.onlinelibrary.wiley.com/doi/10.1002/adfm.202502191 by Fudan University, Wiley Online Library on [08/03/2026]. See the Terms and Conditions (https://onlinelibrary.wiley.com/terms-and-conditions) on Wiley Online Library for rules of use; OA articles are governed by the applicable Creative Commons License

[119] J. Viventi, D.-H. Kim, L. Vigeland, E. S. Frechette, J. A. Blanco, Y.-S. Kim, A. E. Avrin, V. R. Tiruvadi, S.-W. Hwang, A. C. Vanleer, D. F. Wulsin, K. Davis, C. E. Gelber, L. Palmer, J. Van der Spiegel, J. Wu, J. Xiao, Y. Huang, D. Contreras, J. A. Rogers, B. Litt, *Nat. Neurosci.* **2011**, *14*, 1599.
[120] a) D. Hudecz, T. Khire, H. L. Chung, L. Adumeau, D. Glavin, E. Luke, M. S. Nielsen, K. A. Dawson, J. L. McGrath, Y. Yan, *ACS Nano* **2020**, *14*, 1111; b) A. Prominski, P. Li, B. A. Miao, B. Tian, *Acc. Mater. Res.* **2021**, *2*, 895; c) M. Yu, Y. Huang, J. Ballweg, H. Shin, M. Huang, D. E. Savage, M. G. Lagally, E. W. Dent, R. H. Blick, J. C. Williams, *ACS Nano* **2011**, *5*, 2447.
[121] K. Kwon, J. U. Kim, S. M. Won, J. Z. Zhao, R. Avila, H. L. Wang, K. S. Chun, H. Jang, K. H. Lee, J. H. Kim, S. Yoo, Y. J. Kang, J. Kim, J. Lim, Y. Park, W. Lu, T. I. Kim, A. Banks, Y. G. Huang, J. A. Rogers, *Nat. Biomed. Eng.* **2023**, *7*, 1215.
[122] S. Y. Huang, B. C. Zhang, Z. B. Shao, L. He, Q. Zhang, J. S. Jie, X. H. Zhang, *Nano Lett.* **2020**, *20*, 2478.
[123] Q. S. Yang, S. Lee, Y. G. Xue, Y. Yan, T. L. Liu, S. K. Kang, Y. J. Lee, S. H. Lee, M. H. Seo, D. Lu, J. Koo, M. R. MacEwan, R. S. T. Yin, W. Z. Ray, Y. G. Huang, J. A. Rogers, *Adv. Funct. Mater.* **2020**, *30*, 1910718.
[124] N. Abdul, M. N. Rush, J. Nohava, U. Amezcua, A. P. Shreve, F. Cavallo, *ACS Appl. Mater. Interfaces* **2020**, *12*, 10697.
[125] W. Bai, J. Shin, R. Fu, I. Kandela, D. Lu, X. Ni, Y. Park, Z. Liu, T. Hang, D. Wu, Y. Liu, C. R. Haney, I. Stepien, Q. Yang, J. Zhao, K. R. Nandoliya, H. Zhang, X. Sheng, L. Yin, K. MacRenaris, A. Brikha, F. Aird, M. Pezhouh, J. Hornick, W. Zhou, J. A. Rogers, *Nat. Biomed. Eng.* **2019**, *3*, 644.
[126] X. Huang, Y. Liu, G. W. Kong, J. H. Seo, Y. Ma, K.-I. Jang, J. A. Fan, S. Mao, Q. Chen, D. Li, H. Liu, C. Wang, D. Patnaik, L. Tian, G. A. Salvatore, X. Feng, Z. Ma, Y. Huang, J. A. Rogers, *Microsyst. Nanoeng.* **2016**, *2*, 16052.
[127] J. Kim, M. Lee, H. J. Shim, R. Ghaffari, H. R. Cho, D. Son, Y. H. Jung, M. Soh, C. Choi, S. Jung, K. Chu, D. Jeon, S. T. Lee, J. H. Kim, S. H. Choi, T. Hyeon, D. H. Kim, *Nat. Commun.* **2014**, *5*, 5747.
[128] D. Meng, H. Zhao, X. Wu, M. Liu, Q. Guo, *IEEE Electron. Device Lett.* **2024**, *45*, 2518.
[129] a) G. Li, E. Song, G. Huang, Q. Guo, F. Ma, B. Zhou, Y. Mei, *Adv. Funct. Mater.* **2018**, *28*, 1801448; b) G. Li, E. Song, G. Huang, R. Pan, Q. Guo, F. Ma, B. Zhou, Z. Di, Y. Mei, *Small* **2018**, *14*, 1802985; c) S. W. Hwang, C. H. Lee, H. Y. Cheng, J. W. Jeong, S. K. Kang, J. H. Kim, J. Shin, J. Yang, Z. J. Liu, G. A. Ameer, Y. G. Huang, J. A. Rogers, *Nano Lett.* **2015**, *15*, 2801.
[130] a) Y. Chen, H. Wang, Y. Zhang, R. Li, C. Chen, H. Zhang, S. Tang, S. Liu, X. Chen, H. Wu, R. Lv, X. Sheng, P. Zhang, S. Wang, L. Yin, *Nanotechnology* **2019**, *30*, 394002; b) H. L. Hernandez, S. K. Kang, O. P. Lee, S. W. Hwang, J. A. Kaitz, B. Inci, C. W. Park, S. Chung, N. R. Sottos, J. S. Moore, J. A. Rogers, S. R. White, *Adv. Mater.* **2014**, *26*, 7637; c) S.-K. Kang, S.-W. Hwang, S. Yu, J.-H. Seo, E. A. Corbin, J. Shin, D. S. Wie, R. Bashir, Z. Ma, J. A. Rogers, *Adv. Funct. Mater.* **2015**, *25*, 1789; d) J. Koo, M. R. MacEwan, S. K. Kang, S. M. Won, M. Stephen, P. Gamble, Z. Xie, Y. Yan, Y. Y. Chen, J. Shin, N. Birenbaum, S. Chung, S. B. Kim, J. Khalifeh, D. V. Harburg, K. Bean, M. Paskett, J. Kim, Z. S. Zohny, S. M. Lee, R. Zhang, K. Luo, B. Ji, A. Banks, H. M. Lee, Y. Huang, W. Z. Ray, J. A. Rogers, *Nat. Med.* **2018**, *24*, 1830.
[131] H. Fang, J. Zhao, K. J. Yu, E. Song, A. B. Farimani, C. H. Chiang, X. Jin, Y. Xue, D. Xu, W. Du, K. J. Seo, Y. Zhong, Z. Yang, S. M. Won, G. Fang, S. W. Choi, S. Chaudhuri, Y. Huang, M. A. Alam, J. Viventi, N. R. Aluru, J. A. Rogers, *Proc. Natl. Acad. Sci. U.S.A.* **2016**, *113*, 11682.
[132] M. A. Brenckle, H. Cheng, S. Hwang, H. Tao, M. Paquette, D. L. Kaplan, J. A. Rogers, Y. Huang, F. G. Omenetto, *ACS Appl. Mater. Interfaces* **2015**, *7*, 19870.
[133] J. Shin, Y. Yan, W. Bai, Y. Xue, P. Gamble, L. Tian, I. Kandela, C. R. Haney, W. Spees, Y. Lee, M. Choi, J. Ko, H. Ryu, J. K. Chang, M. Pezhouh, S. K. Kang, S. M. Won, K. J. Yu, J. Zhao, Y. K. Lee, M. R. MacEwan, S. K. Song, Y. Huang, W. Z. Ray, J. A. Rogers, *Nat. Biomed. Eng.* **2019**, *3*, 37.
[134] a) H. Li, C. Zhao, X. Wang, J. Meng, Y. Zou, S. Noreen, L. Zhao, Z. Liu, H. Ouyang, P. Tan, M. Yu, Y. Fan, Z. L. Wang, Z. Li, *Adv. Sci.* **2019**, *6*, 1801625; b) G. Lee, Y. S. Choi, H.-J. Yoon, J. A. Rogers, *Matter* **2020**, *3*, 1031.
[135] S. W. Hwang, H. Tao, D. H. Kim, H. Y. Cheng, J. K. Song, E. Rill, M. A. Brenckle, B. Panilaitis, S. M. Won, Y. S. Kim, Y. M. Song, K. J. Yu, A. Ameen, R. Li, Y. W. Su, M. M. Yang, D. L. Kaplan, M. R. Zakin, M. J. Slepian, Y. G. Huang, F. G. Omenetto, J. A. Rogers, *Science* **2012**, *337*, 1640.
[136] C. Dagdeviren, Y. Su, P. Joe, R. Yona, Y. Liu, Y.-S. Kim, Y. Huang, A. R. Damadoran, J. Xia, L. W. Martin, Y. Huang, J. A. Rogers, *Nat. Commun.* **2014**, *5*, 4496.
[137] J. Kim, D. Son, M. Lee, C. Song, J. K. Song, J. H. Koo, D. J. Lee, H. J. Shim, J. H. Kim, M. Lee, T. Hyeon, D. H. Kim, *Sci. Adv.* **2016**, *2*, 1501101.
[138] J. Kim, J. Park, Y. G. Park, E. Cha, M. Ku, H. S. An, K. P. Lee, M. I. Huh, J. Kim, T. S. Kim, D. W. Kim, H. K. Kim, J. U. Park, *Nat. Biomed. Eng.* **2021**, *5*, 772.
[139] D. Son, J. Lee, S. Qiao, R. Ghaffari, J. Kim, J. E. Lee, C. Song, S. J. Kim, D. J. Lee, S. W. Jun, S. Yang, M. Park, J. Shin, K. Do, M. Lee, K. Kang, C. S. Hwang, N. S. Lu, T. Hyeon, D. H. Kim, *Nat. Nanotechnol.* **2014**, *9*, 397.
[140] a) J. Deng, H. Ji, C. Yan, J. Zhang, W. Si, S. Baunack, S. Oswald, Y. Mei, O. G. Schmidt, *Angew. Chem., Int. Ed.* **2013**, *52*, 2326; b) X. Liu, J. Zhang, W. Si, L. Xi, B. Eichler, C. Yan, O. G. Schmidt, *ACS Nano* **2015**, *9*, 1198.
[141] S. Huang, L. Zhang, L. Liu, L. Liu, J. Li, H. Hu, J. Wang, F. Ding, O. G. Schmidt, *Energy Storage Mater.* **2018**, *12*, 23.
[142] S. H. Lee, C. K. Jeong, G.-T. Hwang, K. J. Lee, *Nano Energy* **2015**, *14*, 111.
[143] C. Yu, X. Li, T. Ma, J. Rong, R. Zhang, J. Shaffer, Y. An, Q. Liu, B. Wei, H. Jiang, *Adv. Energy Mater.* **2012**, *2*, 68.
[144] L. Y. Lu, Z. J. Yang, K. Meacham, C. Cvetkovic, E. A. Corbin, A. Vázquez-Guardado, M. T. Xue, L. Yin, J. Boroumand, G. Pakeltis, T. Sang, K. J. Yu, D. Chanda, R. Bashir, R. W. Gereau, X. Sheng, J. A. Rogers, *Adv. Energy Mater.* **2018**, *8*, 1703035.
[145] a) H. M. Nguyen, O. Seitz, W. Peng, Y. N. Gartstein, Y. J. Chabal, A. V. Malko, *ACS Nano* **2012**, *6*, 5574; b) R. Li, W. Yang, Z. Ma, W. Zhou, *2011 37th IEEE Photovoltaic Specialists Conference* **2011**; c) S. Hoang, A. Ashraf, M. D. Eisaman, D. Nykypanchuk, C. Y. Nam, *Nanoscale* **2016**, *8*, 5873.
[146] a) E. Aydin, T. G. Allen, M. De Bastiani, A. Razzaq, L. Xu, E. Ugur, J. Liu, S. De Wolf, *Science* **2024**, *383*, adh3849; b) Z. Zheng, J. Wang, P. Bi, J. Ren, Y. Wang, Y. Yang, X. Liu, S. Zhang, J. Hou, *Joule* **2022**, *6*, 171.
[147] a) X. Yang, B. Geng, J. Wei, Z. Wang, K. Lan, X. Ren, G. Qin, *J. Phys. D: Appl. Phys.* **2022**, *55*, 175105; b) J. Zhang, Y. Zhang, D. Chen, W. Zhu, H. Xi, J. Zhang, C. Zhang, Y. Hao, *Nanomaterials* **2018**, *8*, 1060; c) Y. Liu, L. Wang, L. Wang, X. Wu, Z. Hao, J. Yu, Y. Luo, C. Sun, Y. Han, B. Xiong, J. Wang, H. Li, *Semicond. Sci. Technol.* **2019**, *34*, 105023; d) G. Qin, Y. Zhang, K. Lan, L. Li, J. Ma, S. Yu, *ACS Appl. Mater. Interfaces* **2018**, *10*, 12798; e) T. Das, H. Jang, J. Bok Lee, H. Chu, S. Dae Kim, J.-H. Ahn, *2D Mater.* **2015**, *2*, 044006; f) M. Cho, J.-H. Seo, M. Kim, J. Lee, D. Liu, W. Zhou, Z. Yu, Z. Ma, *J. Vac. Sci. Technol. B* **2016**, *34*, 040604; g) H.-S. Kim, S. M. Won, Y.-G. Ha, J.-H. Ahn, A. Facchetti, T. J. Marks, J. A. Rogers, *Appl. Phys. Lett.* **2009**, *95*, 183504.
[148] E. Menard, R. G. Nuzzo, J. A. Rogers, *Appl. Phys. Lett.* **2005**, *86*, 093507.
[149] J. Zhang, W. Wang, J. Zhu, C. Wang, T. Zhu, C. Zhao, J. Wang, S. Zhang, X. Wang, K.-C. Chang, H. Meng, M. Chan, M. Zhang, *ACS Nano* **2024**, *18*, 3362.

© 2025 Wiley-VCH GmbH

16163028, 2025, 35, Downloaded from https://advanced.onlinelibrary.wiley.com/doi/10.1002/adfm.202502191 by Fudan University, Wiley Online Library on [08/03/2026]. See the Terms and Conditions (https://onlinelibrary.wiley.com/terms-and-conditions) on Wiley Online Library for rules of use; OA articles are governed by the applicable Creative Commons License

[150] a) L. Sun, G. Qin, J.-H. Seo, G. K. Celler, W. Zhou, Z. Ma, *Small* **2010**, *6*, 2553; b) H. C. Yuan, M. M. Kelly, D. E. Savage, M. G. Lagally, G. K. Celler, Z. Ma, *IEEE Trans. Electron. Dev.* **2008**, *55*, 810.
[151] T. I. Kim, Y. H. Jung, H. J. Chung, K. J. Yu, N. Ahmed, C. J. Corcoran, J. S. Park, S. H. Jin, J. A. Rogers, *Appl. Phys. Lett.* **2013**, *102*, 182104.
[152] a) J. Koo, C. Lee, C. R. Chu, S.-K. Kang, H. M. Lee, *Adv. Mater. Technol.* **2020**, *5*, 1900962; b) M. Liu, G. Huang, P. Feng, Q. Guo, F. Shao, Z. Tian, G. Li, Q. Wan, Y. Mei, *J. Semicond* **2017**, *38*, 064006.
[153] D. H. Kim, Y. S. Kim, J. Wu, Z. J. Liu, J. Z. Song, H. S. Kim, Y. G. Y. Huang, K. C. Hwang, J. A. Rogers, *Adv. Mater.* **2009**, *21*, 3703.
[154] T. Das, X. Chen, H. Jang, I.-K. Oh, H. Kim, J.-H. Ahn, *Small* **2016**, *12*, 5720.
[155] J. Biggs, J. Myers, J. Kufel, E. Ozer, S. Craske, A. Sou, C. Ramsdale, K. Williamson, R. Price, S. White, *Nature* **2021**, *595*, 532.
[156] a) B. Wu, Z. Zhang, C. Wang, E. Song, J. Cui, G. Huang, P. Zhou, Z. Di, Y. Mei, *Appl. Phys. Lett.* **2022**, *121*, 060503; b) G. Liu, Z. Tian, Z. Yang, Z. Xue, M. Zhang, X. Hu, Y. Wang, Y. Yang, P. K. Chu, Y. Mei, L. Liao, W. Hu, Z. Di, *Nat. Electron.* **2022**, *5*, 275; c) Y. Xia, X. Chen, J. Wei, S. Wang, S. Chen, S. Wu, M. Ji, Z. Sun, Z. Xu, W. Bao, P. Zhou, *Nat. Mater.* **2023**, *22*, 1324.
[157] B. Yuan, Z. Chen, Y. Chen, C. Tang, W. Chen, Z. Cheng, C. Zhao, Z. Hou, Q. Zhang, W. Gan, J. Gao, J. Wang, J. Xu, G. Hu, Z. Wu, K. Luo, M. Luo, Y. Zhang, Z. Zhang, S. Xiong, C. Cong, W. Bao, S. Ma, J. Wan, P. Zhou, Y. Lu, *Nat. Commun.* **2024**, *15*, 9038.
[158] J. Deng, L. Zong, M. Zhu, F. Liao, Y. Xie, Z. Guo, J. Liu, B. Lu, J. Wang, W. Hu, P. Zhou, W. Bao, J. Wan, *Adv. Funct. Mater.* **2019**, *29*, 1906242.
[159] K. Xiao, J. Wan, H. Xie, Y. Zhu, T. Tian, W. Zhang, Y. Chen, J. Zhang, L. Zhou, S. Dai, Z. Xu, W. Bao, P. Zhou, *Nat. Commun.* **2024**, *15*, 9782.
[160] L. Tong, J. Wan, K. Xiao, J. Liu, J. Ma, X. Guo, L. Zhou, X. Chen, Y. Xia, S. Dai, Z. Xu, W. Bao, P. Zhou, *Nat. Electron.* **2022**, *6*, 37.
[161] a) Q. Lin, H. Fang, A. Kalaboukhov, Y. Liu, Y. Zhang, M. Fischer, J. Li, J. Hagel, S. Brem, E. Malic, N. Stenger, Z. Sun, M. Wubs, S. Xiao, *Nat. Commun.* **2024**, *15*, 8762; b) L. Kong, X. Zhang, Q. Tao, M. Zhang, W. Dang, Z. Li, L. Feng, L. Liao, X. Duan, Y. Liu, *Nat. Commun.* **2020**, *11*, 1866.
[162] F. Sahli, J. Werner, B. A. Kamino, M. Bräuninger, R. Monnard, B. Paviet-Salomon, L. Barraud, L. Ding, J. J. Diaz Leon, D. Sacchetto, G. Cattaneo, M. Despeisse, M. Boccard, S. Nicolay, Q. Jeangros, B. Niesen, C. Ballif, *Nat. Mater.* **2018**, *17*, 820.
[163] a) Y. Tian, Y. An, J. Feng, *ACS Appl. Mater. Interfaces* **2019**, *11*, 10004; b) H.-C. Fu, V. Ramalingam, H. Kim, C.-H. Lin, X. Fang, H. N. Alshareef, J.-H. He, *Adv. Energy Mater.* **2019**, *9*, 1900180.
[164] C.-Y. You, B.-F. Hu, B.-R. Xu, Z.-Y. Zhang, B.-M. Wu, G.-S. Huang, E.-M. Song, Y.-F. Mei, *Chip* **2022**, *1*, 100034.
[165] a) Z. Wang, B. Tian, M. Pantouvaki, W. Guo, P. Absil, J. Van Campenhout, C. Merckling, D. Van Thourhout, *Nat. Photonics* **2015**, *9*, 837; b) D.-M. Geum, J. Lim, J. Jang, S. Ahn, S. Kim, J. Shim, B. H. Kim, J. Park, W. J. Baek, J. Jeong, S. Kim, *Light. Sci. Appl.* **2024**, *13*, 311; c) I. H. Rodrigues, A. Vorobiev, *IEEE Trans. Electron. Dev.* **2022**, *69*, 1786.
[166] a) J. Park, R. Ghosh, M. S. Song, Y. Hwang, Y. Tchoe, R. K. Saroj, A. Ali, P. Guha, B. Kim, S.-W. Kim, M. Kim, G.-C. Yi, *NPG Asia Mater* **2022**, *14*, 40; b) P. Guo, B. Tian, J. Liang, X. Yang, G. Tang, Q. Li, Q. Liu, K. Zheng, X. Chen, W. Wu, *Adv. Mater.* **2023**, *35*, 2304420; c) C. Lu, M. Li, L. Gao, Q. Zhang, M. Zhu, X. Lyu, Y. Wang, J. Liu, P. Liu, L. Wang, H. Tao, J. Song, A. Ji, P. Li, L. Gu, Z. Cao, N. Lu, *ACS Nano* **2024**, *18*, 5374.
[167] a) S. M. Koepfli, M. Baumann, R. Gadola, S. Nashashibi, Y. Koyaz, D. Rieben, A. C. Güngör, M. Doderer, K. Keller, Y. Fedoryshyn, J. Leuthold, *Nat. Commun.* **2024**, *15*, 7351; b) Y. Zhang, L. Wang, L. Zhao, K. Wang, Y. Zheng, Z. Yuan, D. Wang, X. Fu, G. Shen, W. Han, *Adv. Mater.* **2021**, *33*, 2007890; c) Y. Zou, Z. Zhang, J. Yan, L. Lin, G. Huang, Y. Tan, Z. You, P. Li, *Nat. Commun.* **2022**, *13*, 4372.
[168] a) X. Geng, F. Wang, H. Tian, Q. Feng, H. Zhang, R. Liang, Y. Shen, Z. Ju, G.-Y. Gou, N. Deng, Y.-t. Li, J. Ren, D. Xie, Y. Yang, T.-L. Ren, *ACS Nano* **2020**, *14*, 2860; b) M. A. Haque, M. I. Nugraha, S. H. K. Paleti, D. Baran, *J. Phys. Chem. C* **2019**, *123*, 14928.
[169] a) Y. H. Hwang, B. Noh, J. Lee, H. S. Lee, Y. Park, K. C. Choi, *Adv. Sci.* **2022**, *9*, 2104855; b) X. Zhao, X. Ding, Q. Tang, Y. Tong, Y. Liu, *J. Mater. Chem. C* **2017**, *5*, 12699.
[170] X.-T. He, E.-T. Liang, J.-J. Yuan, H.-Y. Qiu, X.-D. Chen, F.-L. Zhao, J.-W. Dong, *Nat. Commun.* **2019**, *10*, 872.
[171] H. Shu, L. Chang, Y. Tao, B. Shen, W. Xie, M. Jin, A. Netherton, Z. Tao, X. Zhang, R. Chen, B. Bai, J. Qin, S. Yu, X. Wang, J. E. Bowers, *Nature* **2022**, *605*, 457.
[172] A. Zumeit, A. S. Dahiya, A. Christou, D. Shakthivel, R. Dahiya, *npj Flex. Electron.* **2021**, *5*, 18.
[173] G. Zhang, J. Lai, Y. Su, B. Li, B. Li, J. Bu, C.-F. Yang, *Materials* **2019**, *12*, 2601.
[174] T. Kim, Y. Shin, K. Kang, K. Kim, G. Kim, Y. Byeon, H. Kim, Y. Gao, J. R. Lee, G. Son, T. Kim, Y. Jun, J. Kim, J. Lee, S. Um, Y. Kwon, B. G. Son, M. Cho, M. Sang, J. Shin, K. Kim, J. Suh, H. Choi, S. Hong, H. Cheng, H.-G. Kang, D. Hwang, K. J. Yu, *Nat. Commun.* **2022**, *13*, 5815.
[175] T. Imajo, T. Ishiyama, N. Saitoh, N. Yoshizawa, T. Suemasu, K. Toko, *ACS Appl. Electron. Mater.* **2022**, *4*, 269.
[176] X. Feng, T. Wu, Z. Gao, H. Zhao, S. Wu, Y. Zhang, L. Ge, L. Feng, *Nat. Photonics* **2025**.
[177] L. van Deurzen, E. Kim, N. Pieczulewski, Z. Zhang, A. Feduniewicz-Zmuda, M. Chlipala, M. Siekacz, D. Muller, H. G. Xing, D. Jena, H. Turski, *Nature* **2024**, *634*, 334.
[178] S. Abbas, M. Kumar, J. Kim, *Mater. Sci. Semicond. Process.* **2018**, *88*, 86.
[179] J. K. Saha, M. M. Billah, J. Jang, *ACS Appl. Mater. Interfaces* **2021**, *13*, 37350.
[180] L. Wang, D. Ma, C. Xu, X. Gan, P. Ge, L. Zhu, X. Wang, Y. Lv, *Ceram. Int.* **2023**, *49*, 22875.
[181] B. Bao, D. D. Karnaushenko, J. Xu, S. Wang, V. K. Bandari, O. G. Schmidt, D. Karnaushenko, *Adv. Electron. Mater.* **2024**, *10*, 2400036.
[182] M. J. Paik, J. W. Yoo, J. Park, E. Noh, H. Kim, S.-G. Ji, Y. Y. Kim, S. I. Seok, *ACS Energy Lett.* **2022**, *7*, 1864.
[183] S. Cao, H. Zou, B. Jiang, M. Li, Q. Yuan, *Nano Energy* **2022**, *102*, 107635.
[184] J. Tang, Q. Wang, J. Tian, X. Li, N. Li, Y. Peng, X. Li, Y. Zhao, C. He, S. Wu, J. Li, Y. Guo, B. Huang, Y. Chu, Y. Ji, D. Shang, L. Du, R. Yang, W. Yang, X. Bai, D. Shi, G. Zhang, *Nat. Commun.* **2023**, *14*, 3633.
[185] L. Peng, Z. Xu, Z. Liu, Y. Guo, P. Li, C. Gao, *Adv. Mater.* **2017**, *29*, 1700589.
[186] J. Zhao, L. Zhao, Y. Deng, X. Xiao, Z. Ni, S. Xu, J. Huang, *Nat. Photonics* **2020**, *14*, 612.
[187] H. Liu, G. Shi, R. Khan, S. Chu, Z. Huang, T. Shi, H. Sun, Y. Li, H. Zhou, P. Xiao, T. Chen, Z. Xiao, *Adv. Mater.* **2024**, *36*, 2309921.
[188] Y. Zhang, C. Lei, K. Wu, Q. Fu, *Adv. Sci.* **2021**, *8*, 2004821.
[189] H. M. Schrickx, S. Gyurek, C. Moore, E. Hernández-Pagán, C. J. Doherty, M. W. Kudenov, B. T. O'Connor, *Adv. Opt. Mater.* **2024**, *12*, 2400005.
[190] a) MSE Supplies LLC, MSE PRO 4 inch Silicon-on-Insulator (SOI) Wafer (Device: 10µm; Box: 2µm), 2025-02-26, www.msesupplies.com/products/mse-pro-4-inch-silicon-on-insulator-soi-wafer-device-10-m-box-2-m; b) University Wafer, Silicon-on-Insulator (SOI) 150mm, 2025-02-26, order.universitywafer.com/default.aspx?cat = Silicon-on-Insulator%20(SOI).
[191] T. I. Kim, M. J. Kim, Y. H. Jung, H. J. Jang, C. Dagdeviren, H. A. Pao, S. J. Cho, A. Carlson, K. J. Yu, A. Ameen, H. J. Chung, S. H. Jin, Z. Ma, J. A. Rogers, *Chem. Mater.* **2014**, *26*, 3502.

 © 2025 Wiley-VCH GmbH

16163028, 2025, 35, Downloaded from https://advanced.onlinelibrary.wiley.com/doi/10.1002/adfm.202502191 by Fudan University, Wiley Online Library on [08/03/2026]. See the Terms and Conditions (https://onlinelibrary.wiley.com/terms-and-conditions) on Wiley Online Library for rules of use; OA articles are governed by the applicable Creative Commons License

[192] a) A. Goodyear, M. Cooke, *J. Vac. Sci. Technol. A* **2016**, *35*, 01A105; b) I. L. Berry, K. J. Kanarik, T. Lill, S. Tan, V. Vahedi, R. A. Gottscho, *J. Vac. Sci. Technol. A* **2018**, *36*, 01b105; c) B. Roman, J. Bico, *J. Phys.: Condens. Matter* **2010**, *22*, 493101.
[193] a) Y. Gao, M. Asadirad, Y. Yao, P. Dutta, E. Galstyan, S. Shervin, K. H. Lee, S. Pouladi, S. Sun, Y. Li, M. Rathi, J. H. Ryou, V. Selvamanickam, *ACS Appl. Mater. Interfaces* **2016**, *8*, 29565; b) A. Zumeit, A. S. Dahiya, A. Christou, R. Dahiya, *IEEE Sens. Lett.* **2024**, *8*, 1; c) J. Neto, A. S. Dahiya, A. Zumeit, A. Christou, S. Ma, R. Dahiya, *ACS Appl. Mater. Interfaces* **2023**, *15*, 9618.
[194] J. Aberl, E. P. Navarrete, M. Karaman, D. H. Enriquez, C. Wilflingseder, A. Salomon, D. Primetzhofer, M. A. Schubert, G. Capellini, T. Fromherz, P. Deák, P. Udvarhelyi, S. Li, Á. Gali, M. Brehm, *Adv. Mater.* **2024**, *36*, 2408424.
[195] a) T. Gong, Y. Suzuki, K. Hiller, S. Tanaka, *Sens. Actuators A Phys.* **2023**, *363*, 114691; b) S.-N. Hsiao, K. Ishikawa, T. Hayashi, J. Ni, T. Tsutsumi, M. Sekine, M. Hori, *Appl. Surf. Sci.* **2021**, *541*, 148439; c) M. Rondé, A. J. Walton, J. G. Terry, *J. Microelectromech. Syst.* **2021**, *30*, 156; d) M. Rondé, A. J. Walton, J. G. Terry, *IEEE Trans. Semicond. Manuf.* **2021**, *34*, 241.
[196] a) X. Hong, Q. Liang, X. Liu, C. Y. Ji, J. Li, *Adv. Opt. Mater.* **2022**, *11*, 2202150; b) K. Zhang, Y. H. Jung, S. Mikael, J. H. Seo, M. Kim, H. Y. Mi, H. Zhou, Z. Y. Xia, W. D. Zhou, S. Q. Gong, Z. Q. Ma, *Nat. Commun.* **2017**, *8*, 1782.
[197] a) N. A. Srivastava, A. Priya, R. A. Mishra, *Appl. Phys. A* **2019**, *125*, 533; b) Z. F. Chen, Y. S. Lai, C. M. Huang, Y. H. Wang, M. H. Chiang, *2023 IEEE Nanotechnology Materials and Devices Conference (NMDC)* **2023**.
[198] B. Wu, Z. Zhang, B. Chen, Z. Zheng, C. You, C. Liu, X. Li, J. Wang, Y. Wang, E. Song, J. Cui, Z. An, G. Huang, Y. Mei, *Sci. Adv.* **2023**, *9*, adi7805.
[199] a) J. Gaehun, E. Pierre, J. B. Simon, W. Xiaojing, T. Alain Yuji, S. Hamed, Q. Niels, J. Moises, V. Peter, S. Göran, B. Wim, B. G. Kristinn, N. Frank, *Proc.SPIE* **2021**; b) F. Liu, F. He, X. Tang, J. Li, *IEEE Trans. Compon. Packag. Manuf. Technol.* **2024**, *14*, 351.
[200] a) C. Xiang, W. Jin, J. E. Bowers, *Photonics Res.* **2022**, *10*, A82; b) F. Zhao, J. Jin, G. Hu, C. Ma, L. Lu, T. Hu, Y. Liu, D. Hu, M. Liu, C.-L. Jia, *Chem. Eng. J.* **2022**, *450*, 138312; c) Z. Fang, L. Gao, H. Chen, B. Deng, X. Jili, W. Li, T. Liang, S. Qu, Y. Chen, K. Liang, J. Zhang, *Adv. Mater. Technol.* **2022**, *7*, 2101530; d) S. Ghosh, *J. Micromech. Microeng.* **2022**, *32*, 114001; e) W. Huang, J. Zhou, P. J. Froeter, K. Walsh, S. Liu, M. D. Kraman, M. Li, J. A. Michaels, D. J. Sievers, S. Gong, X. Li, *Nat. Electron.* **2018**, *1*, 305.

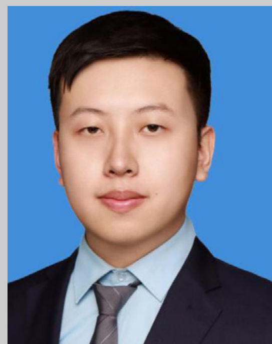

Ziyu Zhang received his B.S. degree in material physics from Fudan University. He is pursuing his Ph.D. degree in material physics and chemistry at Fudan University. His current research interest focuses on the design, fabrication, and application of three-dimensional rolled-up nanomembrane structures for advanced optoelectronics.

Yang Wang received his B.S. degree in materials physics and his Ph.D. in materials science and technology from Fudan University, China. He is currently a postdoctoral researcher at Fudan University, focusing on rolled-up nanomembrane devices and their applications, including microrobots, silicon-based optics, and optoelectronics.

© 2025 Wiley-VCH GmbH

16163028, 2025, 35, Downloaded from https://advanced.onlinelibrary.wiley.com/doi/10.1002/adfm.202502191 by Fudan University, Wiley Online Library on [08/03/2026]. See the Terms and Conditions (https://onlinelibrary.wiley.com/terms-and-conditions) on Wiley Online Library for rules of use; OA articles are governed by the applicable Creative Commons License

Binmin Wu received his Ph.D. in microelectronics and solid-state electronics from Fudan University, China, in 2024. Currently, he is receiving his postdoctoral training at the Shanghai Institute of Technical Physics (SITP), Chinese Academy of Sciences (CAS), Shanghai, China. His current research interests focus on fabrication, mechanisms, and applications of infrared photodetectors based on nanomembrane assembly.

Zengfeng Di received his B.S. degree in biochemistry from Nanjing University and his Ph.D. in microelectronics and solid-state electronics from the Shanghai Institute of Microsystem and Information Technology (SIMIT), Chinese Academy of Sciences (CAS). He is currently a Professor in microelectronics and solid-state electronics, the Director of State Key Laboratory of Materials for Integrated Circuits at SIMIT, CAS, and the Deputy Director of SIMIT, CAS. Prior to joining SIMIT, CAS, he worked as a Director's Postdoctoral Fellow at Los Alamos National Laboratory in the United States. His research interests encompass advanced silicon-on-insulator materials, two-dimensional materials, and microelectronic and optoelectronic devices.

Yongfeng Mei received his B.S. and M.S. degrees from Nanjing University, and Ph.D. degree from the City University of Hong Kong. Following post-doctoral/staff scientist at Max Planck Institute for Solid State Research, as well as group leader/staff scientist at Leibniz Institute for Solid State and Materials Research, he joined Fudan University as a professor in materials physics. He currently serves as deputy department head in the Department of Materials Science and executive director of the International Institute for Intelligent Nanorobots and Nanosystems (IIINN). His current research interest focuses on the development of inorganic nanomembranes in optics, optoelectronics, flexible electronics, and micro/nanoscale robotics.

© 2025 Wiley-VCH GmbH

16163028, 2025, 35, Downloaded from https://advanced.onlinelibrary.wiley.com/doi/10.1002/adfm.202502191 by Fudan University, Wiley Online Library on [08/03/2026]. See the Terms and Conditions (https://onlinelibrary.wiley.com/terms-and-conditions) on Wiley Online Library for rules of use; OA articles are governed by the applicable Creative Commons License